Imaging Biomarkers in Spinocerebellar Ataxias

Doctoral thesis

to obtain a doctorate (PhD)

from the Faculty of Medicine

of the University of Bonn

Mónica Rafaela da Cruz Mota Ferreira

from Lisbon, Portugal

2025

Written with authorization of

the Faculty of Medicine of the University of Bonn

First reviewer: PD Dr. Jennifer Faber

Second reviewer: Prof. Dr. Dr. Florian Mormann

Day of oral examination: 01.12.2025

From Human Imaging Unit at the DZNE (German Center for Neurodegenerative Diseases)

Table of Contents

List of Abbreviations

AD – Axial Diffusivity
ASO – Antisense Oligonucleotide
ATXN3 – Ataxin-3
CAG – Cytosine-Adenine-Guanine
DTI – Diffusion Tensor Imaging
DWI – Diffusion-Weighted Imaging
ESMI – European SCA3/Machado–Joseph Disease Initiative
FA – Fractional Anisotropy
MRI – Magnetic Resonance Imaging
MD – Mean Diffusivity
MWF – Myelin Water Fraction
MWI – Myelin Water Imaging
NfL – Neurofilament Light Chain
QSM – Quantitative Susceptibility Mapping
RD – Radial Diffusivity
SARA – Scale for the Assessment and Rating of Ataxia
SCA – Spinocerebellar Ataxia
SCA3 – Spinocerebellar Ataxia Type 3
SWI – Susceptibility-Weighted Imaging

1. Abstract

Spinocerebellar ataxia type 3 (SCA3) is a progressive neurodegenerative disorder with multisystem involvement and no disease-modifying treatment to date. As targeted therapies move into clinical testing, the need for sensitive imaging biomarkers is critical. This thesis presents a multimodal framework for understanding the structural and microstructural progression of SCA3 and for developing magnetic resonance imaging (MRI) based biomarkers applicable across disease stages. Drawing on cross-sectional and longitudinal data from the European SCA3/Machado– Joseph Disease Initiative (ESMI), this work demonstrates that infratentorial white matter structures—particularly the pons, medulla oblongata, and cerebellar peduncles—showed early and consistent degeneration. Among these, pons volume showed early decline already in pre-symptomatic mutation carriers and showed the highest sensitivity to change, emerging as a robust imaging biomarker across disease stages. Regional atrophy trajectories were modulated by disease severity and duration in distinct, structure-specific patterns. Diffusion tensor imaging showed cerebellar white matter degeneration in cross-sectional comparisons, but high intra-individual variability between visits limited its utility for detecting longitudinal change. Neurofilament light chain (NfL) levels were abnormal decades before clinical onset, but plateaued thereafter and showed limited responsiveness to progression. In contrast, mutant ataxin-3 (ATXN3) concentrations remained relatively constant across the disease course and did not show relevant dynamics. The Scale for the Assessment and Rating of Ataxia (SARA), while widely used clinically, showed lower sensitivity to early progression and exhibited delayed changes relative to imaging markers. To support future biomarker development, a novel method for myelin water estimation was incorporated. While not yet applied in SCA3, it holds great promise for detecting subtle myelin alterations, particularly given the early and pronounced white matter involvement and emerging evidence of oligodendrocyte dysfunction. Together, the findings of this thesis highlight the utility of multimodal imaging for refining disease staging, patient stratification, and identification of suitable imaging biomarkers for clinical trials.

2. Introduction and aims with references

2.1 Spinocerebellar Ataxias

Spinocerebellar ataxias (SCA) are a genetically diverse group of autosomal dominant neurodegenerative disorders, with over 40 subtypes currently identified and more emerging (Klockgether et al., 2019; Wilke et al., 2023). They present with a broad clinical spectrum, ranging from pure cerebellar ataxia to complex multisystem involvement (Klockgether et al., 2019). Ataxias are rare diseases with a global prevalence of 10 to 20 per 100,000 individuals (Durr, 2010; Ruano et al., 2014). Gait disturbances are a common hallmark in all ataxia disorders typically worsen over the course of the disease, often leading to the use of walking aid and finally wheelchair. The most common group of SCAs are the so-called polyglutamine disorders, which include SCA1, SCA2, SCA3, SCA6, SCA7, SCA17 (Durr, 2010). In some variants, such as SCA6, the neuropathology is largely confined to the cerebellum. Others, including SCA1, SCA2, and SCA3, exhibit a larger involvement of central and peripheral nervous system structures, including the brainstem, spinal cord, basal ganglia, and peripheral nerves. Accordingly, the clinical phenotype does include other neurological signs and symptoms beyond ataxia, such as spasticity, sensory neuropathy, oculomotor abnormalities, or rigidity (Klockgether et al., 2019; Paulson et al., 2017).

2.1.1 Spinocerebellar Ataxia Type 3

SCA3, also known as Machado–Joseph disease, is the most common form of dominantly inherited ataxia worldwide (Klockgether et al., 2019). In SCA3, the repeat expansion occurs in the *ATXN3* gene (Kawaguchi et al., 1994), which encodes the deubiquitinating enzyme ataxin-3 (Klockgether et al., 2019), that disrupt cellular processes and lead to neuronal dysfunction and degeneration (Paulson et al., 2017). Clinically, SCA3 is characterized by progressive cerebellar ataxia, frequently accompanied by pyramidal and extrapyramidal signs, peripheral neuropathy, and oculomotor abnormalities (Paulson et al., 2017). Symptoms typically emerge in mid-adulthood, although anticipation can lead to earlier onset in successive generations, most commonly associated with longer CAG repeat lengths (Klockgether et al., 2019). Currently, there is no disease-modifying treatment for SCA3. Gene-silencing strategies, particularly antisense oligonucleotides (ASOs), have demonstrated efficacy in preclinical models (McLoughlin et al., 2018). Although the first ASO trial in SCA3 was terminated early due to safety concerns, these approaches remain among the most promising candidates, particularly for pre-symptomatic intervention. Early interventions require sensitive and reliable biomarkers capable of detecting neurodegenerative changes prior to the clinical onset and of tracking disease progression over time. Clinical assessments lack sensitivity in the pre-symptomatic stage, highlighting the need for objective, quantitative measures to capture early pathological alterations (Faber et al., 2021).

2.1.2 Clinical Assessment and Disease Staging

The Scale for the Assessment and Rating of Ataxia (SARA) quantifies ataxia severity based on eight motor tasks, with scores ranging from 0 (no ataxia) to 40 (severe ataxia) (Schmitz-Hübsch et al., 2006). It is widely used to monitor progression and serves as an outcome measure in ataxia trials (Jacobi et al., 2015). Notably, its scores can vary considerably due to daily fluctuations, particularly in mildly affected individuals (Grobe-Einsler et al., 2021). Longitudinal data suggest an average annual increase of 1-2 points (Jacobi et al., 2015). The threshold of < 3 is used to define clinical onset, with lower scores indicating the pre-ataxic stage (Maas et al., 2015; Schmitz-Hübsch et al., 2006).

Disease duration is typically defined as the time since symptom onset, usually marked by the reported onset of gait disturbances (Klockgether et al., 1998). In pre-symptomatic mutation carriers, time to onset can be estimated using predictive models based on the individual’s current age and CAG repeat length (Tezenas du Montcel et al., 2014). Disease duration is calculated as difference between current age and (estimated) age of onset. As a result, values are negative in individuals, not yet experiencing gait disturbances, indicating years before the expected onset, and are positive in symptomatic individuals, reflecting (reported) years since onset.

Staging is increasingly recognized as essential for stratifying participants in clinical trials, and optimizing the timing of therapeutic interventions. Traditionally, clinical staging relies on measures such as SARA. More recently, fluid biomarkers such as NfL and structural imaging markers have been explored to refine staging. In the context of SCA3, a three-stage model was previously described (Faber et al., 2024): a *carrier stage*, in which individuals carry the pathogenic mutation but show no clinical signs and normal NfL levels; a *biomarker stage*, defined by elevated NfL levels in otherwise asymptomatic carriers; and an *ataxia stage*, marked by the emergence of clinical symptoms of ataxia, typically defined by a SARA score of three or higher.

2.2 Magnetic Resonance Imaging

MRI is a powerful imaging technique that allows visualization of anatomical properties of biological tissues. It is a medical application of nuclear magnetic resonance, in which atomic nuclei with non-zero spin (such as hydrogen protons in water) are aligned in a strong static magnetic field and perturbed by a resonant radio frequency pulse (Martinez, 2018). Magnetic field gradients are applied to spatially encode the location of nuclei during excitation. As the nuclei relax back to their original state, they emit radiofrequency signals, which are detected by receiver coils and used to reconstruct an image. Its non-invasive nature and sensitivity to both macro- and microstructural alterations make MRI a powerful tool for investigating progressive neurodegenerative disorders such as SCA3.

2.2.1 Diffusion Imaging

Diffusion weighed imaging (DWI) extends conventional structural MRI by sensitizing the signal to the random motion (diffusion) of water molecules. In biological tissue, this motion is hindered by structural barriers such as cell membranes and organelles. In white matter, where axons are bundled together into coherent fibre tracts, water diffusion is directionally constrained, occurring preferentially along the orientation of these axonal fibres, which leads to anisotropic diffusion (Beaulieu, 2002). This property allows DWI to probe the microstructural organization of brain tissue. The most established model for quantifying diffusion *in vivo* is diffusion tensor imaging (DTI), which describes diffusion in each voxel using a second-order tensor (Basser et al., 1994). From this model, several scalar metrics are derived that reflect different aspects of tissue microstructure. Fractional anisotropy (FA) quantifies the degree of directionality of diffusion and is commonly used to assess fibre coherence; lower FA values may indicate disrupted axonal organization or myelin loss. Mean diffusivity (MD) reflects the overall magnitude of diffusion within a voxel and tends to increase in the presence of tissue degeneration or expanded extracellular space. Radial diffusivity (RD) quantifies diffusion perpendicular to the main axis and is often associated to changes in myelination, while axial diffusivity (AD) measures diffusion along the primary axis of the tensor and is considered sensitive to axonal integrity (Alexander et al., 2007). While DTI provides a simplified and widely used framework for modelling diffusion, it is inherently limited in regions with complex fibre architecture, such as crossing, kissing, or fanning fibres. More advanced models, such as constrained spherical deconvolution, allow for improved characterization of these configurations by resolving multiple fibre orientations within a voxel.

2.2.2 Susceptibility Imaging

Iron accumulation plays a role in many neurodegenerative disorders and is commonly investigated using susceptibility-based MRI techniques (Harada et al., 2022). T_2^*-weighted and susceptibility-weighted imaging (SWI) are widely used to detect abnormal magnetic susceptibility caused by paramagnetic substances such as iron or blood (Haacke et al., 2004). However, both methods are qualitative, prone to blooming artifacts, and cannot reliably distinguish between paramagnetic and diamagnetic materials such as iron and calcium (Harada et al., 2022). Quantitative susceptibility mapping (QSM) was developed to overcome these limitations by enabling tissue-specific quantification of magnetic susceptibility. It reconstructs susceptibility values from phase images acquired in multi-echo gradient-echo sequences and has been increasingly applied in conditions such as multiple sclerosis, Parkinson’s, Alzheimer's, Huntington’s and spinocerebellar ataxias (Ravanfar et al., 2021). However, QSM reconstruction requires careful processing steps, including phase unwrapping, background field removal, and dipole inversion, each of which introduces potential error sources.

2.2.3 Myelin Imaging

Myelin plays a critical role in the structural and functional integrity of white matter by facilitating saltatory conduction and thus enabling efficient signal transmission along axons (Laule et al., 2007). While DTI can detect microstructural alterations, its metrics are not specific to myelin. Changes in RD, particularly when interpreted alongside FA, seem to indicate primarily demyelination, but do not provide a direct or quantitative measure of myelin content (Jelescu and Budde, 2017; Stikov et al., 2015). Myelin water imaging (MWI) allows to estimate the myelin water fraction (MWF), an indirect marker of myelin content, based on the short T_2 or T_2^* relaxation times of water trapped between the layers of the myelin sheath (Alonso-Ortiz et al., 2015; MacKay et al., 2006). MWF is derived from multi-compartment modelling, which separates the MRI signal into components associated with different water environments, such as intra-/extra-axonal water and myelin-associated water.

2.3 Aims

This thesis aims to identify sensitive and clinically meaningful MRI biomarkers for SCA3. Specifically, it proposes to use macrostructural and microstructural MRI methods to investigate regional brain changes across stages of the disease — from pre-symptomatic mutation carriers to individuals with manifest ataxia — and to examine how these imaging markers relate to clinical measures such as disease severity and duration. To ensure standardized and reproducible analysis across multi-site data, the thesis further aims to develop an automated processing pipeline for structural, diffusion MRI and susceptibility data. This will enable multi-modal analysis and serve as a platform for systematic biomarker identification. Finally, this thesis aims to explore modelling techniques that may enhance the sensitivity of MRI to subtle white matter changes. Together, these aims support the development of imaging tools for early detection, patient stratification, monitoring of disease progression, and application in future clinical trials and therapeutic interventions.

2.4 References

Alexander, A.L., Lee, J.E., Lazar, M., Field, A.S., 2007. Diffusion tensor imaging of the brain. Neurother. J. Am. Soc. Exp. Neurother. 4, 316–329. https://doi.org/10.1016/j.nurt.2007.05.011

Alonso-Ortiz, E., Levesque, I.R., Pike, G.B., 2015. MRI-based myelin water imaging: A technical review. Magn. Reson. Med. 73, 70–81. https://doi.org/10.1002/mrm.25198

Basser, P.J., Mattiello, J., LeBihan, D., 1994. MR diffusion tensor spectroscopy and imaging. Biophys. J. 66, 259–267. https://doi.org/10.1016/S0006-3495(94)80775-1

Beaulieu, C., 2002. The basis of anisotropic water diffusion in the nervous system - a technical review. NMR Biomed. 15, 435–455. https://doi.org/10.1002/nbm.782

Durr, A., 2010. Autosomal dominant cerebellar ataxias: polyglutamine expansions and beyond. Lancet Neurol. 9, 885–894. https://doi.org/10.1016/S1474-4422(10)70183-6

Faber, J., Berger, M., Wilke, C., Hubener-Schmid, J., Schaprian, T., Santana, M.M., Grobe-Einsler, M., Onder, D., Koyak, B., Giunti, P., Garcia-Moreno, H., Gonzalez-Robles, C., Lima, M., Raposo, M., Melo, A.R.V., De Almeida, L.P., Silva, P., Pinto, M.M., Van De Warrenburg, B.P., Van Gaalen, J., De Vries, J., Oz, G., Joers, J.M., Synofzik, M., Schols, L., Riess, O., Infante, J., Manrique, L., Timmann, D., Thieme, A., Jacobi, H., Reetz, K., Dogan, I., Onyike, C., Povazan, M., Schmahmann, J., Ratai, E., Schmid, M., Klockgether, T., 2024. Stage-Dependent Biomarker Changes in Spinocerebellar Ataxia Type 3. Ann. Neurol. 95, 400–406. https://doi.org/10.1002/ana.26824

Faber, J., Schaprian, T., Berkan, K., Reetz, K., França, M.C., De Rezende, T.J.R., Hong, J., Liao, W., Van De Warrenburg, B., Van Gaalen, J., Durr, A., Mochel, F., Giunti, P., Garcia-Moreno, H., Schoels, L., Hengel, H., Synofzik, M., Bender, B., Oz, G., Joers, J., De Vries, J.J., Kang, J., Timmann-Braun, D., Jacobi, H., Infante, J., Joules, R., Romanzetti, S., Diedrichsen, J., Schmid, M., Wolz, R., Klockgether, T., 2021. Regional Brain and Spinal Cord Volume Loss in Spinocerebellar Ataxia Type 3. Mov. Disord. 36, 2273–2281. https://doi.org/10.1002/mds.28610

Grobe-Einsler, M., Taheri Amin, A., Faber, J., Schaprian, T., Jacobi, H., Schmitz-Hübsch, T., Diallo, A., Tezenas du Montcel, S., Klockgether, T., 2021. Development of SARAhome , a New Video-Based Tool for the Assessment of Ataxia at Home. Mov. Disord. Off. J. Mov. Disord. Soc. 36, 1242–1246. https://doi.org/10.1002/mds.28478

Haacke, E.M., Xu, Y., Cheng, Y.-C.N., Reichenbach, J.R., 2004. Susceptibility weighted imaging (SWI). Magn. Reson. Med. 52, 612–618. https://doi.org/10.1002/mrm.20198

Harada, T., Kudo, K., Fujima, N., Yoshikawa, M., Ikebe, Y., Sato, R., Shirai, T., Bito, Y., Uwano, I., Miyata, M., 2022. Quantitative Susceptibility Mapping: Basic Methods and Clinical Applications. Radiogr. Rev. Publ. Radiol. Soc. N. Am. Inc 42, 1161–1176. https://doi.org/10.1148/rg.210054

Jacobi, H., du Montcel, S.T., Bauer, P., Giunti, P., Cook, A., Labrum, R., Parkinson, M.H., Durr, A., Brice, A., Charles, P., Marelli, C., Mariotti, C., Nanetti, L., Panzeri, M., Rakowicz, M., Sulek, A., Sobanska, A., Schmitz-Hübsch, T., Schöls, L., Hengel, H., Baliko, L., Melegh, B., Filla, A., Antenora, A., Infante, J., Berciano, J., van de Warrenburg, B.P., Timmann, D., Szymanski, S., Boesch, S., Kang, J.-S., Pandolfo, M., Schulz, J.B., Molho, S., Diallo, A., Klockgether, T., 2015. Long-term disease progression in spinocerebellar ataxia types 1, 2, 3, and 6: a longitudinal cohort study. Lancet Neurol. 14, 1101–1108. https://doi.org/10.1016/S1474-4422(15)00202-1

Jelescu, I.O., Budde, M.D., 2017. Design and validation of diffusion MRI models of white matter. Front. Phys. 28, 61. https://doi.org/10.3389/fphy.2017.00061

Kawaguchi, Y., Okamoto, T., Taniwaki, M., Aizawa, M., Inoue, M., Katayama, S., Kawakami, H., Nakamura, S., Nishimura, M., Akiguchi, I., Kimura, J., Narumiya, S., Kakizuka, A., 1994. CAG expansions in a novel gene for Machado-Joseph disease at chromosome 14q32.1. Nat. Genet. 8, 221–228. https://doi.org/10.1038/ng1194-221

Klockgether, T., Lüdtke, R., Kramer, B., Abele, M., Bürk, K., Schöls, L., Riess, O., Laccone, F., Boesch, S., Lopes-Cendes, I., Brice, A., Inzelberg, R., Zilber, N., Dichgans, J., 1998. The natural history of degenerative ataxia: a retrospective study in 466 patients. Brain J. Neurol. 121 (Pt 4), 589–600. https://doi.org/10.1093/brain/121.4.589

Klockgether, T., Mariotti, C., Paulson, H.L., 2019. Spinocerebellar ataxia. Nat. Rev. Dis. Primer 5, 24. https://doi.org/10.1038/s41572-019-0074-3

Laule, C., Vavasour, I.M., Kolind, S.H., Li, D.K.B., Traboulsee, T.L., Moore, G.R.W., MacKay, A.L., 2007. Magnetic resonance imaging of myelin. Neurother. J. Am. Soc. Exp. Neurother. 4, 460–484. https://doi.org/10.1016/j.nurt.2007.05.004

Maas, R.P.P.W.M., van Gaalen, J., Klockgether, T., van de Warrenburg, B.P.C., 2015. The preclinical stage of spinocerebellar ataxias. Neurology 85, 96–103. https://doi.org/10.1212/WNL.0000000000001711

MacKay, A., Laule, C., Vavasour, I., Bjarnason, T., Kolind, S., Mädler, B., 2006. Insights into brain microstructure from the T2 distribution. Magn. Reson. Imaging 24, 515–525. https://doi.org/10.1016/j.mri.2005.12.037

Martinez, G.V., 2018. Introduction to MRI Physics. Methods Mol. Biol. Clifton NJ 1718, 3–19. https://doi.org/10.1007/978-1-4939-7531-0_1

McLoughlin, H.S., Moore, L.R., Chopra, R., Komlo, R., McKenzie, M., Blumenstein, K.G., Zhao, H., Kordasiewicz, H.B., Shakkottai, V.G., Paulson, H.L., 2018. Oligonucleotide therapy mitigates disease in spinocerebellar ataxia type 3 mice. Ann. Neurol. 84, 64–77. https://doi.org/10.1002/ana.25264

Paulson, H.L., Shakkottai, V.G., Clark, H.B., Orr, H.T., 2017. Polyglutamine spinocerebellar ataxias - from genes to potential treatments. Nat. Rev. Neurosci. 18, 613–626. https://doi.org/10.1038/nrn.2017.92

Ravanfar, P., Loi, S.M., Syeda, W.T., Van Rheenen, T.E., Bush, A.I., Desmond, P., Cropley, V.L., Lane, D.J.R., Opazo, C.M., Moffat, B.A., Velakoulis, D., Pantelis, C., 2021. Systematic Review: Quantitative Susceptibility Mapping (QSM) of Brain Iron Profile in Neurodegenerative Diseases. Front. Neurosci. 15, 618435. https://doi.org/10.3389/fnins.2021.618435

Ruano, L., Melo, C., Silva, M.C., Coutinho, P., 2014. The global epidemiology of hereditary ataxia and spastic paraplegia: a systematic review of prevalence studies. Neuroepidemiology 42, 174–183. https://doi.org/10.1159/000358801

Schmitz-Hübsch, T., du Montcel, S.T., Baliko, L., Berciano, J., Boesch, S., Depondt, C., Giunti, P., Globas, C., Infante, J., Kang, J.-S., Kremer, B., Mariotti, C., Melegh, B., Pandolfo, M., Rakowicz, M., Ribai, P., Rola, R., Schöls, L., Szymanski, S., van de Warrenburg, B.P., Dürr, A., Klockgether, T., Fancellu, R., 2006. Scale for the assessment and rating of ataxia: development of a new clinical scale. Neurology 66, 1717–1720. https://doi.org/10.1212/01.wnl.0000219042.60538.92

Stikov, N., Campbell, J.S.W., Stroh, T., Lavelée, M., Frey, S., Novek, J., Nuara, S., Ho, M.-K., Bedell, B.J., Dougherty, R.F., Leppert, I.R., Boudreau, M., Narayanan, S., Duval, T., Cohen-Adad, J., Picard, P.-A., Gasecka, A., Côté, D., Pike, G.B., 2015. In vivo histology of the myelin g-ratio with magnetic resonance imaging. NeuroImage 118, 397–405. https://doi.org/10.1016/j.neuroimage.2015.05.023

Tezenas du Montcel, S., Durr, A., Rakowicz, M., Nanetti, L., Charles, P., Sulek, A., Mariotti, C., Rola, R., Schols, L., Bauer, P., Dufaure-Garé, I., Jacobi, H., Forlani, S., Schmitz-Hübsch, T., Filla, A., Timmann, D., van de Warrenburg, B.P., Marelli, C., Kang, J.-S., Giunti, P., Cook, A., Baliko, L., Melegh, B., Boesch, S., Szymanski, S., Berciano, J., Infante, J., Buerk, K., Masciullo, M., Di Fabio, R., Depondt, C., Ratka, S., Stevanin, G., Klockgether, T., Brice, A., Golmard, J.-L., 2014. Prediction of the age at onset in spinocerebellar ataxia type 1, 2, 3 and 6. J. Med. Genet. 51, 479–486. https://doi.org/10.1136/jmedgenet-2013-102200

Wilke, C., Pellerin, D., Mengel, D., Traschütz, A., Danzi, M.C., Dicaire, M.-J., Neumann, M., Lerche, H., Bender, B., Houlden, H., RFC1 study group, Züchner, S., Schöls, L., Brais, B., Synofzik, M., 2023. GAA-FGF14 ataxia (SCA27B): phenotypic profile, natural history progression and 4-aminopyridine treatment response. Brain J. Neurol. 146, 4144–4157. https://doi.org/10.1093/brain/awad157

3. Publications

3.1 Publication 1: Cerebellar Volumetry in Ataxias: Relation to Ataxia Severity and Duration (DOI: 10.1007/s12311-024-01659-0)

The Cerebellum (2024) 23:1521–1529
https://doi.org/10.1007/s12311-024-01659-0

RESEARCH

Cerebellar Volumetry in Ataxias: Relation to Ataxia Severity and Duration

Mónica Ferreira[1,2] · **Tamara Schaprian**[1] · **David Kügler**[1] · **Martin Reuter**[1,3,4] · **Katharina Deike‑Hoffmann**[5] · **Dagmar Timmann**[6] · **Thomas M. Ernst**[6] · **Paola Giunti**[7,8] · **Hector Garcia‑Moreno**[7,8] · **Bart van de Warrenburg**[9] · **Judith van Gaalen**[9,10] · **Jeroen de Vries**[11] · **Heike Jacobi**[12] · **Katharina Marie Steiner**[6] · **Gülin Öz**[13] · **James M. Joers**[13] · **Chiadi Onyike**[14] · **Michal Povazan**[14] · **Kathrin Reetz**[15,16] · **Sandro Romanzetti**[15] · **Thomas Klockgether**[1,17] · **Jennifer Faber**[1,17]

Accepted: 15 January 2024 / Published online: 16 February 2024

Abstract

Cerebellar atrophy is the neuropathological hallmark of most ataxias. Hence, quantifying the volume of the cerebellar grey and white matter is of great interest. In this study, we aim to identify volume differences in the cerebellum between spinocerebellar ataxia type 1 (SCA1), SCA3 and SCA6 as well as multiple system atrophy of cerebellar type (MSA-C). Our cross-sectional data set comprised mutation carriers of SCA1 (N=12), SCA3 (N=62), SCA6 (N=14), as well as MSA-C patients (N=16). Cerebellar volumes were obtained from T1-weighted magnetic resonance images. To compare the different atrophy patterns, we performed a z-transformation and plotted the intercept of each patient group's model at the mean of 7 years of ataxia duration as well as at the mean ataxia severity of 14 points in the SARA sum score. In addition, we plotted the extrapolation at ataxia duration of 0 years as well as 0 points in the SARA sum score. Patients with MSA-C demonstrated the most pronounced volume loss, particularly in the cerebellar white matter, at the late time intercept. Patients with SCA6 showed a pronounced volume loss in cerebellar grey matter with increasing ataxia severity compared to all other patient groups. MSA-C, SCA1 and SCA3 showed a prominent atrophy of the cerebellar white matter. Our results (i) confirmed SCA6 being considered as a pure cerebellar grey matter disease, (ii) emphasise the involvement of cerebellar white matter in the neuropathology of SCA1, SCA3 and MSA-C, and (iii) reflect the rapid clinical progression in MSA-C.

Keywords Ataxia · Atrophy · Cerebellum · z-scores

Introduction

Among the adult-onset degenerative cerebellar ataxias, the autosomal dominantly inherited polyglutamine spinocerebellar ataxias type 1 (SCA1), SCA3, and SCA6, and the sporadic multiple system atrophy of cerebellar type (MSA-C) are most common [1]. SCA1, SCA3 and SCA6 are caused by translated CAG repeat expansion mutations of variable length in the respective genes. The mutations result in formation of abnormal disease proteins containing elongated polyglutamine stretches [1]. MSA-C is neuropathologically defined by the presence of alpha-synuclein-positive inclusions in oligodendroglia. The diagnosis of MSA-C relies on clinical features, particularly including severe autonomic failure [2, 3]. SCA1, SCA3, and MSA-C are multisystemic diseases that not only affect the cerebellum, but also involve the spinal cord, brainstem, basal ganglia, and other regions of the central nervous system. Ataxia is the primary clinical feature, with additional other non-ataxia symptoms such as spasticity, rigidity or ophthalmoparesis. In contrast, SCA6 is considered as an almost purely cerebellar disease characterised by isolated cerebellar ataxia without major non-ataxia signs [1, 4]. Previous neuropathological and MRI studies examining the atrophy patterns of SCA1, SCA3, SCA6, and MSA-C have, to date, predominantly used voxel-based morphometry and emphasised the involvement of extracerebellar structures [5–11]. While voxel-wise analysis can be useful for detecting subtle or widespread changes in brain structure, it is essential to focus on specific regions of the cerebellum when studying cerebellar ataxias. Recent progress in the MRI

✉ Jennifer Faber
jennifer.faber@dzne.de

Extended author information available on the last page of the article

morphometric analysis of the cerebellum allows detailed quantitative assessment of the cerebellum at the lobular level and precise delineation of cerebellar white matter [12].

The aim of this study was the investigation of the pattern of cerebellar grey and white matter atrophy in SCA1, SCA3, SCA6 and MSA-C. We applied a z-transformation to correct for age effects and used a linear model with read-outs at defined time points of the disease course and degrees of ataxia severity, to allow the comparison of the amount and pattern of cerebellar atrophy between SCA1, SCA3, SCA6 and MSA-C.

Methods

Participants

Cross-sectional data of SCA1 ($N = 12$), SCA3 ($N = 62$), SCA6 ($N = 14$) and MSA-C ($N = 16$) were analysed. In addition, healthy controls (HCs) ($N = 292$) were analysed and used as a reference for the z-transformation. All subjects participated in ongoing observational studies (ESMI, SCA Registry, DANCER, DELCODE) at 8 European and 2 US sites, and were enrolled between 2017 and 2022. All participants gave their written informed consent according to the declaration of Helsinki. SCA diagnosis was confirmed by diagnostic genetic testing, MSA-C was diagnosed applying the diagnostic criteria from 2008 [2]. The new diagnostic criteria of Wenning et al. [3] could not be applied retrospectively. Ataxia severity was assessed using the Scale of Assessment and Rating of Ataxia (SARA) [13]. We only included ataxic patients with SARA sum scores higher than or equal to the established cutoff value of 3 [13, 14]. Ataxia onset was defined as the first occurrence of gait disturbances, and the reported ataxia duration in years was calculated accordingly.

Imaging Protocol

All participants were scanned on 3T SIEMENS scanners, with a 32-channel head coil, using a standardised T1-weighted magnetisation-prepared rapid gradient-echo (MPRAGE) sequence. Sequence parameters were as follows: repetition time (TR) = 2500 ms, echo time (TE) = 4.37 ms, inversion time (TI) = 1100 ms, flip angle = 7°, field of view 256 x 256 mm^2 and 192 slices, voxel size = 1 mm isotropic.

Image Analysis

We used *CerebNet* [12] for the automated sub-segmentation of the cerebellum into the following volumes (for hemispheric volumes, each volume corresponds to the combined volumes of left and right hemisphere): anterior lobe (consisting of the lobules I-V), superior posterior lobe (consisting of the lobules VI-VII), inferior posterior lobe (consisting of the lobules VIII-IX) and the flocculonodular lobe (corresponding to lobule X) and the midline vermis as well as the cerebellar white matter (cWM). In addition we analysed the combined volume of cerebellar grey matter (cGM) comprised of all hemispheric volumes plus vermis. All scans were visually inspected.

Exemplary cases of the automated cerebellar segmentations are shown in Fig. 1.

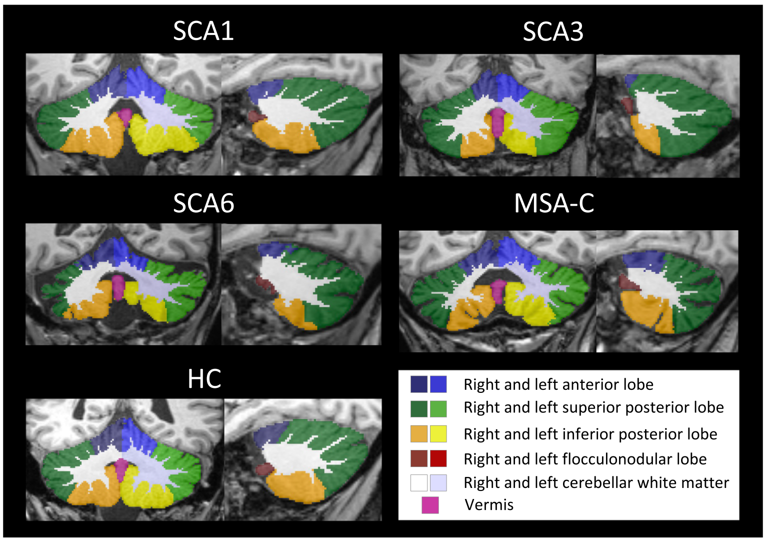

Fig. 1 Segmentation examples of a fully automated cerebellar segmentation in SCA1, SCA3, SCA6 and MSA-C patients as well as in a HC, projected onto a coronal and sagittal slice

To account for individual differences in head size, we used estimated total intracranial volume (eTIV) calculated with *FreeSurfer* (version 6.0.0) [15]. Normalised cerebellar volumes were calculated by dividing the raw cerebellar volumes by the individual's eTIV. These values were harmonised across sites using the ComBat method to adjust for potential batch effects [16–18].

Statistical Analysis of Cerebellar Atrophy in Relation to Ataxia Duration and Ataxia Severity

All statistical analyses were performed using R Software for Statistical Computing, version 4.2.3 [19]. In order to compare volumes across the different diseases, we z-transformed each normalised volume in relation to HCs to compensate for age-related atrophy, as described previously [20]. Here, a z-score of 0 corresponds to the respective, expected mean in HCs of the same age. A z-score of ±1, ±2 etc. corresponds to ±1, ±2 etc. standard deviations below or above the expected mean in HCs of the same age [20]. The resulting z-scores were used for all subsequent statistical analyses.

In order to compare the different ataxias at the same time points of ataxia duration and degrees of ataxia severity the following stepwise approach was performed for each considered cerebellar volume. First, we plotted the z-scores for each cerebellar volume against the reported ataxia duration in years as well as ataxia severity assessed with the SARA sum score. Here, we applied a linear model for each disease and calculated the coefficient of determination (R^2) and p-value for every correlation. Moreover, quadratic and cubic models were also established. Second, we defined the points for comparison: (i) we calculated the overall mean ataxia duration and ataxia severity for all patient groups, which were 7 years of ataxia duration and a SARA sum score of 14, and (ii) we used the extrapolation at 0 years of ataxia duration and the absence of ataxia (SARA sum score of 0). Accordingly, the intercept volume z-score of the linear interpolation line at 0 years and 7 years of ataxia duration, and at a SARA sum score of 0 and 14, were extracted for each disease. Finally, radar plots of these intercept z-scores for each considered volume were used to visualise the degree and patterns of cerebellar atrophy in SCA1, SCA3, SCA6 and MSA-C at 0 and 7 years of disease duration as well as an ataxia severity of 0 and 14 points in the SARA sum score.

Results

Demographic and characterising data are summarised in Table 1. SCA1 had the earliest age of onset, while SCA3 patients the longest reported ataxia duration, followed by SCA6. Notably, MSA-C was associated with the highest SARA sum scores among all studied ataxia groups.

Cerebellar Atrophy in Relation to Ataxia Duration and Ataxia Severity

The linear model of volume z-scores and ataxia duration as well as severity are given in Figs. 2 and 3. The coefficient of determination (R^2) as well as the p-value representing evidence of a linear relationship are given in the superior left corner of each subplot. Using quadratic and cubic models, neither the residual versus fitted values plots nor the Q-Q plots showed substantial improvement in comparison to the linear model. Thus, given the limited sample size we based the further analyses on the linear model (Supplement Figs. 4- 15).

The relation of cerebellar volumes and ataxia duration in years is shown in Fig. 2. Overall, most volumes decreased with increased ataxia duration. The steepest decline of all cerebellar grey and white matter volumes was observed in MSA-C, followed by SCA6 except for cerebellar white matter. In SCA1, the anterior, superior posterior, and flocculonodular lobe, and in SCA3 the anterior, superior posterior and flocculonodular lobe as well as aggregated cGM, showed a not significant slight volume increase with longer ataxia duration.

With regard to ataxia severity, most volumes decreased with increased ataxia severity. Overall, MSA-C and SCA6 showed the steepest decline in all grey matter volumes, and MSA-C additionally in the white matter volume, with exception for cWM in SCA6 that presented a slight volume

Table 1 Demographic and cohort characteristics

Group entity	Number (Female/ Male)	Age at scan[1] mean (SD)	Ataxia duration mean (SD)	SARA sum score mean (SD)	CAG repeats[2] mean (SD)
SCA1	12 (7/5)	45.1 (9.6)	3.9 (3.3)	12.1 (3.9)	48.3 (4.2)
SCA3	62 (25/37)	50.7 (10.6)	10.8 (6.5)	12.8 (6.2)	67.8 (8.0)
SCA6	14 (4/10)	64.2 (8.6)	7.8 (5.5)	13.3 (4.9)	21.8 (0.5)
MSA-C	16 (6/10)	64.5 (8.2)	4.4 (2.1)	17.2 (5.2)	n.a.
HC	292 (160/132)	63.5 (12.6)	n.a.	n.a.	n.a.

SD, standard deviation; *SCA*, spinocerebellar ataxia; *MSA-C*, multiple system atrophy of cerebellar type; *HC*, healthy control; *n.a.*, not applicable. [1] in years; [2] of the longer allele

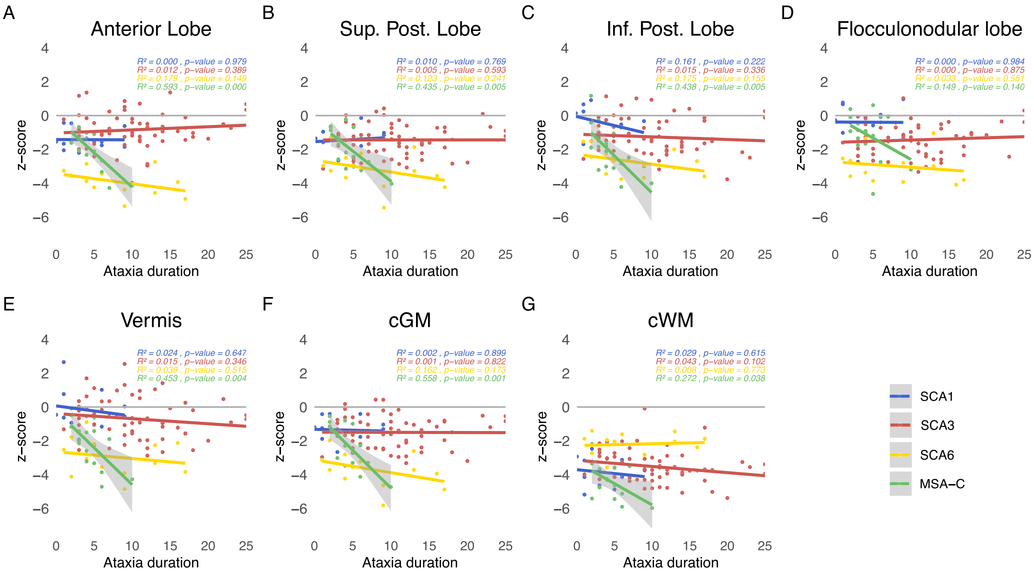

Fig. 2 Relation of cerebellar volumes and ataxia duration in years. The z-scores of each cerebellar sub-segmented region are plotted against the reported ataxia duration in years for SCA1 (in blue), SCA3 (in red), SCA6 (in yellow) and MSA-C (in green). Linear interpolation was applied with the 95% confidence intervals given as shaded grey areas for linear regressions with significant correlations ($p \leq 0.05$). Values of the coefficient of determination (R^2) as well as the p-value are given for each disease, respectively

increase. In SCA1 the anterior and superior posterior lobe, as well as cGM, and in SCA3 the flocculonodular lobe and the vermis, as well as in SCA6 the cerebellar white matter showed a not significant slight volume increase with increased ataxia severity. The relation between cerebellar volumes and ataxia severity is shown in Fig. 3.

R^2 values were overall relatively small, and ranged between 0 and 0.54. Generally, the highest R^2 was observed in MSA-C followed by SCA6. In MSA-C R^2 was emphasised in relation to ataxia duration with the maximum of $R^2 = 0.537$ for cGM. In SCA6 R^2 was emphasised in relation to ataxia severity. SCA1 and SCA3 showed very small values of R^2, except for the relation of cWM and ataxia severity in SCA3. In MSA-C the correlation with ataxia duration of all cerebellar volumes reached statistical significance with $p \leq 0.05$, except for the flocculonodular lobe. The correlation with ataxia severity reached statistical significance in all volumes, except the anterior lobe and vermis and MSA-C. In the SCAs, only the correlation of cerebellar white matter and ataxia severity in SCA3 reached statistical significance with a $p \leq 0.05$.

To visualise for each disease the pattern and extent of atrophy at certain time points of ataxia duration and degrees of ataxia severity, we displayed the linear interpolated z-scores for the volumes of the anterior, superior posterior and inferior posterior and flocculonodular lobe and vermis as well as cGM and cWM in radar plots. Figure 4 shows radar plots of the extrapolation at the time of ataxia onset (ataxia duration of 0 years) and at 7 years after ataxia onset, as well as for the intercept at SARA sum scores of 0 and 14. Comparison of the radar plots at ataxia onset and at 7 years after onset revealed a strong atrophy increase in MSA-C, whereas the increase was less pronounced in the SCAs. Comparison of the plots at SARA sum score of 0 and of 14 revealed an emphasised atrophy increase in SCA6 and MSA-C, whereas the increase was only minor in SCA1 and SCA3. Moreover, in SCA1, SCA3 and MSA-C cWM volume was consistently affected, in contrast to SCA6, where the cWM was considerably less affected than the grey matter structures.

Discussion

We used a z-transformation to study the degree and distribution of cerebellar atrophy in SCA1, SCA3, SCA6 and MSA-C at certain levels of ataxia duration and ataxia severity, while accounting for the healthy aging effect. We could demonstrate a strong coherence between ataxia severity and grey matter atrophy in SCA6, underlining the consideration of SCA6 as a pure cerebellar disease. In contrast, volume loss of

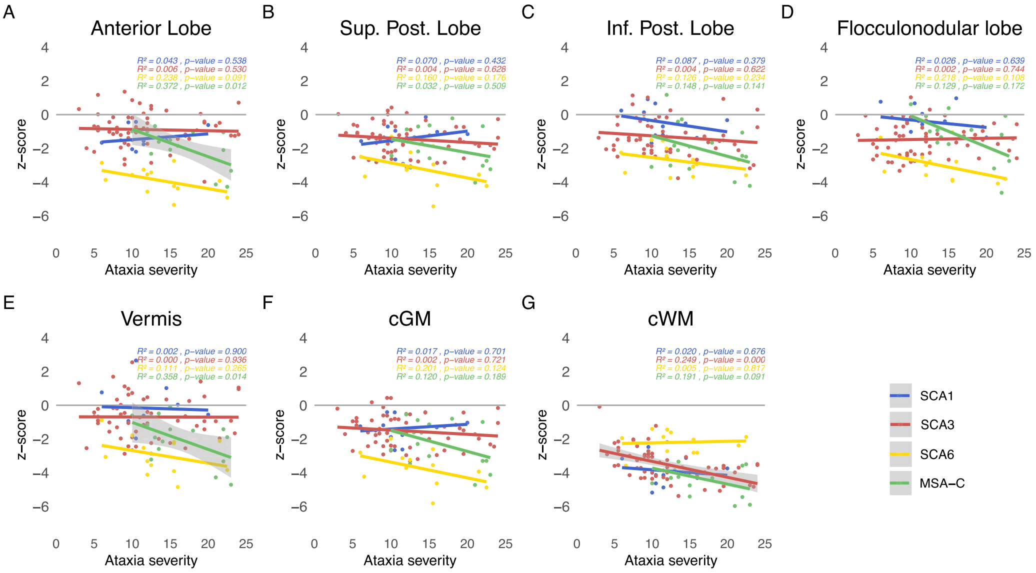

Fig. 3 Relation of cerebellar volumes and ataxia severity. The z-scores of each cerebellar sub-segmented region are plotted against ataxia severity measured with SARA sum score for SCA1 (in blue), SCA3 (in red), SCA6 (in yellow) and MSA-C (in green). Linear interpolation was applied with the 95% confidence intervals given as shaded grey areas for linear regressions with significant correlations ($p \leq 0.05$). Values of the coefficient of determination (R^2) as well as the p-value are given for each disease, respectively

the cerebellar white matter was prominent in MSA-C, SCA1 and SCA3. Overall MSA-C showed the steepest decline of all cerebellar white and grey matter volumes in particular in relation to ataxia duration.

Since ataxias are rare diseases, patient populations are often small and additionally, as in our sample, differ in duration and severity of ataxia, making comparison between entities difficult. We chose the applied approach to overcome this limitation and used radar plots to visualise the differences in atrophy patterns between diseases at certain levels of ataxia duration and severity.

Our results are in line with previous studies mainly of voxel-based-morphometry as well as volumetry in SCAs and MSA-C [5, 6, 8, 21–23]. Notably, throughout the different considered intersections of ataxia duration and ataxia severity, we confirmed earlier findings that, in contrast to other SCA genotypes, atrophy in SCA6 was mainly restricted to the cerebellar GM almost excluding the WM [24, 25]. While cerebellar GM atrophy at the extrapolated point of 0 SARA sum score has no clear discernible pattern across the diseases, it becomes markedly emphasised in SCA6 with increasing ataxia severity in comparison to SCA1, SCA3 and MSA-C. Thus, in SCA6 cerebellar atrophy seems to account almost solely for the clinically observed ataxia. In contrast, it is known, that the neuropathology in the other, multisystemic disorders SCA1, SCA3 and MSA-C also involves other parts of the central nervous system, e.g. brainstem and basal ganglia [1, 20, 26]. Here, the resulting non-ataxia symptoms, e.g. spasticity or rigidity, probably exacerbate motor and coordination impairments. In other words, by concept, the impairments measured by the SARA scale primarily capture ataxia but may be aggravated by other non-ataxia symptoms. With regard to ataxia duration, MSA-C shows the most pronounced cerebellar grey and white matter atrophy with increasing ataxia duration. This observation reflects the known rapid clinical progression in MSA-C [27]. For the clinical diagnosis of MSA, qualitative imaging features have recently been included as mandatory features [3], underlining their importance. In this analysis, due to the recruitment period, only the former clinical criteria [2] found the basis for the clinical diagnosis of probable MSA-C. We excluded one patient who met these former clinical diagnostic criteria but had an unexpectedly long disease duration of > 30 years. Future studies might be more specific with potentially improved diagnostic accuracy due to the revised clinical criteria. Cerebellar white matter atrophy was pronounced in MSA-C, SCA1 and SCA3, with the steepest and significant decline relative to ataxia severity in SCA3 and MSA-C. In MSA-C, alpha-synuclein deposition in oligodendrocytes represents the central neuropathological changes. However, also

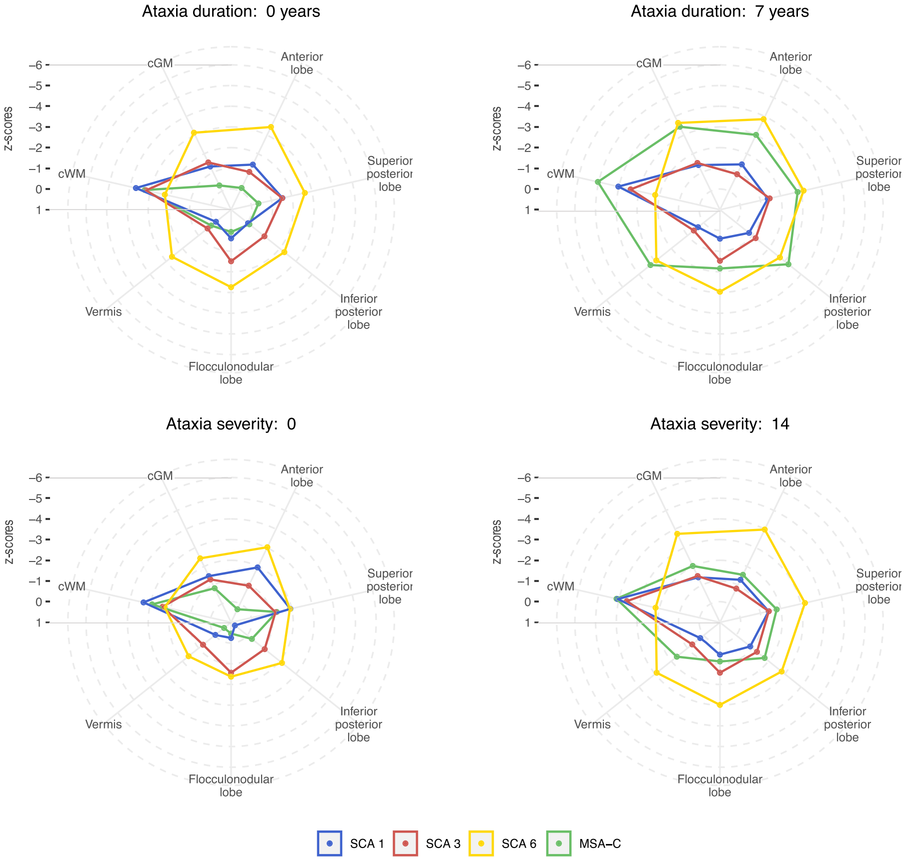

Fig. 4 Radar plot of atrophy in SCA1, SCA3, SCA6 and MSA-C at ataxia duration equal to 0 and 7 years and at ataxia severity of a SARA sum score equal to 0 and 14. For each volume the intercept at an ataxia duration of 0 years (A) as well as the mean ataxia duration of 7 years (B) from the linear interpolation of volume z-scores against ataxia duration, Fig. 2, is given. Similarly, the intercept at SARA sum score of 0 (C) as well as the mean SARA sum score of 14 (D) from the linear interpolation of volume z-scores against ataxia severity, Fig. 3, is given. A z-score of 0 corresponds to the mean of healthy control distribution, while z-scores of ±1, ±2 etc. correspond to values which are 1, 2 etc. standard deviations (SD) of the distributions in HC above or below the mean in HC, respectively

in SCA3 there is increasing evidence for a strong involvement of oligodendrocytes in the disease-specific neuropathology [28].

Our approach allowed the comparison of the different diseases at specific levels of duration and severity of ataxia, yet these results are based on indirect measurements and are therefore subject to limitations that must be considered. The number of available participants, along with their relatively short spans of ataxia duration and severity levels, obviously can impact the linear model. Cubic and quadratic models are provided in the Supplementary Data. However, neither the residual versus fitted values plots nor the Q-Q plots showed substantial improvement compared to the linear model. Thus, given the limited sample size and previous literature showing linear relations between, e.g., ataxia severity and disease duration [9, 29–31], we kept the linear assumption.

Within the SCAs, in particular SCA1 and SCA3, we found in a minority of volumes a contra-intuitive increase of volumes with increasing ataxia duration or severity. We hypothesise that this is either due to noise or a selection bias with a biased focus on the proportion of less affected patients in advanced stages. Severely affected patients suffer substantial restrictions in mobility and are often no longer able to travel to study visits. Thus, the complete spectrum of advanced stage patients might not be represented, but rather, there may be a positive selection of those who are still reasonably mobile despite an advanced SARA score. Studies with larger sample sizes and in addition ideally longitudinal data are needed to study the differences between diseases more reliably at comparable levels of ataxia severity and duration. Despite the aforementioned limitations, our results are able to illustrate main principles using comparative visualisations of volumetric changes in cerebellar grey and white matter in MSA-C, SCA1, SCA3 and SCA6 and thereby may inform further studies on a broader data basis.

Conclusion

Application of z-transformation to correct for age effects and the use of a linear model to read-out volumetric values at distinct levels of disease duration and ataxia severity allowed comparison of the extend and pattern of cerebellar atrophy between SCA1, SCA3, SCA6 and MSA-C. In summary, our results confirmed that SCA6 is primarily a pure cerebellar disease with markedly emphasised cGM atrophy. In contrast, a prominent involvement of cWM was found in SCA1, SCA3 and MSA-C. The well-known rapid clinical progression in MSA-C was also reflected in impressive volume loss later in the disease course. Further studies in larger longitudinal samples are needed to confirm our findings and put them on a broader basis.

Supplementary Information The online version contains supplementary material available at https://doi.org/10.1007/s12311-024-01659-0.

Acknowledgements TK and BvdW are members of the European Reference Network for Rare Neurological Diseases (ERN-RD, project number 739510). The ESMI consortium acknowledges Ruth Hossinger for the project management of the ESMI project and for all contributions made towards the success of this project. The authors would like to thank Peter Barker for assisting with data collection.

Author Contributions Conception and design of the study: MF, TK, JF; Writing a significant portion of the manuscript: MF, TK, JF; Acquisition and analysis of data: MF, TS, DK, MR, KDH, DT, TME, PG, HGM, BvdW, JvG, JdV, HJ, KMS, GO, JMJ, CO, MP, KR, TK, JF; Figures preparation: MF, JF; All authors reviewed the manuscript.

Funding Open Access funding enabled and organized by Projekt DEAL. This publication is an outcome of ESMI, an EU Joint Programme - Neurodegenerative Disease Research (JPND) project (see www.jpnd.eu). The project is supported through the following funding organisations under the aegis of JPND: Germany, Federal Ministry of Education and Research (BMBF; funding codes 01ED1602A/B); Netherlands, The Netherlands Organisation for Health Research and Development; Portugal, Fundação para a Ciência e Tecnologia (FCT, funding code JPCOFUND/0002/2015); United Kingdom, Medical Research Council For Peer Review (MR/N028767/1). This project has received funding from the European Union's Horizon 2020 research and innovation programme under grant agreement No. 643417. At the US sites this work was in part supported by the National Ataxia Foundation and the National Institute of Neurological Disorders and Stroke (NINDS) grant R01NS080816. The Center for Magnetic Resonance Research is supported by the National Institute of Biomedical Cores for Imaging and Advanced Neuroimaging award P30 NS076408 and S10 OD017974 grant. JF received funding as a fellow of the Hertie Network of Excellence in Clinical Neuroscience. MR is supported by FCT (CEECIND/03018/2018). BvdW from ZonMw, NWO, Gossweiler Foundation, Brugling Fonds, Radboudumc, Hersenstichting. DT received research grants from the Deutsche Forschungsgemeinschaft (DFG), European Union (EU), the Bernd Fink Foundation and the Once Upon a Time Foundation. JJ received grant support from National Institutes of Health (NIH) and Friedrich's Ataxia Research Alliance (FARA).

Availability of Data and Materials This declaration is not applicable.

Declarations

Ethics Approval The study was approved by the local ethics committees. Written informed consent according to the declaration of Helsinki was obtained from all participants.

Conflict of Interest The authors declare no competing interests.

References

1. Klockgether T, Mariotti C, Paulson H. Spinocerebellar Ataxia. Nat Rev Dis Prim. 2016;5(1). https://doi.org/10.1038/s41572-019-0074-3.
2. Gilman S, Wenning G, Low P, Brooks D, Mathias C, Trojanowski J, et al. Second consensus statement on the diagnosis of multiple system atrophy. Neurology. 2008;71(9):670–6. https://doi.org/10.1212/01.wnl.0000324625.00404.15.
3. Wenning G, Stankovic I, Vignatelli L, Fanciulli A, Calandra-Buonaura G, Seppi K, et al. Rhe movement disorder society criteria for the diagnosis of multiple system atrophy. Mov Disord. 2022;37(6):1131–48. https://doi.org/10.1002/mds.29005.
4. Rentiya Z, Hutnik R, Mekkam Y, Bae J. The pathophysiology and clinical manifestations of spinocerebellar Ataxia type 6. Cerebellum. 2020;19(3):459–64. https://doi.org/10.1007/s12311-020-01120-y.
5. Hernandez-Castillo CR, King M, Diedrichsen J, Fernandez-Ruiz J. Unique degeneration signatures in the cerebellar cortex for spinocerebellar Ataxias 2, 3, and 7. NeuroImage Clin. 2018;20:931–8. https://doi.org/10.1016/j.nicl.2018.09.026.
6. Reetz K, Costa AS, Mirzazade S, Lehmann A, Juzek A, Rakowicz M, et al. Genotype-specific patterns of Atrophy progression are more sensitive than clinical decline in SCA1, SCA3 and

SCA6. Brain. 2013;136(Pt 3):905–17. https://doi.org/10.1093/brain/aws369.
7. Deistung A, Jäschke D, Draganova R, Pfaffenrot V, Hulst T, Steiner KM, et al. Quantitative susceptibility mapping reveals alterations of dentate nuclei in common types of degenerative cerebellar Ataxias. Brain Commun. 2022;4(1):fcab306. https://doi.org/10.1093/braincomms/fcab306.
8. Adanyeguh IM, Perlbarg V, Henry PG, Rinaldi D, Petit E, Valabregue R, et al. Autosomal dominant cerebellar Ataxias: imaging biomarkers with high effect sizes. NeuroImage: Clin. 2018;19:858–67. https://doi.org/10.1016/j.nicl.2018.06.011.
9. Chandrasekaran J, Petit E, Park YW, du Montcel ST, Joers JM, Deelchand DK, et al. Clinically meaningful magnetic resonance endpoints sensitive to Preataxic spinocerebellar Ataxia types 1 and 3. Ann Neurol. 2022. https://doi.org/10.1002/ana.26573.
10. Gitaí LLG, Sobreira-Neto MA, Diniz PRB, Éckeli AL, Fernandes RMF, Marques WJ, et al. Voxel-based morphometry and relaxometry demonstrate macro- and microstructural damages in spinocerebellar Ataxia type 3. Cerebellum. 2023;22(5):818–24. https://doi.org/10.1007/s12311-022-01452-x.
11. Della Nave R, Ginestroni A, Tessa C, Salvatore E, De Grandis D, Plasmati R, et al. Brain white matter damage in SCA1 and SCA2. An in vivo study using voxel-based morphometry, histogram analysis of mean diffusivity and tract-based spatial statistics. Neuroimage. 2008;43(1):10–19. Epub 2008 Jul 11. PMID: 18672073. https://doi.org/10.1016/j.neuroimage.2008.06.036.
12. Faber J, Kügler D, Bahrami E, Heinz LS, Timmann D, Ernst TM, et al. CerebNet: a fast and reliable deep-learning pipeline for detailed cerebellum sub-segmentation. Neuroimage. 2022;264:119703. https://doi.org/10.1016/j.neuroimage.2022.119703.
13. Schmitz-Hübsch T, du Montcel ST, Baliko L, Berciano J, Boesch S, Depondt C, et al. Scale for the assessment and rating of Ataxia: development of a new clinical scale. Neurology. 2006;66(11):1717–20.
14. Maas RPPWM, van Gaalen J, Klockgether T, van de Warrenburg BPC. The preclinical stage of spinocerebellar Ataxias. Neurology. 2015;85(1):96–103. https://doi.org/10.1212/WNL.0000000000001711.
15. Buckner RL, Head D, Parker J, Fotenos AF, Marcus D, Morris JC, et al. A unified approach for morphometric and functional data analysis in young, old, and demented adults using automated atlas-based head size normalization: reliability and validation against manual measurement of total intracranial volume. Neuroimage. 2004;23(2):724–38. https://doi.org/10.1016/j.neuroimage.2004.06.018.
16. Fortin JP, Parker D, Tunc B, Watanabe T, Elliott MA, Ruparel K, et al. Harmonization of multi-site diffusion tensor imaging data. NeuroImage. 2017;161:149–70. https://doi.org/10.1016/j.neuroimage.2017.08.047.
17. Fortin JP, Cullen N, Sheline YI, Taylor WD, Aselcioglu I, Cook PA, et al. Harmonization of cortical thickness measurements across scanners and sites. NeuroImage. 2018;167:104–20. https://doi.org/10.1016/j.neuroimage.2017.11.024.
18. Johnson WE, Li C. Adjusting batch effects in microarray expression data using empirical Bayes methods. Biostatistics. 2007;8(1):118–27. https://doi.org/10.1093/biostatistics/kxj037.
19. R Core Team. R: A language and environment for statistical computing. Vienna; 2023.
20. Faber J, Schaprian T, Berkan K, Reetz K, França MCJ, de Rezende TJR, et al. Regional brain and spinal cord volume loss in spinocerebellar Ataxia type 3. Mov Disord. 2021;36(10):2273–81. https://doi.org/10.1002/mds.28610.
21. Rezende TJR, de Paiva JLR, Martinez ARM, Lopes-Cendes I, Pedroso JL, Barsottini OGP, et al. Structural signature of SCA3: from presymptomatic to late disease stages. Ann Neurol. 2018;84(3):401–8. https://doi.org/10.1002/ana.25297.
22. Eichler L, Bellenberg B, Hahn HK, Köster O, Schöls L, Lukas C. Quantitative assessment of brain stem and cerebellar atrophy in spinocerebellar Ataxia types 3 and 6: impact on clinical status. AJNR Am J Neuroradiol. 2011;32(5):890–7. https://doi.org/10.3174/ajnr.A2387.
23. Arruda WO, Meira AT, Ono SE, de Carvalho Neto A, Betting LEGG, Raskin S, et al. Volumetric MRI changes in spinocerebellar Ataxia (SCA3 and SCA10) patients. Cerebellum. 2020;19(4):536–43. https://doi.org/10.1007/s12311-020-01137-3.
24. Schulz JB, Borkert J, Wolf S, Schmitz-Hübsch T, Rakowicz M, Mariotti C, et al. Visualization, quantification and correlation of brain atrophy with clinical symptoms in spinocerebellar Ataxia types 1, 3 and 6. NeuroImage. 2010;49(1):158–68. https://doi.org/10.1016/j.neuroimage.2009.07.027.
25. Lukas C, Schöls L, Bellenberg B, Rüb U, Przuntek H, Schmid G, et al. Dissociation of grey and white matter reduction in spinocerebellar Ataxia type 3 and 6: a voxel-based morphometry study. Neurosci Lett. 2006;408(3):230–235. Epub 2006 Sep 26. https://doi.org/10.1016/j.neulet.2006.09.007.
26. Faber J, Giordano I, Jiang X, Kindler C, Spottke A, Acosta-Cabronero J, et al. Prominent white matter involvement in multiple system Atrophy of cerebellar type. Mov Disord. 2020;35(5):816–24. https://doi.org/10.1002/mds.27987.
27. Oender D, Faber J, Wilke C, Schaprian T, Lakghomi A, Mengel D, et al. Evolution of clinical outcome measures and biomarkers in sporadic adult-onset degenerative Ataxia. Mov Disord. 2023;38(4):1654–64. https://doi.org/10.1002/mds.29324.
28. Schuster KH, Zalon AJ, Zhang H, DiFranco DM, Stec NR, Haque Z, et al. Impaired oligodendrocyte maturation is an early feature in SCA3 disease pathogenesis. J Neurosci. 2022;42(8):1604–17. https://doi.org/10.1523/JNEUROSCI.1954-20.2021.
29. Jacobi H, du Montcel ST, Bauer P, Giunti P, Cook A, Labrum R, et al. Long-term disease progression in spinocerebellar Ataxia types 1, 2, 3, and 6: a longitudinal cohort study. Lancet Neurol. 2015;14(11):1101–8. https://doi.org/10.1016/S1474-4422(15)00202-1.
30. Jäschke D, Steiner KM, Chang DI, Claaßen J, Uslar E, Thieme A, et al. Age-related differences of cerebellar cortex and nuclei: MRI findings in healthy controls and its application to spinocerebellar Ataxia (SCA6) patients. Neuroimage. 2023;270:119950. https://doi.org/10.1016/j.neuroimage.2023.119950.
31. Oender D, Faber J, Wilke C, Schaprian T, Lakghomi A, Mengel D, et al. Evolution of clinical outcome measures and biomarkers in sporadic adult-onset degenerative ataxia. Mov Disord. 2023;38(4):654–64. https://doi.org/10.1002/mds.29324.

Authors and Affiliations

Mónica Ferreira[1,2] · Tamara Schaprian[1] · David Kügler[1] · Martin Reuter[1,3,4] · Katharina Deike-Hoffmann[5] · Dagmar Timmann[6] · Thomas M. Ernst[6] · Paola Giunti[7,8] · Hector Garcia-Moreno[7,8] · Bart van de Warrenburg[9] · Judith van Gaalen[9,10] · Jeroen de Vries[11] · Heike Jacobi[12] · Katharina Marie Steiner[6] · Gülin Öz[13] · James M. Joers[13] · Chiadi Onyike[14] · Michal Povazan[14] · Kathrin Reetz[15,16] · Sandro Romanzetti[15] · Thomas Klockgether[1,17] · Jennifer Faber[1,17]

[1] German Center for Neurodegenerative Diseases (DZNE), Bonn, Germany

[2] Rhenish Friedrich Wilhelm University of Bonn, Bonn, Germany

[3] A.A. Martinos Center for Biomedical Imaging, Massachusetts General Hospital, Boston, MA, USA

[4] Department of Radiology, Harvard Medical School, Boston, MA, USA

[5] Department of Neuroradiology, University Hospital Bonn, Bonn, Germany

[6] Department of Neurology and Center for Translational Neuro- and Behavioral Sciences, University Hospital Essen, University of Duisburg-Essen, Duisburg, Germany

[7] Ataxia Centre, Department of Clinical and Movement Neurosciences, UCL Queen Square Institute of Neurology, London, UK

[8] National Hospital for Neurology and Neurosurgery, University College London Hospitals NHS Foundation Trust, London, UK

[9] Department of Neurology, Donders Institute for Brain, Cognition, and Behaviour, Radboud University Medical Center, Nijmegen, The Netherlands

[10] Neurology Department, Rijnstate Hospital, Arnhem, The Netherlands

[11] Department of Neurology, University Medical Center Groningen, University of Groningen, Groningen, The Netherlands

[12] Department of Neurology, University Hospital Heidelberg, Heidelberg, Germany

[13] Center for Magnetic Resonance Research, Department of Radiology, University of Minnesota, Minneapolis, MN, USA

[14] Johns Hopkins University School of Medicine, Baltimore, MD, USA

[15] Department of Neurology, RWTH Aachen University, Aachen, Germany

[16] JARA-Brain Institute Molecular Neuroscience and Neuroimaging, Forschungszentrum Jülich, Jülich, Germany

[17] Department of Neurology, University Hospital Bonn, Bonn, Germany

3.2 Publication 2: Progression of biological markers in spinocerebellar ataxia type 3 (DOI: 10.1016/j.lanepe.2025.101339)

Progression of biological markers in spinocerebellar ataxia type 3: longitudinal analysis of prospective data from the ESMI cohort

Moritz Berger,[a,b,ap] Hector Garcia-Moreno,[c,d,ap] Mónica Ferreira,[e,f,ap] Jeannette Hubener-Schmid,[g,ap] Tamara Schaprian,[e] Philipp Wegner,[e,f] Tim Elter,[d] Kennet M. Teichmann,[e] Magda M. Santana,[h,i,j] Marcus Grobe-Einsler,[e,k] Demet Oender,[e,k] Berkan S. C. Koyak,[e,k] Sarah Bernsen,[e,k] Luís Pereira de Almeida,[h,i,j] Patrick Silva,[h,i,j] Joana Afonso Ribeiro,[l] Inês Cunha,[m] Cristina Gonzalez-Robles,[c] Shamsher Khan,[c] Amanda Heslegrave,[n,o] Henrik Zetterberg,[n,o,p] Manuela Lima,[q,r] Mafalda Raposo,[s,t] Ana F. Ferreira,[q,r] João Vasconcelos,[u] Bart P. van de Warrenburg,[v] Judith van Gaalen,[v,w] Teije H. van Prooije,[v] Jeroen de Vries,[x] Ludger Schols,[y,z] Olaf Riess,[g] Matthis Synofzik,[z,aa] Dagmar Timmann,[ab] Andreas Thieme,[ab] Friedrich Erdlenbruch,[ab] Jon Infante,[ac,ad] Ana L. Pelayo-Negro,[ac,ad] Leire Manrique,[ae] Kathrin Reetz,[af,ag] Imis Dogan,[af,ag] Gulin Oz,[ah] James M. Joers,[ah] Khalafalla Bushara,[ai] Chiadikaobi Onyike,[aj] Michal Povazan,[ak] Heike Jacobi,[al] Jeremy D. Schmahmann,[am] Eva-Maria Ratai,[an] Matthias Schmid,[a,e] Paola Giunti,[c,d,***] Thomas Klockgether,[e,**] and Jennifer Faber[e,k,ao,*]

[a]Medical Faculty, Institute for Medical Biometry, Informatics and Epidemiology, University of Bonn, Bonn, Germany
[b]Core Facility Biostatistics, Central Institute of Mental Health, Medical Faculty Mannheim, Heidelberg University, Mannheim, Germany
[c]Department of Clinical and Movement Neurosciences, UCL Queen Square Institute of Neurology, Ataxia Centre, University College London, London WC1N 3BG, UK
[d]Department of Neurogenetics, National Hospital for Neurology and Neurosurgery, University College London Hospitals NHS Foundation Trust, London WC1N 3BG, UK
[e]German Center for Neurodegenerative Diseases (DZNE), Bonn, Germany
[f]University of Bonn, Bonn, Germany
[g]Institute for Medical Genetics and Applied Genomics, University of Tuebingen, Tuebingen, Germany
[h]Center for Neuroscience and Cell Biology, University of Coimbra (CNC-UC), Coimbra, Portugal
[i]Center for Innovative in Biomedicine and Biotechnology (CIBB), University of Coimbra, Coimbra, Portugal
[j]Gene Therapy Center of Excellence (GeneT), Coimbra, Portugal
[k]Department of Parkinson’s Disease, Sleep and Movement Disorders, Center for Neurology, University Hospital Bonn, Bonn, Germany
[l]Department of Neurology, Child Development Centre, Coimbra University Hospital Center (CHUC), Coimbra, Portugal
[m]Department of Neurology, Coimbra University Hospital Center (CHUC), Coimbra, Portugal
[n]Department of Neurodegenerative Disease, UCL Queen Square Institute of Neurology, London WC1N 3BG, UK
[o]UK Dementia Research Institute at UCL, London, UK
[p]Department of Psychiatry and Neurochemistry, Institute of Neuroscience and Physiology, The Sahlgrenska Academy at the University of Gothenburg, S-431 80, Mölndal, Sweden
[q]Faculdade de Ciências e Tecnologia, Universidade dos Açores, Ponta Delgada, Portugal
[r]UMIB - Unit for Multidisciplinary Research in Biomedicine, ICBAS - School of Medicine and Biomedical Sciences, University of Porto, Porto, Portugal
[s]Instituto de Biologia Molecular e Celular (IBMC), Instituto de Investigação e Inovação em Saúde (i3S), Universidade do Porto, Porto, Portugal
[t]Faculdade de Ciências e Tecnologia, Universidade dos Açores, Ponta Delgada, Portugal
[u]Hospital CUF Açores, Lagoa, Portugal
[v]Department of Neurology, Donders Institute for Brain, Cognition, and Behaviour, Radboud University Medical Center, Nijmegen, the Netherlands
[w]Department of Neurology, Rijnstate Hospital, Arnhem, the Netherlands
[x]Department of Neurology, University Medical Center Groningen, Groningen, the Netherlands
[y]Department of Neurodegenerative Diseases, Hertie Institute for Clinical Brain Research & Center of Neurology, University of Tuebingen, Tuebingen, Germany
[z]German Center for Neurodegenerative Diseases (DZNE), Tuebingen, Germany
[aa]Division Translational Genomics of Neurodegenerative Diseases, Hertie Institute for Clinical Brain Research & Center of Neurology, University of Tuebingen, Germany
[ab]Department of Neurology and Center for Translational Neuro- and Behavioral Sciences (C-TNBS), University Hospital Essen, University of Duisburg-Essen, Essen, Germany

---

DOI of original article: https://doi.org/10.1016/j.lanepe.2025.101374

*Corresponding author. Venusberg-Campus 1/99, Bonn 53127, Germany.
**Corresponding author. Venusberg-Campus 1/99, Bonn 53127, Germany.
***Corresponding author. Institute of Neurology Queen Square, UCL Queen Square, London WC1N 3BG, UK.
E-mail addresses: Jennifer.faber@dzne.de (J. Faber), klockgether@uni-bonn.de (T. Klockgether), p.giunti@ucl.ac.uk (P. Giunti).

[ap]Contributed equally.

[ac]University Hospital Marqués de Valdecilla-IDIVAL, Santander, Spain
[ad]Centro de Investigación Biomédica en Red de Enfermedades Neurodegenerativas (CIBERNED), Universidad de Cantabria, Santander, Spain
[ae]University Hospital of Navarra, Pamplona, Spain
[af]Department of Neurology, RWTH Aachen University, Pauwelsstr. 30, Aachen 52074, Germany
[ag]JARA-BRAIN Institute Molecular Neuroscience and Neuroimaging, Research Centre Juelich GmbH and RWTH Aachen University, Aachen 52074, Germany
[ah]Department of Radiology, Center for Magnetic Resonance Research, University of Minnesota, Minneapolis, MN, USA
[ai]Department of Neurology, University of Minnesota Medical School, Minneapolis, MN, USA
[aj]Department of Psychiatry and Behavioral Sciences, Johns Hopkins University School of Medicine, Baltimore, MD, USA
[ak]Johns Hopkins University School of Medicine, Baltimore, MD 21205, USA
[al]Department of Neurology, University Hospital of Heidelberg, Heidelberg, Germany
[am]Laboratory for Neuroanatomy and Cerebellar Neurobiology, Ataxia Center, Massachusetts General Hospital and Harvard Medical School, MA, USA
[an]Department of Radiology, A. A. Martinos Center for Biomedical Imaging and Harvard Medical School, Massachusetts General Hospital, Charlestown, MA, USA
[ao]Department of Neuroradiology, University Hospital Bonn, Bonn, Germany

The Lancet Regional Health - Europe
2025;55: 101339

https://doi.org/10.1016/j.lanepe.2025.101339

Summary

Background Spinocerebellar ataxia type 3 (SCA3) is an autosomal dominantly inherited adult-onset disease. We aimed to describe longitudinal changes in clinical and biological findings and to identify predictors for clinical progression.

Methods We used data from participants enrolled in the ESMI cohort collected between Nov 09, 2016 and July 18, 2023. The data freeze included data from 14 sites in five European countries and the United States. We assessed ataxia with the Scale for the Assessment and Rating of Ataxia (SARA). We measured disease-specific mutant ataxin-3 protein (ATXN3) and neurofilament light chain (NfL) in plasma and performed MRIs. Data were analysed by regression modelling on a timescale defined by onset. The onset of abnormality of a marker was defined as the time at which its value, as determined by modelling, exceeded the mean ± 2 SD of healthy controls. To study responsiveness of markers, we determined the sensitivity to change ratios (SCSs).

Findings Data from 291 SCA3 mutation carriers before and after clinical onset and 121 healthy controls were included. NfL levels became abnormal in SCA3 mutation carriers more than 20 years (–21.5 years [95% CI n.d.–9.5]) before onset. The earliest MRI abnormality was volume loss of medulla oblongata (–4.7 years [95% CI n.d.–3.3]). The responsiveness of markers depended on the disease stage. Across all stages, pons volume had the highest responsiveness with an SCS of 1.35 [95% CI 1.11–1.78] exceeding that of SARA (0.99 [95% CI 0.88–1.11]). In SCA3, lower age ($p = 0.0459$ [95% CI of slope change –0.0018 to 0.0000]) and lower medulla oblongata volume ($p < 0.0001$ [95% CI of slope change –0.0298 to –0.0115]) were predictors of SARA progression.

Interpretation Our study provides quantitative information on the progression of biological markers in SCA3 mutation carriers before and after onset of ataxia, and allowed the identification of predictors for clinical progression. Our data could prove useful for the design of future clinical trials.

Funding HEU Joint Programme – Neurodegenerative Disease Research (JPND) (Federal Ministry of Education and Research, Germany; The Netherlands Organisation for Health Research and Development; Foundation for Science and Technology, Portugal; Medical Research Council, Regional Fund for Science and Technology, Azores), and Servier. At the US sites this work was in part supported by the National Ataxia Foundation and the National Institute of Neurological Disorders and Stroke (NINDS) grant R01NS080816.

Keywords: Spinocerebellar ataxia; MRI; NfL; ATXN3; Disease modelling; Staging model; Biomarker

Research in context

Evidence before this study

We searched Medline and ISI Web of Science for reports published before Nov 30, 2024, with the search terms [“spinocerebellar ataxia type 3” AND “biomarker” OR “ATXN3” OR “neurofilament light chain (NfL)” OR “MRI” AND “prospective” OR “follow-up” OR “longitudinal“]. Only peer-reviewed, English-language reports of human cohort studies with at least 10 participants were considered. In a previous analysis of 33 SCA3 mutation carriers from this cohort, plasma concentrations of mutant ATXN3 remained stable over one year. In a two-year follow-up study of 19 SCA3 patients, NfL concentration did not change. Six studies with participant numbers ranging from 17 to 23 and follow-up times from six months to five years found progressive atrophy of a number of brain structures and cervical spinal cord, as well as increasing abnormalities of diffusion parameters of a number of brain fibre tracts.

Added value of this study

In this European, longitudinal registry study (ESMI), we prospectively investigated a large cohort of SCA3 mutation carriers before and after onset. We determined the sequence and extent of plasma mutant ATXN3 and NfL, as well as MRI measure changes along the disease course. This study is, to the best of our knowledge, the first to comprehensively study multimodal biological markers longitudinally over the entire disease course of SCA3. Our data allowed to determine the onset of abnormality of the studied biological markers, define their stage-specific sensitivity to change, and identify predictors for clinical progression.

Implications of all the available evidence

The available data provide quantitative information on the progression of biological markers in SCA3 mutation carriers before and after the onset of ataxia, and allow the identification of predictors of clinical progression. Knowledge of the progression of biological markers in these individuals can help researchers to design trials of interventions aimed at slowing clinical progression or delaying the onset of ataxia.

Introduction

Spinocerebellar ataxia type 3 (SCA3) is the most common autosomal dominantly inherited adult-onset ataxia disease worldwide. SCA3 takes a progressive course and leads to increasing disability and premature death. It is caused by unstable expansions of polyglutamine encoding CAG repeats within the *ATXN3* gene, resulting in the formation of abnormally elongated, misfolded ataxin-3 protein (ATXN3).[1]

Targeted therapies for SCA3 are being developed, and first safety trials of antisense oligonucleotides (ASOs) have been initiated (https://clinicaltrials.gov, NCT05160558, NCT05822908). In the future, preventive intervention in mutation carriers before clinical onset will be a realistic option.[2] With the advent of disease-modifying treatments for SCA3, there is the need to identify biological markers that are sensitive to disease-related change before and after clinical manifestation. Mutant ATXN3 can be measured at low concentrations in the CSF and plasma of mutation carriers, but is absent in healthy controls.[3,4] Blood neurofilament light chain (NfL) is an easily accessible, non-specific marker of neurodegeneration.[5] In cross-sectional studies, NfL was increased in patients and in mutation carriers before onset.[6–10] In a two-year follow-up study of 19 SCA3 patients, the increased NfL concentrations did not change.[9] In longitudinal MRI studies of SCA3 mutation carriers, progressive atrophy of the cerebellum, pons, mesencephalon, and cervical spinal cord was observed.[11–14] In addition, diffusion parameters of cerebellar peduncles, superior longitudinal fasciculus, corona radiata, and medial lemniscus showed increasing abnormalities.[13–15]

The European Spinocerebellar ataxia type 3/ Machado-Joseph disease Initiative (ESMI) initiated a longitudinal registry study of SCA3 mutation carriers before and after clinical onset representing a wide spectrum of disease severity. Analysis of cross-sectional clinical, as well as fluid biomarker and MRI volumetric data allowed to draft a data-driven model of disease stages for SCA3.[16] In the present study, we describe longitudinal changes of mutant ATXN3, NfL and several MRI measures that were abnormal in SCA3 mutation carriers before onset. We focused the analysis on determining stage-specific sensitivity of biological markers and identifying predictors of clinical progression.

Methods

Study design and participants

The study population of the ESMI registry study consists of (1) SCA3 mutation carriers before and after onset, (2) persons at risk to carry the SCA3 mutation (first degree relatives of SCA3 patients) who have not been diagnostically tested, and who do not wish to be tested, and (3) healthy controls (including spouses, unrelated persons, and persons at risk who were negatively tested). The genetic status of persons at risk (first degree relatives of SCA3) was assessed within a central scientific genetic testing. Results of these central scientific genetic tests were used to assign persons at risk either to the

SCA3 mutation carrier or healthy control group, but not disclosed to the study participants.

The ESMI registry study is conducted at 14 sites in five European countries and the United States. Participants undergo annual standardized assessments including clinical examination and biosample collection. MRI is performed at 11 sites.

Procedures

We used the Scale for the Assessment and Rating of Ataxia (SARA)[17] to assess the presence and severity of ataxia. Manifest ataxia was defined by a score of ≥ 3.[17,18]

Analysis of the CAG repeat length of the *ATXN3* gene was performed at the Department of Medical Genetics of the University of Tübingen (Tübingen, Germany). Determinations were done for 243 mutation carriers and 20 persons at risk who had not been diagnostically tested. For 42 SCA3 mutation carriers, from whom no DNA was available, information about CAG repeat lengths was taken from medical records; in eight participants, no information on repeat length was available.

Plasma concentrations of mutant ATXN3 were measured using an ultrasensitive immunoassay based on the SMC® technology.[3] Plasma concentrations of NfL were determined with the Neurology 4-Plex A assay (N4PA) (Quanterix, Billerica, MA, United States) run on the Simoa HD-X Analyzer™.[7] Samples were analysed using two different assay lots. For each sample, measurements were performed in split duplicates, and the average values were calculated.

T1-and diffusion weighted MRIs were acquired on Siemens 3T scanners (Siemens Medical Systems, Erlangen, Germany). As imaging biological markers, we calculated 61 brain volumes including brainstem and cerebellar sub-segments and the mean diffusion metrics (fractional anisotropy (FA), medial diffusivity (MD), axial (AD) and radial diffusivity (RD)) of 14 white matter tracts. Details of the MR sequences and imaging analysis as well as a comprehensive list of all studied volumes and white matter tracts are given in the Appendix pp 4–5.

Definition of axes and disease stages

Age of onset was defined as the reported first occurrence of gait disturbances.[19] The onset of reported gait disturbances is different from the time of conversion to manifest ataxia, defined by a SARA cut-off of ≥3.The time of onset defined as the time of the first occurrence of gait abnormalities reported by a mutation carrier has been used, because (i) it refers to a reference time point that can be determined retrospectively, while the observed conversion of SARA to values ≥3 is only available in a minority of cases, (ii) it represents a core symptom of ataxia which appears in all patients, and is a milestone with relevance to the patient, (iii) mathematical models, related to the reported onset of gait disturbances are available and allow to estimate the time to onset in mutation carriers, not yet experiencing gait disturbances (negative values).[20] In contrast, SARA is an examiner-based assessment of ataxia severity. As mentioned above, there are currently not enough data sets available with observed changes from values < 3 to values ≥ 3, that would allow to establish estimation models. 36 SCA3 mutation carriers had not yet experienced gait disturbances (right-censored individuals). In nine SCA3 mutation carriers with gait disturbance, information on the reported age of onset was missing (left-censored individuals). In these 45 SCA3 mutation carriers, the age of onset was estimated, as described below.

For regression, NfL concentrations and MRI measures were z-transformed with respect to age and sex. Z-scores of MRI volumes and FA values were inverted, so that higher z-scores indicate increasing abnormality in all measures. Since SARA scores and mutant ATXN3 in healthy controls were close to 0, no z-transformation was performed, and the raw values were used. A Box-Cox transformation with parameter $\lambda = 0.25$ was applied to the SARA score to approximate normality. Following recently proposed definitions of SCA3 disease stages,[16] SCA3 mutation carriers were assigned to the carrier stage (SARA <3 and NfL z-score <2), biomarker stage (SARA <3 and NfL z-score ≥2), or ataxia stage (SARA ≥3).

Statistical analysis

General statistical approach

Statistical analysis was carried out using R version 4.3.1 (R Core Team 2023: R: A Language and Environment for Statistical Computing, R Foundation for Statistical Computing, Vienna, Austria).

The selection of MRI parameters was based on the group comparison between pre-ataxic SCA3 mutation carriers with a SARA <3 and healthy controls using linear regression models. Details on the statistical methods and test results are given in the Appendix pp 6–7.

Five NfL values, one ATXN3 value, and one pons volume value were excluded as outliers after visual inspection of the data (Appendix p 2).

To relate fluid and MRI biomarker data to the time from onset, we applied a conditional multiple imputation approach.[16] First, censored values of age of onset were imputed fitting a previously published parametric survival model.[20] For this, the last follow-up visit of each participant was considered and the time from onset for towards each visit date was then calculated respectively. To account for censoring, age of onset was imputed with the conditional expectation for right-censored individuals (accounting for actual age) and with the unconditional expectation for left-censored individuals. Second, SARA score and biological markers were regressed on the (imputed) time from onset using additive mixed regression models with participant-specific random intercepts and a cubic P-spline with six B-spline basis functions and a second-order difference penalty. This two-step procedure was repeatedly applied to 1000 bootstrap samples from the original sample. Final estimates of the spline coefficients and associated variance estimates were then calculated by applying Rubin's rule.

Onset of abnormality in fluid and MRI markers

A biological marker was considered abnormal, if its value, as determined by modelling, exceeded the normal range defined by mean ± 2 SD in healthy controls. Onset of abnormality was defined as not determinable (n.d.) if the intersection between the normal range and the fitted spline function of the upper and lower limit of the 95% CI, respectively, was not reached within the time interval of observations (33 years before to 41 years after onset).

Sensitivity to change of clinical, fluid and MRI measures

Responsiveness of SARA and biological markers was assessed by calculating sensitivity to change ratios (SCSs).[21] To this end, linear mixed regression models with the (imputed) time from onset as the time variable and participant-specific random intercepts were fitted for the entire disease course and each stage (carrier, biomarker, ataxia), respectively. SCSs were then calculated by dividing the estimated slopes of progression by the estimated standard deviation of the slopes. 95% CIs of the SCSs were determined by non-parametric bootstrap based on 1000 samples. Higher SCS values indicate greater sensitivity to change of the respective measure.

Predictors of clinical *progression*

For prediction of SARA increase, we applied univariable and multivariable mixed regression models with the Box-Cox transformed SARA as outcome and age, sex, CAG repeat length of the expanded allele and the baseline values of the biological markers as covariates. We tested the effect of these factors on SARA progression by interactions with the time variable (time from onset). The multivariable model was selected by stepwise selection with the Bayesian information criterion including all covariates with $p < 0.05$ in univariable models (or $p < 0.15$, see Appendix p 11). We conducted the univariable analysis for the entire disease course and each stage (carrier, biomarker, ataxia), respectively, while we restricted the multivariable model to the entire disease course to ensure a sufficiently large sample size.

Ethic approval

The study was approved by the ethics committees of all contributing centres. Approval numbers and dates for the leading national site: London, UK: Research Ethics Committee (REC) name: London–Chelsea Research Ethics Committee; REC Reference number: 17/LO/0381; Approval date: 28/04/2017; Bonn, Germany: Ethics committee, Medical Faculty, University of Bonn, 176/16; date of approval: 11th Oct 2016, Amendment1 17th Sep 2020, Amendment2: 27th Aug 2024; Nijmegen, The Netherlands: CMO (Regio Arnhem-Nijmegen); European Spinocerebellar Ataxia Type 3/Machado-Joseph Disease (ESMI); 2016–2554 (local), NL25267.091.16 (national); Approval date: April 3rd, 2017; Santander, Spain: COMITÉ DE ÉTICA DE LA INVESTIGACIÓN CON MEDICAMENTOS DE CANTABRIA; 2018.282, Date of approval: 01/02/2019 and 26/04/2021 (Amendment 1); Coimbra, Portugal: Ethics committee of the Faculty of Medicine of the University of Coimbra. Date of approval: CE-085/2017 (date 25.09.2017), amendment CE-121/2020 (date 20.01.2020); Minnesota, USA: Ethics committee Univ. of Minnesota, IRB study number 0502M67488, date of approval: June 9, 2017). At enrolment, informed and written consent following the Declaration of Helsinki was obtained from all study participants. The study protocol is available online (https://ataxia-esmi.eu/study-protocols).

Role of the funding source

The study funders had no role in study design, data collection, data analysis, data interpretation, or writing of the report. The corresponding authors had full access to all the data in the study and had final responsibility for the decision to submit for publication.

Results

Enrolment and cohort characteristics

Between Nov 09, 2016, and Jul 18, 2023, we enrolled 419 participants with at least one available biological marker. Seven participants and biomarker data from 39 visits were excluded. A flow chart detailing the reasons is given in the Appendix p 2. Eventually, 291 SCA3 mutation carriers and 121 healthy controls were included in the analysis. Among the SCA3 mutation carriers, 55 had no ataxia (SARA <3), and 236 had ataxia (SARA ≥3) at baseline. At baseline, mutant ATXN3 concentrations were available in 97, NfL concentrations in 303, and MRI results in 171 participants. Baseline characteristics of the study participants and the subgroups with available biological markers are given in Table 1.

Data from 856 visits were analysed. Participants had a median number of 2 (IQR 1–3) visits and a median observation time of 1.02 years (0.00–2.03). Hundred-and-two SCA3 mutation carriers and 33 healthy controls completed one follow-up visit, 64 mutation carriers and 14 healthy controls two follow-up visits, and 31 mutation carriers and 13 healthy controls three to five follow-up visits. The Appendix details the availability of ATXN3, NfL and MRI data at the follow-up visits (Appendix p 3).

	Healthy controls	SCA3 mutation carriers with SARA < 3	SCA3 mutation carriers with SARA ≥ 3
Total group (n = 412)			
Number of participants	121 (29%)	55 (13%)	236 (57%)
Women	71 (59%)	30 (55%)	113 (48%)
Age, years	44.6 (34.3–56.3)	34.6 (29.1–39.9)	52.2 (45.2–60.3)
SARA score	0.0 (0.0–0.5)	1.0 (0.5–2.0)	12.0 (8.5–19.0)
Length of expanded CAG allele	n.a.	68 (65–71)	69 (66–71)
Time from onset, years	n.a.	−12.5 (−16.8 to −0.0)	10.1 (5.6–14.9)
ATXN3 subgroup (n = 97)			
Number of participants	10 (10%)	14 (14%)	73 (76%)
Women	6 (60%)	8 (57%)	29 (40%)
Age, years	49.1 (31.8–57.5)	34.2 (29.4–37.6)	51.6 (44.9–60.2)
SARA score	0.0 (0.0–0.0)	1.0 (0.3–1.5)	10.5 (7.5–16.5)
Length of expanded CAG allele	n.a.	69 (65–71)	69 (64–71)
Time from onset, years	n.a.	−14.6 (−18.1 to −10.7)	8.3 (4.9–13.2)
NfL subgroup (n = 303)			
Number of participants	92 (30%)	32 (10%)	179 (59%)
Women	55 (60%)	18 (56%)	90 (50%)
Age, years	44.8 (35.7–56.6)	34.2 (26.2–39.7)	51.9 (45.3–59.7)
SARA score	0.0 (0.0–0.7)	1.0 (0.5–1.6)	13.0 (8.5–20.6)
Length of expanded CAG allele	n.a.	69 (66–71)	69 (66–72)
Time from onset, years	n.a.	−12.6 (−16.7 to −2.7)	10.9 (6.4–15.9)
MRI subgroup (n = 171)			
Number of participants	45 (26%)	32 (19%)	94 (55%)
Women	25 (56%)	21 (66%)	38 (40%)
Age, years	45.8 (32.7–56.3)	34.2 (29.5–40.8)	51.8 (45.3–58.2)
SARA score	0.0 (0.0–0.5)	1.0 (0.4–2.0)	10.0 (8.0–14.5)
Length of expanded CAG allele	n.a.	68. (65–71)	69 (67–71)
Time from onset, years	n.a.	−12.3 (−17.6 to 2.0)	8.7 (4.6–12.6)

Data are n, n (%), or median (IQR). NfL = neurofilament light chain. SARA = Scale for the Assessment and Rating of Ataxia.

Table 1: **Baseline characteristics of study participants.**

Baseline results of ATXN3 concentrations, NfL concentrations, and MRI measures are given in Appendix p 8. Mutation carriers without ataxia had higher ATXN3 and NfL concentrations, lower medulla oblongata, pons, midbrain, cerebellar white matter (CWM), and superior cerebellar peduncle (SCP) volumes, reduced FA inferior cerebellar peduncle (ICP) and FA SCP, and increased RD ICP values than healthy controls. Because our focus was on early disease stages, we took into account only those MRI measures, which were altered in mutation carriers without ataxia in comparison to healthy controls (Appendix p 7). In addition, we included cerebellar grey matter (CGM) volume, to be consistent with the previously published cross-sectional analysis of this cohort.[16]

At baseline, nine of the SCA3 mutation carriers were in the carrier stage, 23 in the biomarker stage, and 236 in the ataxia stage. Twenty-three mutation carriers without ataxia could not be assigned to a disease stage, because NfL concentrations were not available. Within the observation period, two mutation carriers converted from the carrier to the biomarker stage, and seven from the biomarker to the ataxia stage. On the other hand, one mutation carrier assigned to the biomarker stage at baseline was assigned to the carrier stage at the final visit. Further, three mutation carriers, which were scored as ataxic at baseline, were assigned to earlier stages at the final visit: two to the biomarker and one to the carrier stage.

Onset of abnormality of fluid and MRI markers

Progression of SARA scores, mutant ATXN3, NfL concentrations, and MRI measures of SCA3 mutation carriers in relation to the time from onset are shown as modelled curves in Fig. 1. The original data displayed as spaghetti plots are given in the Appendix p 9.

SARA progression had a sigmoidal shape (Fig. 1A). Scores crossed the cut-off of 3, which defines the onset of the ataxia stage, 4.2 years [95% CI n.d.–0.9] before the reported or estimated onset of gait disturbances (Table 2). At the time of onset of gait disturbances, the SARA score was 4.7 [2.5–7.9]. Mutant ATXN3 concentrations were constant throughout the entire disease course without major changes over time so that the onset of abnormality could not be determined (Fig. 1B). NfL concentrations increased throughout the disease course, but the increase slowed down after onset (Fig. 1C). NfL values became abnormal more than 20 years (−21.5 years [n.d. to −9.5]) before onset (Table 2). All analysed MRI volumes and diffusion measures worsened over time, albeit at different rates and with different slopes (Fig. 1D–F). Medulla oblongata volume (−4.7 years [n.d. to +3.7]), FA ICP (−2.1 years [−10.3 to 2.7]), and pons volume (−0.6 years [−6.4 to 3.8]) became abnormal before onset. The remaining MRI measures became abnormal 0.3–14.4 years after onset in the following temporal order: RD ICP, CWM volume, midbrain volume, SCP volume, and FA SCP. CGM value did not decrease more than 2 SD below the mean of healthy controls throughout the entire disease course (Table 2). Compared to our previous cross-sectional analysis, in which we determined the upper 95% CI limits of NfL, pons volume, and CWM volume, the onset of abnormality of these measures was 3.8–6.5 years later. To clarify the reason for this difference, we calculated the upper 95% CI limits of NfL, pons volume, and CWM volume based alone on the baseline values of the present dataset. These values differed only by 1.1–3.2 years from the previously determined values (Appendix p 12).

Sensitivity to change of clinical, fluid and MRI measures

To determine the responsiveness of the studied measures, we calculated the SCSs. For the entire disease, all measures except ATXN3 had SCSs larger than 0. The most sensitive measure was pons volume with an SCS of 1.35 [95% CI 1.11–1.78]. Further stage-specific analyses showed that the SCSs of the various outcome measures depended on the disease stage. In the carrier

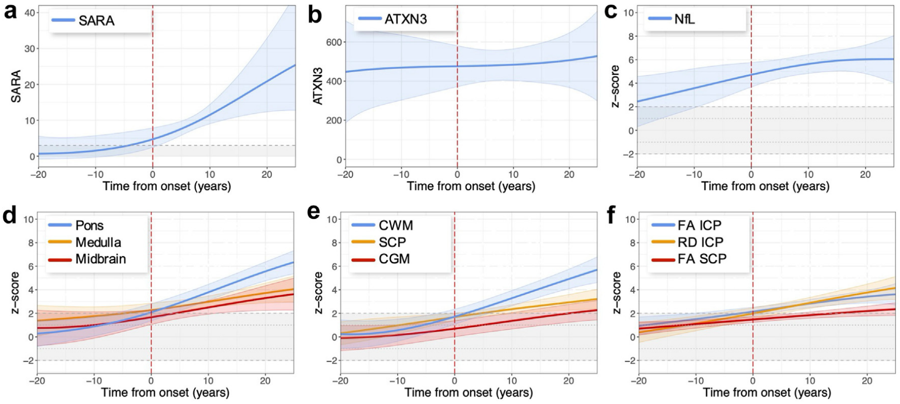

Fig. 1: Progression of (a) SARA, (b) ATXN3, (c) NfL, (d) MRI brainstem volumes, (e) MRI cerebellar volumes, and (f) MRI diffusion measures in SCA3. Data were analysed by additive mixed regression models with participant-specific random intercepts on a timescale defined by onset of gait disturbances (vertical dashed line in red) using a cubic P-spline with six B-spline basis functions. The estimated 95% CIs are shown by the shaded areas around the curves. NfL and MRI data were z-transformed in relation to healthy controls. Z-scores of MRI volumes and FA values were inverted for a better visualisation. The horizontal ribbon shaded in grey indicates the normal range (±2) of the z-transformed measures (NfL, MRI measures) of healthy controls. For SARA the applied cut-off of 3 is indicated by a dotted horizontal line. CGM = cerebellar grey matter. CWM = cerebellar white matter. FA ICP = fractional anisotropy of the inferior cerebellar peduncle. FA SCP = fractional anisotropy of the superior cerebellar peduncle. NfL = neurofilament light chain. RD ICP = radial diffusivity of the inferior cerebellar peduncle. SCP = superior cerebellar peduncle.

Outcome	Onset of abnormality in years	95% CI
Clinical		
SARA	−4.2	n.d.–0.9
Fluid		
Mutant ATXN3	n.d.	n.d.–n.d.
NfL	−21.5	n.d. to −9.5
MRI volume		
Medulla oblongata	−4.7	−n.d. to 3.7
Pons	−0.6	−6.4 to 3.8
Midbrain	4.1	n.d.–11.4
CWM	2.0	−3.0 to 5.9
CGM	n.d.	9.4–n.d.
SCP	4.6	0.1–10.8
MRI diffusion measures		
FA ICP	−2.1	−10.3 to 2.7
RD ICP	0.3	−6.4 to 5.0
FA SCP	14.4	7.7–n.d.

The onset of abnormality of a marker was defined as the time at which its value, as determined by modelling, exceeded the mean ± 2 SD of healthy controls. All outcomes except SARA and ATXN3 were z-transformed. Z-scores of MRI volumes and FA values were inverted. For SARA, the time point, at which the score crossed the cut-off of 3 are shown. CGM = cerebellar grey matter. CWM = cerebellar white matter. FA ICP = fractional anisotropy of inferior cerebellar peduncle. FA SCP = fractional anisotropy of superior cerebellar peduncle. n.d. = not determinable. NfL = neurofilament light chain. RD ICP = radial diffusivity inferior cerebellar peduncle. SARA = Scale for the Assessment and Rating of Ataxia. SCP = superior cerebellar peduncle.

***Table 2:* Onset of abnormality of SARA, ATXN3, NfL, and MRI measures in SCA3.**

stage, the SCSs of SCP volume (0.62 [0.04–1.05]) and FA SCP (0.45 [0.17–0.92]) were larger than 0, whereas the SCSs of SARA and all other analysed biological markers did not differ from 0. In the biomarker stage, SCSs of SARA, NfL, all MRI volumes except midbrain, and RD ICP were larger than 0. In this stage, pons volume had the highest SCS of all outcome measures (1.41 [0.64–3.29]), followed by SCP (0.81 [0.34–1.64]) and CWM volume (0.78 [0.11–1.73]). Pons volume also had the highest SCS in the ataxia stage (1.71 [1.32–2.45]). It markedly exceeded the SCS of SARA (0.69 [0.60–0.80]). In the ataxia stage, the SCSs of NfL and FA SCP did not differ from 0, whereas all other biological markers had SCSs larger than 0 (Table 3).

Predictors of clinical progression

To identify factors that predicted SARA progression we applied univariable and multivariable modelling. In the univariable analysis of the entire disease, lower age, larger CAG repeat length, and lower volumes of medulla oblongata, midbrain, CGM, and SCP were associated with faster SARA progression. In the carrier stage, lower age, female sex, higher ATXN3 levels, larger CAG repeat length, and lower medulla oblongata and CWM volumes were predictors, in the ataxia stage, lower age, larger CAG repeat length, and lower medulla oblongata, midbrain and CGM volumes. In the biomarker stage, we did not find significant predictors (Appendix pp 10–11). The

Outcome measure	Entire disease	Carrier stage	Biomarker stage	Ataxia stage
Clinical				
SARA	0.99 (0.88–1.11)	0.07 (−0.25 to 0.52)	0.37 (0.19–0.59)	0.69 (0.60–0.80)
Fluid				
Mutant ATXN3	0.04 (−0.11 to 0.20)	0.09 (−0.78 to 7.61)	−0.11 (−1.55 to 0.72)	0.10 (−0.01 to 0.21)
NfL	0.21 (0.14–0.30)	0.51 (−0.11 to 1.28)	0.63 (0.37–0.99)	0.08 (−0.03 to 0.19)
MRI volume				
Medulla oblongata	0.48 (0.33–0.73)	0.20 (−0.56 to 0.60)	0.52 (0.04–1.20)	0.30 (0.13–0.75)
Pons	1.35 (1.11–1.78)	0.19 (−0.11 to 0.50)	1.41 (0.64–3.29)	1.71 (1.32–2.45)
Midbrain	0.49 (0.34–0.80)	−0.18 (−0.59 to 0.12)	0.31 (−0.17 to 0.89)	0.40 (0.16–1.00)
CWM	1.01 (0.85–1.23)	−0.03 (−0.54 to 0.22)	0.78 (0.11–1.73)	1.10 (0.84–1.48)
CGM	0.64 (0.50–0.80)	0.00 (−0.25 to 0.49)	0.48 (0.19–0.79)	0.72 (0.54–0.93)
SCP	0.69 (0.52–0.94)	0.62 (0.04–1.05)	0.81 (0.34–1.64)	0.30 (0.14–0.53)
MRI diffusion measures				
FA ICP	0.56 (0.44–0.67)	0.11 (−0.22 to 0.40)	0.24 (−0.03 to 0.58)	0.17 (0.03–0.32)
RD ICP	0.56 (0.44–0.71)	0.17 (−0.08 to 0.70)	0.51 (0.17–1.02)	0.24 (0.09–0.40)
FA SCP	0.38 (0.22–0.58)	0.45 (0.17–0.92)	0.26 (−0.06 to 0.54)	0.04 (−0.11 to 0.23)

Data are the estimated slope of progression (95% CI). CWM = cerebellar white matter. FA ICP = fractional anisotropy of inferior cerebellar peduncle. FA SCP = fractional anisotropy of superior cerebellar peduncle NfL = neurofilament light chain. RD ICP = radial diffusivity inferior cerebellar peduncle. SARA = Scale for the Assessment and Rating of Ataxia. SCP = superior cerebellar peduncle.

Table 3: **Stage-specific sensitivity to change (SCS) of SARA, ATXN3, NfL, and MRI measures in SCA3.**

multivariable analysis of the entire disease course selected lower age (p = 0.0459, slope change −0.0009 [95% CI of slope change −0.0018 to 0.0000]) and lower medulla oblongata volume (p < 0.0001, slope change −0.0208 [95% CI of slope change −0.0298 to −0.0115]) as predictors of SARA progression (Fig. 2, Appendix p 11).

Discussion

This longitudinal study determined the sequence and extent of plasma mutant ATXN3, plasma NfL and MRI outcome measure changes along the SCA3 disease course in participants of the ESMI cohort. We analysed the data in the framework of the recently proposed SCA3 staging model that distinguishes an asymptomatic carrier stage, a biomarker stage and the final ataxia stage.[16]

The present analysis showed that pre-ataxic SCA3 mutation carriers on average entered the biomarker stage 21.5 years before clinical onset with an upper margin of the 95% CI of 9.5 years before onset. The moderate difference to the previously reported time of 13.3 years is most likely due to the fact that we now analysed longitudinal data, while the previous analysis was based on cross-sectional data.[16] The ataxia stage started 4.2 years before the onset, defined by the estimated or reported onset of gait abnormalities. In the RISCA study, the observed conversion of SCA mutation carriers to ataxia also occurred before the estimated onset.[22] These data provide convergent evidence that the clinically determined ataxia onset precedes the self-

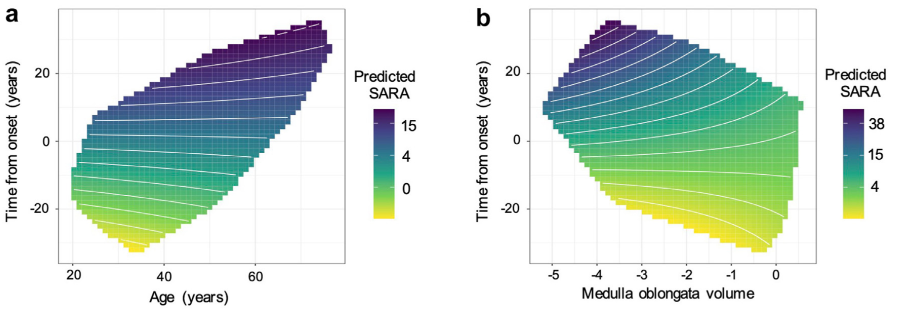

Fig. 2: Partial dependence plots of the multivariable model for SARA progression, including variables with p < 0.05 in univariable models. Predicted values of SARA as a function of the time from onset and age (a) and the time from onset and medulla oblongata volume given as z-score (b). In both panels, the value of the other predictor was set to the observed mean (medulla oblongata volume: −2.6; age: 46.4 years), respectively. The closer the white lines, which represent identical SARA values, are together, the faster is the predicted progression.

perceived onset, which is generally equated with the clinical onset. The number of observed transitions between stages was low. This reflects the relatively slow progression of SCA3. In a minority of cases, we observed counter-intuitive improvements over time which are most likely due to individual fluctuations of outcome measures. Indeed, video-based home recordings of SARA revealed short-term fluctuations of several score points.[23]

Mutant ATXN3 concentrations were almost constant across the entire disease course and did not show relevant dynamics. Correspondingly, ATXN3 provides no information about the progression of SCA3. This is in line with previous studies, where ATXN3 did not show a correlation with disease onset or severity.[4] However, ATXN3 has potential as a target engagement marker in gene silencing trials.[3,4] NfL levels became abnormal earlier than any of the analysed MRI measures. NfL slowly increased and stayed at elevated levels throughout the disease course. Like in previous studies,[9] it did not show a sensitivity to change in the ataxia stage. As NfL reflects the rate of neurodegeneration rather than disease severity, constantly increased NfL levels indicate ongoing disease progression. NfL might therefore be studied as a treatment response marker for SCA3.[5,8]

The earliest MRI abnormalities were volume loss of the medulla oblongata and reduced FA ICP, followed by volume loss of the pons and increased RD ICP, while cerebellar measures became abnormal only in the later course. The ICP contains the dorsal spinocerebellar tract and fibre tracts connecting the medulla oblongata with the cerebellum. Together with previous reports of impaired microstructural integrity of the ICP in preataxic SCA3 mutation carriers,[15,24] these findings suggest a pathological process that originates in the spinal cord and lower brainstem and further ascends to the cerebellum. They further indicate early white matter pathology in SCA3. This is in line with the observation of impaired oligodendrocyte maturation in two animal models of SCA3.[25,26]

To assess the responsiveness of SARA and the analysed biological markers, we determined the SCSs for each of them. This analysis revealed stage-dependence of SCSs. In both, biomarker and ataxia stage as well as across the entire disease course, pons volume had the highest SCS of all analysed measures. The superior responsiveness of the MRI volume measures compared to SARA is in line with previous studies in small cohorts of ataxic SCA3 individuals.[11,12] Our results agree with those of a prospective MRI study of 24 SCA3 mutation carriers over 6 months in that MRI measures were more sensitive to change than SARA and that pons volume had the highest responsiveness of the studied MRI measures.[14] The responsiveness of NfL was low across the entire disease course. This is in agreement with a previous longitudinal study in 19 SCA3 patients that did not find a NfL increase over two years.[9]

This study not only investigated the influence of biological factors, such as age, sex, and CAG repeat length, on disease progression in SCA3, but also that of fluid and MRI markers. Some, but not all previous studies in SCA3 reported an association between the length of the expanded CAG repeat and faster progression of ataxia severity.[27–30] In addition, greater CAG repeat length was reported to be a risk factor for the conversion of pre-ataxic SCA3 individuals to manifest ataxia.[22] In the univariable analysis of the present data, greater CAG repeat length and lower age were associated with faster SARA progression. In the multivariable analysis, lower age was one of two selected factors. As CAG repeat length and age of onset are inversely correlated in SCA3,[1] the opposing effects of CAG repeat length and age suggest a biological effect of the expansion size on the dynamics of disease progression. Of all biological markers investigated, only MRI volume measures were identified as predictors of progression. Among them, lower medulla oblongata volume had the most consistent effect.

A main limitation of this study is the small number of observed stage transitions. We were therefore not in the position to identify predictors of progression, as indicated by transition to more advanced disease stages. Another limitation is that the study was conducted mainly with European participants. It is thus unclear, whether the results can be generalised to SCA3 mutation carriers from other world regions.

In conclusion, our study provides quantitative information on the progression of biological markers in SCA3 mutation carriers before and after onset of ataxia, and allowed the identification of predictors for clinical progression. Our data are useful for the design of future clinical trials. Of particular importance is the finding that pons volume was more sensitive to change than any other outcome. This characterises pons volume as a useful marker to monitor progression in clinical trials.

Contributors

Conceptualisation: JF, TK, MB. *Data curation, formal analysis*: JF, MB, MF, HGM, JHS, TS, PW, TE, KT, MSch. *Methodology, Resources, validation and visualisation*: MB, JF, MF, HGM, PG, JHS. *Writing—original draft*: JF, TK, MB, MF, HGM, JHS, TS. *Investigation*: JF, TK, ML, LPdA, PG, BvdW, JdV, JI, GO, OR, LS, KR, DT, JS, CO, HJ, MMS, JHS, JvG, THvP, CGR, SK, AH, HZ, MR, AFF, JV, ALP, LMq, ID, JMJo, KB, MPov, EMR, MSy. *Project administration*: TK, JF, ML, LPdA, PG, BvdW, JdV, JI, GO, OR, LS, KR, DT, JS, CO, HJ, MMS, JHS. *Writing—review & editing*: ML, LPdA, PG, BvdW, JdV, JI, GO, OR, LS, KR, DT, JS, CO, HJ, MMS, PW, TE, KT, MSch, JvG, THvP, CGR, SK, AH, HZ, MR, AFF, JV, ALP, LMq, ID, JMJo, KB, MPov, EMR, MSy. *Funding acquisition*: TK, JF, GO, BvdW, OR, LS, ML, LPdA, PG.

JF, TK, MB, MF, JHS, HGM verified the data and had access to the raw data. JF, TK, MB, PG, MF, JHS and HGM had the final responsibility for the decision to submit for publication.

Data sharing statement

The data are not publicly available but can be accessed upon reasonable request to the consortium, subject to approval.

Declaration of interests

JF received consultancy honoraria from Vico therapeutics, unrelated to the present manuscript. GO has consulted for IXICO Technologies Limited, Servier and UCB Biopharma SRL/Lacerta Therapeutics Inc, serves on the Scientific Advisory Board of BrainSpec Inc. and received research support from Biogen, each unrelated to the current manuscript. JS is site PI for Biohaven Pharmaceuticals clinical trials NCT03701399 and NCT02960893; received consults for Biohaven Pharmaceuticals; and royalties from Oxford University Press, Elsevier, MacKeith Press, and Springer; and is the inventor of the Brief Ataxia Rating Scale, Cerebellar Cognitive Affective/Schmahmann Syndrome Scale, the Patient Reported Outcome Measure of Ataxia, and the Cerebellar Neuropsychiatry Rating Scale which are licenced to the General Hospital Corporation; all unrelated to the current manuscript. MGE received consultancy honoraria from Biogen and Healthcare Manufaktur Germany, both unrelated to the present manuscript. HZ has served at scientific advisory boards and/or as a consultant for Abbvie, Acumen, Alector, Alzinova, ALZpath, Amylyx, Annexon, Apellis, Artery Therapeutics, AZTherapies, Cognito Therapeutics, CogRx, Denali, Eisai, Enigma, LabCorp, Merck Sharp & Dohme, Merry Life, Nervgen, Novo Nordisk, Optoceutics, Passage Bio, Pinteon Therapeutics, Prothena, Quanterix, Red Abbey Labs, reMYND, Roche, Samumed, ScandiBio Therapeutics AB, Siemens Healthineers, Triplet Therapeutics, and Wave. HZ is chair of the Alzheimer's Association Global Biomarker Standardization Consortium and chair of the IFCC WG-BND. HZ is a co-founder of Brain Biomarker Solutions in Gothenburg AB (BBS), which is a part of the GU Ventures Incubator Program, and a shareholder of MicThera (outside submitted work). PG has received grants and honoraria for advisory board from Vico Therapeutics, honoraria for advisory board from Triplet Therapeutics, grants and personal fees from Reata Pharmaceutical, grants from Wave. LS has received consultancy honoraria from Vico, Alexion and Novartis, unrelated to the present manuscript. MSy has received consultancy honoraria from Ionis, UCB, Prevail, Orphazyme, Biogen, Servier, Reata, GenOrph, AviadoBio, Biohaven, Zevra, Lilly, Quince, and Solaxa, all unrelated to the present manuscript. TK received consultancy honoraria from Arrowhead, Bristol Myers Squibb and UCB, unrelated to the present manuscript. KR received consultancy honoraria from Roche and Lilly unrelated to the present manuscript. BvdW would like to thank Heidi van den Boogaard and Janneke Rigter-Schimmel for their help in the ESMI logistics and assessments. JAR received honoraria for participation in advisory boards and speaking fees for Roche, Novartis Gene therapy and Biogen, all in the field of paediatric neuromuscular disorders. IC has received honoraria for participation in advisory boards and speaking fees for Bial, in the field of Epilepsy. AT holds stocks of Viatris Inc. is a pharmaceutical company. EMR received consulting fees from Aletheia and is part of the advisory board of Brain Spec without financial support. We would like to thank Anne Boehlen for her support in the administration of ESMI.

Acknowledgements

Several authors of this publication are members of the European Reference Network for Rare Neurological Diseases. JF was funded within the Advanced Clinician Scientist Programme (ACCENT, funding code 01EO2107, by the German Federal Ministry of Education and Research (BMBF) and as a PI of the iBehave Network, sponsored by the Ministry of Culture and Science of the State of North Rhine-Westphalia. LPdA as funded by the European Regional Development Fund (ERDF), through the Centro 2020 Regional Operational Program; through the COMPETE 2020–Operational Programme for Competitiveness and Internationalisation, and Portuguese national funds via FCT—Fundação para a Ciência e a Tecnologia, under the projects: UIDB/04539/2020, UIDP/04539/2020, LA/P/0058/2020, ViraVector (CENTRO-01-0145-FEDER-022095), Neurodiet (JPND/0001/2022) and 2022.06118.PTDC, CinTech under PRR Ref 02/C05-i01.01/2022.PC644865576-00000005, ARDAT under the IMI2 JU Grant agreement No 945473 supported by EU and EFPIA; ERDERA ID:101156595, Capacity 2023 ID: 101145599, GeneT-Gene Therapy Centre of Excellence Portugal Teaming Project ID:101059981, GeneH Excellence Hub ID:101186939, GCure Era-Chair ID: 101186929, supported by the European Union's Horizon Europe program. Servier for the ESMI project. LPdA reveiced honoraria for a lecture from Novartis Gene Therapy. MMS was received funding related to the SCA Young Investigator Award 2019 from the National Ataxia Foundation (NAF), via the employment contract as a Junior Investigator at the Centre for Neuroscience and Cell Biology under the Portuguese Law DL57/2026 and via the employment contract as assistant investigator under the CEEC individual FCT program 2023.06020.CEECIND/CP2832/CT0010. MGE received research support from the German Ministry of Education and Research (BMBF) within the European Joint Program for Rare Diseases (EJP-RD) 2021 Transnational Call for Rare Disease Research Projects (funding number 01GM2110), from the National Ataxia Foundation (NAF), and from Ataxia UK, all unrelated to the present manuscript. MR is supported by Fundação para a Ciência e a Tecnologia (FCT; CEECIND/03018/2018/CP1556/CT0009). In the Netherlands, this work was supported by ZonMw (grant number 733051066). The Centre for Magnetic Resonance Research is supported by the National Institute of Biomedical Imaging and Bioengineering (NIBIB) grant P41 EB027061, the Institutional Center Cores for Advanced Neuroimaging award P30 NS076408 and S10 OD017974 grant. JS was supported in part by the National Ataxia, Great Oaks, Once Upon A Time, and MINDlink Foundations. PS was funded by FCT under the grant SFRH/BD/148451/2019. DT received funding from the DFG, EU and Bernd Fink Foundation unrelated to the study and grants and institutional moneya to cover travel expenses to go the national and international meetings. FE received funding from the DFG in the framework of the DFG Clinician Scientist Programme UMEA, FU 356/12-2. HZ is a Wallenberg Scholar and a Distinguished Professor at the Swedish Research Council supported by grants from the Swedish Research Council (#2023-00356, #2022-01018 and #2019-02397), the European Union's Horizon Europe research and innovation programme under grant agreement No 101053962, Swedish State Support for Clinical Research (#ALFGBG-71320), the Alzheimer's Drug Discovery Foundation (ADDF), USA (#201809-2016862), the AD Strategic Fund and the Alzheimer's Association (#ADSF-21-831376-C, #ADSF-21-831381-C, #ADSF-21-831377-C, and #ADSF-24-1284328-C), the European Partnership on Metrology, co-financed from the European Union's Horizon Europe Research and Innovation Programme and by the Participating States (NEuroBioStand, #22HLT07), the Bluefield Project, Cure Alzheimer's Fund, the Olav Thon Foundation, the Erling-Persson Family Foundation, Familjen Rönströms Stiftelse, Familjen Beiglers Stiftelse, Stiftelsen för Gamla Tjänarinnor, Hjärnfonden, Sweden (#FO2022-0270), the European Union's Horizon 2020 research and innovation programme under the Marie Skłodowska-Curie grant agreement No 860197 (MIRIADE), the European Union Joint Programme – Neurodegenerative Disease Research (JPND2021-00694), the National Institute for Health and Care Research University College London Hospitals Biomedical Research Centre, the UK Dementia Research Institute at UCL (UKDRI-1003), and an anonymous donor. PG is supported by the National Institute for Health Research University College London Hospitals Biomedical Research Centre UCLH. PG receives also support from the North Thames CRN. HGM received a travel grant of Ataxia UK to attnd international a ataxia meeting. PG and HGM, work at University College London Hospitals/University College London, which receives a proportion of funding from the Department of Health's National Institute for Health Research Biomedical Research Centre's funding scheme. PG received funding from CureSCA3 in support of HGM work. LS received funding by the Deutsche Forschungsgemeinschaft (DFG, grants SCHO754/6-2 and SCA754/8-1), the German Ministry of Education and Research (BMBF, grants 01GM2209F and 01GM2210A) and the German Ministry of Health (BMG, grant ZMVI1-2520DAT94E) and the European Union (grant 947588), all unrelated to this project. MSy is supported by the European Union, project European Rare Disease Research Alliance (ERDERA), GA n°101156595, funded under call HORIZON-HLTH-2023-DISEASE-07. AT held a clinician scientist position that was supported by the DFG in the framework of the DFG Clinician Scientist Programme UMEA (FU 356/12-1 and 12-2), a travel scholarship for attending the Society of Neuroscience annual meeting in Washington D.C. in 11/2023 from the DAAD (German Academic Exchange Service). At the US sites this work was in part supported by the National Ataxia Foundation and the National Institute of Neurological Disorders and Stroke (NINDS) grant R01NS080816. The Centre for Magnetic Resonance Research is supported by the National Institute of Biomedical Imaging and Bioengineering (NIBIB) grant P41 EB027061, the Institutional Center Cores for Advanced Neuroimaging award P30 NS076408 and S10 OD017974 grant. The institution of EMR received funding from the grant no. NIHR01 DA047088, NIH R01NS124065, Baszucki Group Fundation (2023-005), and EMR for the attending meetings via no. NIHR01 DA047088, NIH R01NS124065.

Appendix A. Supplementary data

Supplementary data related to this article can be found at https://doi.org/10.1016/j.lanepe.2025.101339.

References

1 Paulson H. Machado-Joseph disease/spinocerebellar ataxia type 3. *Handb Clin Neurol*. 2012;103:437–449.

2 Klockgether T, Ashizawa T, Brais B, et al. Paving the way toward meaningful trials in ataxias: an ataxia global initiative perspective. *Mov Disord*. 2022;37:1125–1130. https://doi.org/10.1002/mds.29032.

3 Hübener-Schmid J, Kuhlbrodt K, Peladan J, et al. Polyglutamine-expanded ataxin-3: a target engagement marker for spinocerebellar ataxia type 3 in peripheral blood. *Mov Disord*. 2021;36:2675–2681. https://doi.org/10.1002/mds.28749.

4 Prudencio M, Garcia-Moreno H, Jansen-West KR, et al. Toward allele-specific targeting therapy and pharmacodynamic marker for spinocerebellar ataxia type 3. *Sci Transl Med*. 2020;12. https://doi.org/10.1126/scitranslmed.abb7086.

5 Gaetani L, Blennow K, Calabresi P, Di Filippo M, Parnetti L, Zetterberg H. Neurofilament light chain as a biomarker in neurological disorders. *J Neurol Neurosurg Psychiatry*. 2019;90:870–881. https://doi.org/10.1136/jnnp-2018-320106.

6 Du Tezenas Montcel S, Petit E, Olubajo T, et al. Baseline clinical and blood biomarkers in patients with preataxic and early-stage disease spinocerebellar ataxia 1 and 3. *Neurology*. 2023;100:e1836–e1848. https://doi.org/10.1212/WNL.0000000000207088.

7 Garcia-Moreno H, Prudencio M, Thomas-Black G, et al. Tau and neurofilament light-chain as fluid biomarkers in spinocerebellar ataxia type 3. *Eur J Neurol*. 2022;29:2439–2452. https://doi.org/10.1111/ene.15373.

8 Wilke C, Haas E, Reetz K, et al. Neurofilaments in spinocerebellar ataxia type 3: blood biomarkers at the preataxic and ataxic stage in humans and mice. *EMBO Mol Med*. 2020;12:e11803. https://doi.org/10.15252/emmm.201911803.

9 Coarelli G, Darios F, Petit E, et al. Plasma neurofilament light chain predicts cerebellar atrophy and clinical progression in spinocerebellar ataxia. *Neurobiol Dis*. 2021;153:105311. https://doi.org/10.1016/j.nbd.2021.105311.

10 Li Q-F, Dong Y, Yang L, et al. Neurofilament light chain is a promising serum biomarker in spinocerebellar ataxia type 3. *Mol Neurodegener*. 2019;14:39. https://doi.org/10.1186/s13024-019-0338-0.

11 Adanyeguh IM, Perlbarg V, Henry PG, et al. Autosomal dominant cerebellar ataxias: imaging biomarkers with high effect sizes. *Neuroimage Clin*. 2018;19:858–867.

12 Reetz K, Costa AS, Mirzazade S, et al. Genotype-specific patterns of atrophy progression are more sensitive than clinical decline in SCA1, SCA3 and SCA6. *Brain*. 2013;136:905–917.

13 Piccinin CC, Rezende TJR, de Paiva JLR, et al. A 5-year longitudinal clinical and magnetic resonance imaging study in spinocerebellar ataxia type 3. *Mov Disord*. 2020;35:1679–1684. https://doi.org/10.1002/mds.28113.

14 Rezende TJR, Petit E, Park YW, et al. Sensitivity of advanced magnetic resonance imaging to progression over six months in early spinocerebellar ataxia. *Mov Disord*. 2024;39(10):1856–1867. https://doi.org/10.1002/mds.29934.

15 de Oliveira CM, Leotti VB, Polita S, et al. The longitudinal progression of MRI changes in pre-ataxic carriers of SCA3/MJD. *J Neurol*. 2023;270:4276–4287. https://doi.org/10.1007/s00415-023-11763-6.

16 Faber J, Berger M, Wilke C, et al. Stage-dependent biomarker changes in spinocerebellar ataxia type 3. *Ann Neurol*. 2024;95:400–406. https://doi.org/10.1002/ana.26824.

17 Schmitz-Hubsch T, Du Montcel ST, Baliko L, et al. Scale for the assessment and rating of ataxia: development of a new clinical scale. *Neurology*. 2006;66:1717–1720.

18 Jacobi H, Reetz K, Du Montcel ST, et al. Biological and clinical characteristics of individuals at risk for spinocerebellar ataxia types 1, 2, 3, and 6 in the longitudinal RISCA study: analysis of baseline data. *Lancet Neurol*. 2013;12:650–658.

19 Klockgether T, Lüdtke R, Kramer B, et al. The natural history of degenerative ataxia: a retrospective study in 466 patients. *Brain*. 1998;121:589–600.

20 Tezenas du MS, Durr A, Rakowicz M, et al. Prediction of the age at onset in spinocerebellar ataxia type 1, 2, 3 and 6. *J Med Genet*. 2014;51:479–486.

21 Krismer F, Seppi K, Jönsson L, et al. Sensitivity to change and patient-centricity of the unified multiple system atrophy rating scale items: a data-driven analysis. *Mov Disord*. 2022;37:1425–1431. https://doi.org/10.1002/mds.28993.

22 Jacobi H, Du Montcel ST, Romanzetti S, et al. Conversion of individuals at risk for spinocerebellar ataxia types 1, 2, 3, and 6 to manifest ataxia (RISCA): a longitudinal cohort study. *Lancet Neurol*. 2020;19:738–747.

23 Grobe-Einsler M, Taheri AA, Faber J, et al. Development of SARA(home), a new video-based tool for the assessment of ataxia at home. *Mov Disord*. 2021;36(5):1242–1246.

24 Chandrasekaran J, Petit E, Park YW, et al. Clinically meaningful magnetic resonance endpoints sensitive to preataxic spinocerebellar ataxia types 1 and 3. *Ann Neurol*. 2023;93:686–701. https://doi.org/10.1002/ana.26573.

25 Haas E, Incebacak RD, Hentrich T, et al. A novel SCA3 knock-in mouse model mimics the human SCA3 disease phenotype including neuropathological, behavioral, and transcriptional abnormalities especially in oligodendrocytes. *Mol Neurobiol*. 2022;59:495–522. https://doi.org/10.1007/s12035-021-02610-8.

26 Schuster KH, Zalon AJ, Zhang H, et al. Impaired oligodendrocyte maturation is an early feature in SCA3 disease pathogenesis. *J Neurosci*. 2022;42:1604–1617. https://doi.org/10.1523/JNEUROSCI.1954-20.2021.

27 Jardim LB, Hauser L, Kieling C, et al. Progression rate of neurological deficits in a 10-year cohort of SCA3 patients. *Cerebellum*. 2010;9:419–428.

28 Jacobi H, Du Montcel ST, Bauer P, et al. Long-term disease progression in spinocerebellar ataxia types 1, 2, 3, and 6: a longitudinal cohort study. *Lancet Neurol*. 2015;14:1101–1108.

29 Lin Y-C, Lee Y-C, Hsu T-Y, Liao Y-C, Soong B-W. Comparable progression of spinocerebellar ataxias between Caucasians and Chinese. *Parkinsonism Relat Disorders*. 2019;62:156–162. https://doi.org/10.1016/j.parkreldis.2018.12.023.

30 Peng L, Peng Y, Chen Z, et al. The progression rate of spinocerebellar ataxia type 3 varies with disease stage. *J Transl Med*. 2022;20:226. https://doi.org/10.1186/s12967-022-03428-1.

3.3 Publication 3: Myelin water fraction mapping with joint inversion of gradient-echo and spin-echo data (DOI: 10.1007/s10334-025-01235-5)

Magnetic Resonance Materials in Physics, Biology and Medicine (2025) 38:317–332
https://doi.org/10.1007/s10334-025-01235-5

RESEARCH ARTICLE

Myelin water fraction mapping with joint inversion of gradient-echo and spin-echo data

Ségolène Dega[1] · **Mónica Ferreira**[2,3] · **Marten Veldmann**[2] · **Rüdiger Stirnberg**[2] · **Hendrik Paasche**[1] · **Tony Stöcker**[2,4]

Received: 26 July 2024 / Revised: 22 January 2025 / Accepted: 4 February 2025 / Published online: 7 March 2025

Abstract

Objective Accurate estimation of brain myelin-water content from multi-echo data is challenging due to the inherent ill-posedness of the inversion problem. In this study, we propose a novel method for myelin-water imaging that jointly utilizes gradient-echo and spin-echo imaging data to enhance the accuracy of myelin-water estimation.
Material and methods Multi-echo gradient-echo and spin-echo data were simulated and acquired in vivo. The simulations are based on a parameterized myelin and free water signal model, which is also used for the inversion by means of nonlinear local-search optimization. Single inversions of the individual datasets as well as joint inversion of the combined datasets were performed on simulated and real data. While single inversions estimate either the T_2 or T_2^* relaxation spectrum, the joint inversion estimates both spectra simultaneously.
Results Simulation results show that the accuracy of myelin-water imaging improves when jointly inverting gradient-echo and spin-echo synthetic data. In vivo experiments show that the joint inversion of both datasets leads to sharper and more distinct myelin-water images as compared to the individual inversions.
Discussion Our method addresses the ill-posed nature of the myelin-water inversion problem by leveraging complementary information from multi-echo gradient-echo and multi-echo spin-echo imaging sequences, thus improving the reliability of myelin-water quantification.

Keywords Myelin water imaging · Myelin water fraction · T_2 and T_2^* relaxation spectra · Joint inversion

Introduction

Myelin, a lipid-rich substance surrounding neuronal axons, plays a critical role in facilitating rapid signal transmission in the central nervous system. Alterations in myelin content are implicated in various neurologic disorders, making accurate myelin measurements essential for both research and clinical applications. MRI can indirectly assess myelin content by estimating the amount of myelin water (MW), i.e., the amount of water trapped in the myelin sheath [1]. Myelin water has an influence on multiple MRI contrasts, and meanwhile several myelin-water imaging (MWI) methods exist which are either based on T_1, T_2, T_2^*, or MT (magnetization transfer) contrast [2, 3]. For instance, MW has shorter transverse relaxation times than the surrounding axonal and extra-cellular water (AEW). Originally, T_2 and T_2^* contrasts were used to estimate the myelin-water fraction (MWF = amount of MW divided by the total amount of water) from the peak areas of transverse relaxation spectra [4, 5]. Here, either multi-echo spin-echo (ME-SE) or multi-echo gradient-echo (ME-GE) experiments can be employed to measure the multi-exponential T_2 or T_2^* decay signals, respectively. Afterward the relaxation spectra are obtained from data fitting with a suitable signal model. However, this process often suffers from limited accuracy and precision, primarily due to the ill-posed nature of the inversion problem. The MR signal from a single imaging voxel is the superposition of many decay signals with different relaxation times (MW and AEW). In case of a simple multi-exponential decay signal model, estimating those components from their

---

✉ Tony Stöcker
tony.stoecker@dzne.de

[1] UFZ - Helmholtz Centre for Environmental Research (UFZ), Leipzig, Germany

[2] German Center for Neurodegenerative Diseases (DZNE), Bonn, Germany

[3] University of Bonn, Bonn, Germany

[4] Department of Physics and Astronomy, University of Bonn, Bonn, Germany

sum is mathematically equivalent to the inverse Laplace transform [2]. Since exponential functions are mathematically not orthogonal, this is a highly ill-posed inversion problem and the fitting is very sensitive to noise [3]. In order to get stable fit results regularization is typically required. Adding a regularization term to the objective function improves the conditioning of the minimization problem, thus enabling a direct numerical solution. Commonly Tikhonov regularization is employed, which typically results in smooth relaxation spectra with minimum energy (L_2-norm). Regularization enforces a numerical stable solution, however, it also biases the MWF estimates [3]. In addition to the ill-posed nature of the inversion problem, MWF estimation is often further confounded by an underdetermined system of equations: multi-echo signal data are acquired at N different echo times (TE) from which a relaxation spectrum with $M > N$ support points shall be estimated [2]. From the infinite number of possible solutions, the inversion chooses the one which minimizes the objective function (including regularization for stabilization). Commonly, this minimization problem is solved with the nonnegative least squares (NNLS) approach, where no assumption is made on the shape of the relaxation spectrum. The approach is fast, easy to apply and has the additional advantage that the result does not depend on a starting model (in contrast to parameterized local-search optimization), which may explain its popularity in MW imaging. However, it has the disadvantage that a large number of unknowns—the entire relaxation distribution has to be fitted, hence resulting in the above-mentioned underdetermination. Alternatively, it has been shown that fitting a parameterized relaxation spectrum vastly reduces the number of unknowns and improves fitting stability in case of low SNR ME-SE data. Raj et al. modeled the T_2 relaxation distribution as a sum of Gaussian functions representing the different compartments [6]. Then, the inversion problem was solved with an iterative nonlinear least-squares optimization approach. The approach was also applied to ME-GE data with Dirac function (“Delta-peaks”) [7], where additionally the complex signal was utilized. The ME-GE signal depends on susceptibility-induced frequency shifts due to white matter fiber orientation [8]. Therefore, using additional phase information improves MWF estimates based on ME-GE data [3].

Nevertheless, in all these cases, the ill-posed nature of the inversion problem and the concomitant fitting instabilities remain, typically requiring strong regularization. However, ME-GE and ME-SE provide *MWF* estimates via partially independent tissue properties: while the ME-SE signal solely depends on proton density, T_1 and T_2, the ME-GE signal in addition depends on $T_2' = \left(1/T_2^* - 1/T_2\right)^{-1}$ and the above-mentioned frequency shifts. Similar situations are often met in geophysics, where (partially) independent measures provide estimates of physical parameters, each resulting from a highly ill-posed inversion problem. In order to improve the accuracy and precision of the parameter estimates, joint inversion is a geophysical approach on simultaneously inverting multiple data sets influenced by common subsurface physical parameters [9–11]. In this study, we propose such a joint inversion approach to MWI that capitalizes on the complementary information provided by ME-GE and ME-SE imaging sequences. By jointly inverting data from both sequences using parameterized T_2 and T_2^* relaxation spectra, our method aims to mitigate the ill-posedness of the individual inversion problems and enhance the reliability of MW estimation. We hypothesize that the combination of ME-GE and ME-SE data can provide complementary information sensitive to related but different tissue properties (T_2 and T_2^*), thus improving the robustness and accuracy of MW quantification. Potentially, this can be used to relax regularization. Through simulations and in vivo experiments we demonstrate the efficacy of the proposed method in improving MWI.

Theory

ME-GE and ME-SE signal decay models

Under the assumption that T_2 and T_2^* are constant within the acquisition time window (e.g., not influenced by exchange processes), the MR signals of ME-GE and ME-SE sequences can be expressed as integrals [3]

$$S_{GE}(t) = \int_0^\infty \Omega_{GE}\left(T_2^*\right) \exp\left[-t/T_2^*\right] dT_2^* \tag{1}$$

$$S_{SE}(t) = \int_0^\infty \Omega_{SE}\left(T_2\right) S_{EPG}\left(t;\alpha_r, T_1, T_2\right) \mathrm{d}T_2 \tag{2}$$

where Ω_{SE} and Ω_{GE} denote the T_2 and T_2^* relaxation spectra (or distributions) of an imaging voxel. The first equation assumes that the effective transverse relaxation is governed by a simple multi-exponential decay. Thus, the composite ME-GE signal is the forward Laplace transform of the T_2^* distribution. In case of perfect 180° refocusing, the ME-SE signal would follow the same signal model with T_2 instead of T_2^*. However, it is typically not possible to obtain perfect refocusing pulses in real experiments due to subject-induced transmit field inhomogeneities. Therefore, it is necessary to account for signal deviations originating from stimulated echoes generated in the CPMG echo train [12]. These signal components can be conveniently modeled with the extended phase graph (EPG) algorithm [13, 14]. Accordingly, $S_{EPG}\left(t;\alpha_r, T_1, T_2\right)$ in Eq. (2) denotes the ME-SE signal at the echo time t computed with the EPG formalism. It depends on the refocusing flip angle, α_r, and the relaxation times T_1 and T_2. However, the T_1 dependence is weak in case of brain tissue with $T_1 \gg T_2$, and it is sufficient to approximate $T_1 \approx 1$ s with minimal effect on the signal amplitude (and, therefore, subsequent MWF estimation) [15].

Discretization of the integrals in Eqs. (1) and (2) for a finite number of echo times and a grid of relaxation times, T_2 and T_2^*, leads to linear equations

$$S_{GE}\left(t_{GE}\right) = A_{GE}\left(t_{GE}, T_2^*\right) \cdot \Omega_{GE}\left(T_2^*\right) \tag{3}$$

$$S_{SE}\left(t_{SE}\right) = A_{SE}\left(t_{SE}, T_2\right) \cdot \Omega_{SE}\left(T_2\right) \tag{4}$$

where A_{GE} and A_{SE} are operator matrices solving the respective forward problems, S_{GE} and S_{SE} are signal vectors at respective echo times t_{GE} and t_{SE}, and Ω_{GE} and Ω_{SE} are the relaxation spectra vectors on a suitable grid of relaxation times, T_2 and T_2^*, respectively. The forward operators, A_{GE} and A_{SE}, can be precomputed for efficiently solving the nonlinear inverse problem.

Myelin-induced frequency shift: extension to a complex ME-GE signal model

The ME-GE exponential signal model of Eq. (1) does not account for compartmental frequency shifts within the imaging voxel. It was previously shown that susceptibility-induced frequency shifts give rise to a non-exponential ME-GE signal [16], resulting in biased MWF estimates from ME-GE magnitude data. Therefore, we extend the ME-GE signal model to account for frequency shifts, $\Delta\omega$, in the MW and AEW compartments. Following the approach from Nam et al. [7], we extend Eq. (3) to a complex signal model by introducing a complex forward operator

$$A_{GE}\left(t, T_2^*, \Delta\omega, \Delta\Phi_0\right) = \exp\left[-t/T_2^*\right]\exp\left[-\mathrm{i}\left(\Delta\omega t + \Delta\Phi_0\right)\right] \tag{5}$$

where $\Delta\Phi_0$ is a spatially dependent constant phase offset. In the following parameterized forward model, we assume constant frequency shifts, $\Delta\omega_1$ and $\Delta\omega_2$, for the MW and AEW compartments, respectively [7, 16].

Inversion of bi-Gaussian parametric models

We first present the method for the single inversion, i.e., the method to recover the MWF from T_2 (respectively T_2^*) data only, before describing the joint inversion. To model the T_2 (respectively T_2^*) distribution, we resort to a parametric model, assuming the presence of two compartments with different T_2 values, one for the MW pool (fast compartment) and one for axonal/extra-cellular water pool (slow compartment). Similar to [6], we propose a bi-Gaussian parametric model, which strongly improves the optimization stability compared to a bi-impulse (delta function) model.

Within this assumption, the T_2 distribution is modeled by six parameters: the T_2 means (μ_1, μ_2) and standard deviations (σ_1, σ_2) of both compartments, the integral of the axonal/extra-cellular compartment (I_2), and finally the MWF, which is the ratio of the integral of the myelin compartment over the sum of the two compartment integrals, $I_1/\left(I_1 + I_2\right)$. Most references in the literature, using either T_2 or T_2^* parametric models, first invert for all compartment integrals (or amplitudes if delta functions are used instead of Gaussian functions) and based on that compute MWF [2, 7, 17]. Instead, we used the MWF directly as one of the model parameters for the inversion. We found that this parametrization leads to a slightly better resolution and spatial continuity on the final 2D MWF map than inverting for both compartment integrals separately.

Let $G(\tau|\mu, \sigma, I)$ be a Gaussian function over the variable τ, defined by its mean value μ, standard deviation σ and integral value I. Denoting $x = \left(\mu_1, \sigma_1, MWF, \mu_2, \sigma_2, I_2\right)$ as the model vector i.e., the six parameters describing the two Gaussian functions, the T_2 distribution is given by

$$\Omega_{SE}\left(T_2|x\right) = G\left(T_2|\mu_1, \sigma_1, I_1\right) + G\left(T_2|\mu_2, \sigma_2, I_2\right) \tag{6}$$

where I_1 and I_2 are the integrals of the MW pool and the axonal/extra-cellular water pool (AEW), respectively. I_1 is not treated as a model parameter, but expressed according to the MWF definition as $I_1 = I_2 MWF/(1 - MWF)$. Let $S_{SE}(t)$ be the observed ME-SE signal with t being the echo times vector. For a single inversion, the unregularized minimization problem is then given by

$$\min_x \left\| S_{SE}(t) - \hat{S}_{SE}(t|x)^2 \right\|$$

where $\hat{S}_{SE}(t|x) = A_{SE}\left(t, T_2\right) \cdot \Omega_{SE}\left(T_2|x\right)$ is the parameterized forward model from the T_2 relaxometry distribution to the data space (ME-SE decay curve).

Since the problem is highly ill-posed, regularization has to be added to stabilize the inversion. However, classical Tikhonov regularization aims to minimize the model parameters and, therefore, results in low and unrealistic values for the myelin and axonal/extra-cellular T_2 values (μ_1 and μ_2). To overcome this problem, we added a constraint on the model to stay as close as possible to the initial model, but weighting this constraint mainly on the mean of the parameters. The regularized minimization problem is given by

$$\min_x \left\| S_{SE}(t) - \hat{S}_{SE}(t|x) \right\|^2 + \left\| \lambda \cdot \left(x - x_{in}\right) \right\|^2 \tag{7}$$

where x_{in} is the initial model vector (cf. Table 1) and λ a model-sized regularization vector. We resort to this regularization for

Table 1 Summary of the model parameters with their initial values (i.v.) and upper and lower bound, respectively

#	Parameter	Description	Unit	i.v	Bounds	Regularization
1	μ_{1,T_2}	T_2 mean of the MW distribution	[ms]	18	[5, 35]	$\lambda^{S/J}_{1/1}$=0.02
2	σ_{1,T_2}	T_2 standard deviation of the MW distribution	[ms]	0.1	[0.1, 5]	$\lambda^{S/J}_{2/2}$=0.01
3	μ_{2,T_2}	T_2 mean of the AEW distribution	[ms]	80	[45, 180]	$\lambda^{S/J}_{3/3}$=0.02
4	σ_{2,T_2}	T_2 standard deviation of the AEW distribution	[ms]	0.1	[0.1, 5]	$\lambda^{S/J}_{4/4}$=0.01
5	I_{2,T_2}	Integral of the T_2 AEW distribution	–(normalized)	2	[0.1, 5]	$\lambda^{S/J}_{5/5}$=0.01
6	MWF	Myelin-water fraction	–(normalized)	0.1	[0, 0.85]	$\lambda^{S/G/J}_{6/6/6}$=0.01
7	μ_{1,T_2^*}	T_2^* mean of the MW distribution	[ms]	10	[5, 25]	$\lambda^{G/J}_{1/7}$=0.02
8	σ_{1,T_2^*}	T_2^* standard deviation of the MW distribution	[ms]	0.1	[0.1, 5]	$\lambda^{G/J}_{2/8}$=0.01
9	$\Delta\omega_1$	Frequency shift of the MW component	[Hz]	−5	[−75, 75]	$\lambda^{G/J}_{3/9}$=0.02
10	μ_{2,T_2^*}	T_2^* mean of the AEW distribution	[ms]	60	[55, 180]	$\lambda^{G/J}_{4/10}$=0.02
11	σ_{2,T_2^*}	T_2^* standard deviation of the AEW distribution	[ms]	0.1	[0.1, 5]	$\lambda^{G/J}_{5/11}$=0.01
12	I_{2,T_2^*}	Integral of the T_2^* AEW distribution	– (normalized)	1	[0.1, 5]	$\lambda^{G/J}_{7/12}$=0.01
13	$\Delta\omega_2$	Frequency shift of the AEW component	[Hz]	0	[−75, 75]	$\lambda^{G/J}_{8/13}$=0.01
14	Φ_0	Constant phase offset	[rad]	0	[0, 2 π]	$\lambda^{G/J}_{9/14}$=0.01

The rows 1–6 (until MWF) denote parameters for single ME-SE inversion, and the rows 7–14 for single ME-GE inversion, while joint inversion uses all parameters. The last column provides the λ regularization vectors used in the simulations. The superscripts λ^S, λ^G, and λ^J denote vectors for single ME-SE inversion, single ME-GE inversion, and joint inversion, respectively. The subscripts give the number of the element in the corresponding regularization vector, and the values correspond the regularization used for the in vivo data, while the simulations used λ = 0.01 for all parameters

the fast and slow compartments mean values (μ_1,μ_2) since we do have prior information on these parameters from the literature, and want to use this knowledge as initial values to better constraint the inversion. Regarding the standard deviations, which are initialized with small values (see Tab. 1), this regularization helps to maintain the values as small as possible, since we would expect delta functions in an ideal noise-free world. Finally, since we do not have knowledge on the MWF and slow compartment integral (MWF and I_2), we set the corresponding elements of λ for these two parameters to negligibly small, non-zero values (see Tab. 1).

Accordingly, the above equations also apply for the inversion of magnitude ME-GE data, where the model vector x contains the respective six parameters of the T_2^* distribution. Incorporating the complex signal model from Eq. (5), the previous equation naturally extend for the inversion of complex ME-GE data:

$$\min_x \left\| S_{GE}(t) - \hat{S}_{GE}(t|x) \right\|^2 + \left\| \lambda \cdot \left(x - x_{in} \right) \right\|^2 \tag{8}$$

with the parameterized complex signal forward model

$$\widehat{S}_{GE}(t|x) = \left[G\left(T_2^* | \mu_1, \sigma_1, \frac{I_2\, MWF}{1 - MWF} \right) \mathrm{e}^{-t/T_2^* + \mathrm{i}\Delta\omega_1 t} + G\left(T_2^* | \mu_2, \sigma_2, I_2 \right) \mathrm{e}^{-t/T_2^* + \mathrm{i}\Delta\omega_2 t} \right] \mathrm{e}^{\mathrm{i}\Phi_0} \tag{9}$$

where the model vector $x = \left(\mu_1, \sigma_1, \Delta\omega_1, MWF, \mu_2, \sigma_2, I_2, \Delta\omega_2, \Delta\Phi_0 \right)$ now contains nine values for the parameterization, including the MW and AEW frequency shifts, $\Delta\omega_1$ and $\Delta\omega_2$, and the constant phase term $\Delta\Phi_0$.

In contrast to the single inversions, the joint inversion aims to find simultaneously distributions for both T_2 and T_2^* which fit the respective decay curves, with the same MWF value in both distributions. The model vector x has now 14 parameters since it represents two signals, the SE signal modeled by six parameters and the GE signal modeled by nine parameters, but the MWF parameter is the same in both. Then, the minimization problem of the joint inversion can be stated as the sum of both residuals with a regularization term (analog to the single inversions) using 14 parameters:

$$\min_{x} \; \alpha \left\| S_{SE}\left(t_{SE}\right) - \hat{S}_{SE}(t|x) \right\|^2 + \left\| S_{GE}\left(t_{GE}\right) - \hat{S}_{GE}(t|x) \right\|^2 + \left\| \lambda \cdot \left(x - x_{in}\right) \right\|^2 \tag{10}$$

where t_{GE} denote the echo times of the ME-SE and ME-GE acquisitions, respectively, and α is a scalar weighting factor to adjust the influence of the first term, the ME-SE data consistency. Since ME-GE acquisition has the double amount of data (magnitude and phase) than the ME-SE acquisitions (magnitude only), $\alpha = 2$ was chosen for equal weighting of both terms for all simulations and in vivo experiments.

Methods

Single and joint inversion implementation

We iteratively solve the nonlinear inversion problems from Eqs. (7–10) for single and joint inversion with a local-search optimization method, the Levenberg–Marquardt algorithm [18]. At each iteration, we compute the Fréchet derivatives by finite difference. We solve the linearized problem as a classical linear least-squares problem with bounds on the variables, using the *lsq_linear* method from the Scipy Python library. We added a damping term (value 0.01) to the minimization for more stability. Table 1 summarizes the parameters to be inverted (cf. model vector x of Eq. (10)), their initial values, and the upper and lower bounds during minimization. Note that the joint inversion does not explicitly enforce $T_2^* \leq T_2$ during the optimization but implicitly via the forward models in combination with realistic data. With the inversion parameters in Table 1, such a physically impossible solution was never observed for all simulated and in vivo data.

Simulations

Synthetic ME-GE and ME-SE data were generated to test the inversion approaches in simulations with known ground truth. We used a published MW fraction atlas [19] to compute voxel-wise two-pool Gaussian relaxation spectra. The Gaussian integrals were modified to match the respective *MWF* value per voxel. The simulations were repeated six times with different parameters for the Gaussian distributions, which were randomly drawn within certain ranges: $\mu_{1,T_2} \in [16, 22]$ ms, $\mu_{2,T_2} \in [65, 80]$ ms, $\mu_{2,T_2^*} \in [10, 15]$ ms, $\mu_{2,T_2^*} \in [48, 62]$ ms, and $\sigma_{1/2,T_2}/\sigma_{1/2,T_2} \in [0.2, 1]$ ms (cf. Table 1). The compartmental frequency shifts for ME-GE signal simulations were modeled accordingly with $\Delta\omega_1 \in [-2, -10]$ Hz, $\Delta\omega_2 \in [-3, 3]$ Hz, and $\Delta\Phi_0 \in [0, \pi]$. We chose these ranges according to the literature and to ensure $T_2^* \leq T_2$. All other distribution parameters were chosen constant but not too close to the initial model.

From the spectra we computed the ME-GE and ME-SE signals with the respective forward models. The sequence parameters are given in Fig. 1 C: first echo time (TE_1), increment (ΔTE), echo train length (ETL), and ME-SE flip angles (α_e and α_r). After adding Gaussian noise to the real and imaginary part of all signals (SNR = 150 for the first TE) to the signals, individual inversions and joint inversion based on the Levenberg–Marquardt algorithm were compared. For the simulation the same regularization term (0.01) was used for all λ-parameters (cf. Table 1). The workflow for the simulation process is schematically depicted in Fig. 1.

Data acquisition

Measurements were conducted at a 3T MAGNETOM Skyra scanner (Siemens Healthineers) using custom slab selective 3D sequences with 2-mm isotropic resolution to ensure sufficiently high SNR and short echo times. Both sequences, ME-GE and ME-SE, encode the identical FOV of 220 × 220x48 mm^3. While the in-plane axial FOV covers complete transverse slices, the FOV in head-feet direction (48mm) was chosen to cover several important WM structures for region of interest (ROI) analysis (cf. Result section). Furthermore, the repetition times of the ME-GE and ME-SE sequences were matched to TR=900 ms. This is an essential requirement for the analysis, which does not take T_1 relaxation into account.

For time-efficient ME-GE acquisition, we used a custom multi-echo 3D-EPI sequence [20] as a monopolar ME-GE sequence with ramp sampling by setting the EPI factor to 1 and disabling phase correction and echo time shifting. We allowed the sequence to acquire non-equidistant echo times. In order to best capture the MW signal component at short echo times and at the same time minimize the gradient duty cycle, 32 echoes with exponentially increasing spacing were acquired:$\Delta TE_n = \Delta TE_0 \mathrm{e}^{nr\,\Delta TE_0}$, $n = 1, ..., 31$. Consequently, echo times increased according to $TE_n = TE_0 + \Delta TE_0 \left(\mathrm{e}^{nr\,\Delta TE_0} - 1\right) / \left(\mathrm{e}^{r\,\Delta TE_0} - 1\right)$. Using TE_0 =2 ms, ΔTE_0=1.5 ms and increase rate r=0.02, the resulting echo times were: TE_{GE}=[2, 3.5, …, 73.89,77.58] ms. Further sequence parameters were: TR=900 ms, 60° nominal flip angle, 1516 Hz/pixel readout bandwidth, CAIPIRINHA $2 \times 2_{z1}$ parallel imaging, TA=9:08 min (total acquisition time).

The total acquisition time of a purely phase-encoded 3D ME-SE sequence would be too long for in vivo applications [21]. Therefore, we implemented a ME-SE sequence with a

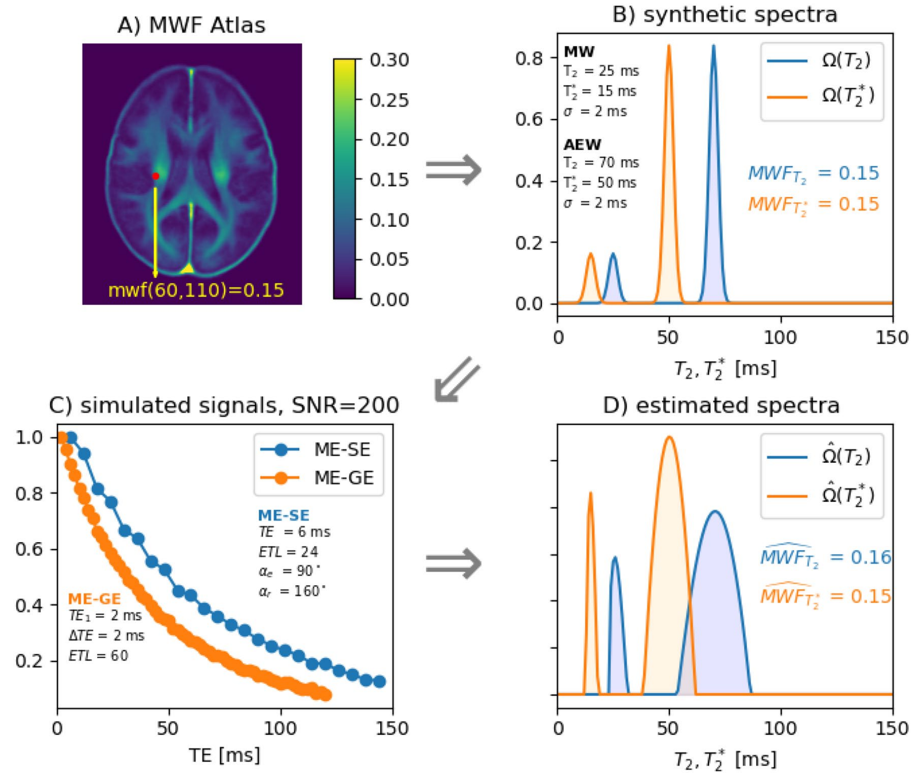

Fig. 1 Workflow of the simulation process. For each voxel from one slice of the MWF atlas (**A**) synthetic relaxation spectra are generated (**B**) with realistic values for the respective Gaussians. Next, ME-GE and ME-SE signals are simulated by applying forward models and adding noise (**C**). Finally, the parametric fitting of the individual inversions provides the estimated spectra and resulting MWF estimates (**D**)

segmented spiral-in/out readout using the Pulseq [22] framework. The sequence diagram is depicted in Fig. 2: after fat suppression and slab selective excitation, a CPMG echo train is applied with nonselective refocusing pulses in order to avoid slice profile effects (which would confound the EPG-based MWF analysis). The spiral readout of the CPMG echo train is strongly segmented to ensure short echo times. Image reconstruction was performed with the BART toolbox [23] using an established open-source MR imaging and reconstruction workflow [24], including correction of spiral trajectory imperfections by means of the GIRF approach [25]. For the in vivo acquisitions the following sequence parameters were chosen, TE_{SE}=6.6 ms (CPMG echo spacing), ETL=24, TR=900 ms (repetition time), 50° nominal excitation flip angle, TA=7:48 min (total acquisition time). These parameters could be achieved utilizing N_s=21 spiral interleaves and N_z=24 phase encoding steps along the slab dimension.

The slightly lower flip angle of ME-SE (50°) compared to ME-GE (60°) ensures the same T_1-saturation for TR =900 ms, assuming $T_1 \approx 900$ ms for the AEW component. It is difficult to measure T_1 of MW, but it is assumed to be much shorter than the T_1 of the AEW component [3, 26]. For instance, T_1 = 118 ms was reported for MW at 3T [27]. Thus, we assume full recovery of the MW component during TR=900 ms for both sequences. In total, this ensures equal (apparent) MWF in ME-GE and ME-SE acquisitions, which is a central requirement for the joint inversion approach.

Both sequences were acquired twice in order to use two-fold averaged data for the single T_2 and T_2^* inversions, whereas the joint inversion is based on single ME-GE and

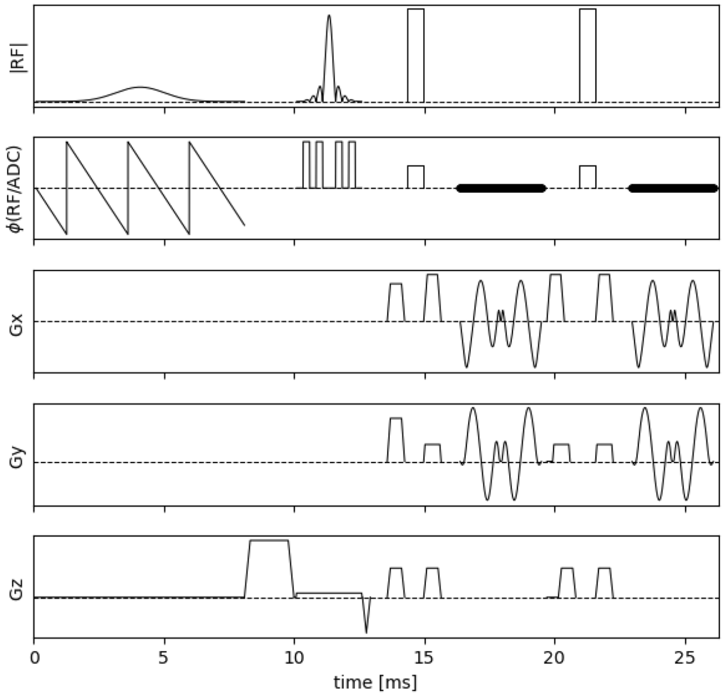

Fig. 2 Diagram of the Pulseq implementation for the ME-SE 3D imaging sequence with in-plane segmented spiral-in/out readout (Gx,Gy) and through-plane phase encoding (Gz). The plot depicts the fat suppression, slab selective excitation, and the first two echoes of the CPMG train with nonselective refocusing pulses. After 24 echoes a fill-time is appended to result in TR=900 ms. This sequence is repeated in a double loop structure acquiring all spiral interleaves (inner loop) and phase encoding steps (outer loop)

ME-SE acquisitions. This way approximately the same amount of data and scan time enters all three inversion approaches.

As a first scan in the experiment, a flip angle (B1) map is acquired with the 3DREAM sequence [28] as required for the EPG signal modeling. The 3DREAM acquisition parameters were: FOV = $220 \times 220 \mathrm{x} 160\ \mathrm{mm}^3$, isotropic resolution of 5 mm, *TA* = 1:41 min. Finally, a custom MP-RAGE sequence [29] with 2D acceleration capabilities [30] was acquired for image registration and segmentation, enabling ROI analysis of the *MWF* estimates. The MP-RAGE acquisition parameters were: FOV = $256 \times 256 \mathrm{x} 172\ \mathrm{mm}^3$, isotropic resolution of 1 mm, *TA* = 3:12 min. The total acquisition time of the entire in vivo protocol was approximately 40 min. Three healthy subjects (age range 34 ± 11 years) were scanned after providing informed consent in accordance with local institutional review board regulations.

Data analysis

A custom data analysis pipeline was implemented in Python. First, the B1 map was registered to the ME-GE/ME-SE images with the *AntsPy* library. Voxel-wise single and joint inversions were performed as described above. For the single inversions, the average of the two respective ME-GE and ME-SE acquisitions was used, whereas the joint inversion was applied to single acquisitions (the first one for both, ME-GE and ME-SE). The subjects were highly compliant and we did not observe any misalignment between the datasets. Therefore, in order to avoid re-slicing errors, image registration was neither performed between ME-GE and ME-SE data (for joint inversion) nor between repeated scans (for single inversions). However, averaging of the complex ME-GE data required phase-matching between the two scans to account for local frequency and phase drifts, e.g., due to gradient heating. To this end, a voxel-wise linear fit of the TE-dependent phase change between repeated ME-GE scans was performed and then subtracted from the phase of the repeated scan before complex-valued averaging.

Single and joint inversions were performed voxel-by-voxel as described above. The inversion of ME-GE data and the joint inversion were run twice, once with the suggested complex signal model (including compartmental frequency shifts), and once with the simplified mono-exponential decay model. Here, the ME-GE inversion problem is similar to

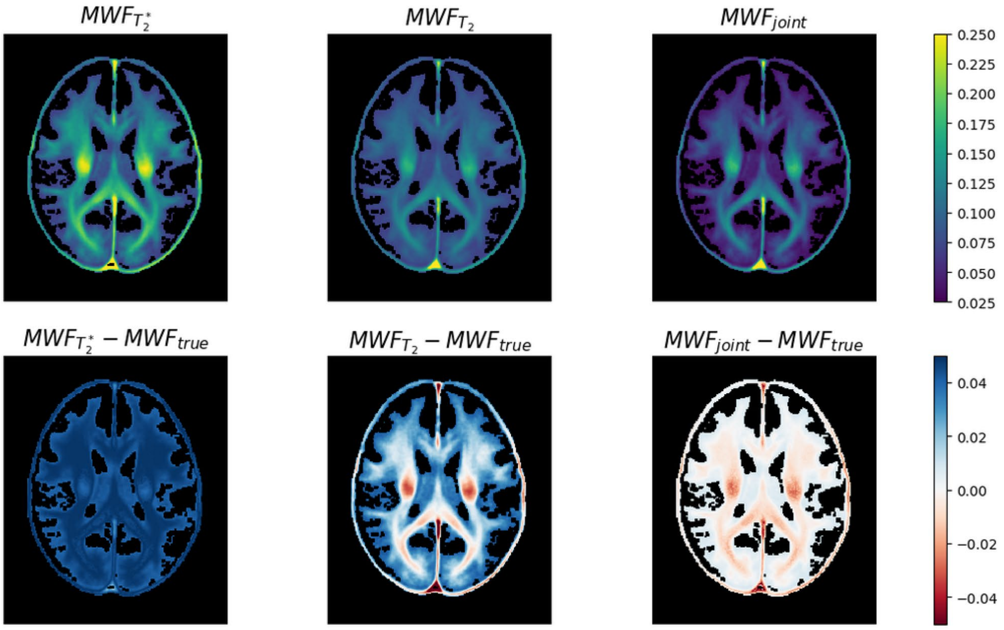
$MWF_{T_2^*}$
MWF_{T_2}
MWF_{joint}
0.250
0.225
0.200
0.175
0.150
0.125
0.100
0.075
0.050
0.025
$MWF_{T_2^*} - MWF_{true}$
$MWF_{T_2} - MWF_{true}$
$MWF_{joint} - MWF_{true}$
0.04
0.02
0.00
−0.02
−0.04

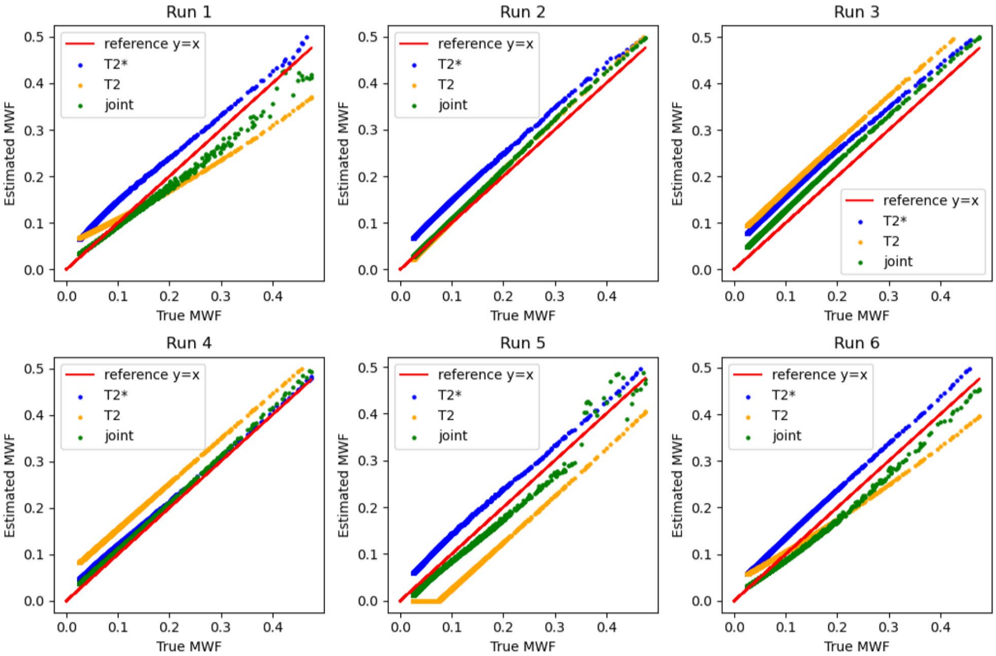
Run 1
Run 2
Run 3
Run 4
Run 5
Run 6
reference y=x
T2*
T2
joint
Estimated MWF
True MWF
0.0
0.1
0.2
0.3
0.4
0.5

◀**Fig. 3** Depiction of the simulation results. The top row of images shows the estimated MWF maps from one simulation run of the single (T_2 and T_2^*) inversions and the joint inversion. The second row of images show the respective deviations to the ground truth. The last two rows show scatter plot for all simulation runs displaying the deviation between the estimated MWF and the true MWF. The data points show the MWF values in the individual voxels for the repeated simulation runs and within the (discontinuous) range of MWF values present in the depicted slice of the atlas

Eq. (7) for ME-SE data, i.e., only the six parameters of the T_2^* are estimated. (Likewise, the joint inversion reduces to 9 parameters instead of 14, cf. Table 1.) To ensure equal weighting for the joint inversion, ME-GE and ME-SE data were normalized prior to the analysis, $S_{GE/SE}\left(TE_{min}\right) \equiv 1$. A slightly higher regularization for the parameters of the MW component was chosen in comparison to the simulation (cf. Table 1). However, again the same regularization parameters were applied in single and joint inversions. This slight increase in regularization showed more homogeneous MWF results for all three inversion methods (comparison not shown), potentially counteracting a model-induced bias for real data.

Probability GM and WM maps were generated from the MP-RAGE with SPM12 (MATLAB vR2022a) [31]. Only voxels with a probability higher than 95% were included to create the respective masks. Registration from the MP-RAGE to the ME-SE and ME-GE spaces were performed with *ANTs* [32] using a rigid transformation, which was then applied to the GM and WM masks. To obtain WM tract ROIs, we used the JHU ICBM-DTI-81 WM atlas [33]. The MNI 152 T1 template was registered to the ME-GE and ME-SE spaces with *ANTs* using a symmetric normalization (SyN), which was then applied to the atlas. Ten regions were included in the analysis: total WM, ALR (anterior limb of the internal capsule—right), ALL (anterior limb of the internal capsule—left), PLR (posterior limb of the internal capsule—right), PLL (posterior limb of the internal capsule—left), GCC (genu of the corpus callosum), BCC (body of the corpus callosum), SCC (splenium of the corpus callosum), AF (anterior forcepts) and PF (posterior forcepts). Parameter estimation was performed in the native space. Finally group statistics across all ROI voxels and subjects were computed to obtain mean and standard deviation of the estimated model parameters.

Results

Simulation results

The top row in Fig. 3 depicts *MWF* maps resulting from from one simulation run of the single inversions (T_2 and T_2^*) and the joint inversion. To emphasize the comparison with the *MWF* atlas (ground truth), the second row shows the difference maps, where the sign indicates if the *MWF* was over- or underestimated. It can be seen that the joint inversion *MWF* estimate is closer to the ground truth than the single inversions. The last two rows of Fig. 3 depict cross-plots for all six simulation runs, displaying the voxel-wise estimated *MWF* values against the ground truth. The closer the points to the identity ($x = y$), the more accurate the inversion. For example, in Run 5 the T_2^* inversion overestimates the *MWF* and the T_2 inversion underestimates the *MWF*, while the joint inversion lies in between. In Run 3 all inversions overestimate the *MWF*, but the joint inversion is closest to the ground truth. When a single inversion provides a good estimate, then the joint inversion is close to these values (Runs 2 and 4). In general, the plots show that the joint inversion is closer to the ground truth than the single inversions for almost all data points. In most cases, the observed error of the *MWF* estimates resulted from deviations in the estimated integrals (I_1, I_2), while the estimates of Gaussian mean and standard deviation was always very close to the ground truth.

In-vivo results

The in vivo results shown in this section depict a single representative slice for each of the three subjects. Fly-through movies showing the quantitative maps for all slices (and subjects) are provided as Supporting Information Videos S1-2. Figure 4 shows the acquired ME-GE and ME-SE imaging data for all subjects and a subset of all echo times (see figure legend). The images are free of obvious artifacts and generally good image quality was observed in all cases. The image SNR of the first echo was in the range of 200 for both sequences and all subjects. The *MWF* results of the single inversions (T_2 and T_2^*) and the joint inversion are shown in Fig. 5 for all subjects. All inversion methods show increased *MWF* values in WM compared to GM, as expected. The most obvious differences between single and joint inversion results are the reduced blurring and overall more distinct contours in the joint inversion *MWF* maps, which results in sharper depiction of WM structures. This effect becomes even more evident when only the ME-GE magnitude data is used for the inversion, as shown in Fig. 6. Here, the *MWF*-map from the single T_2^* inversion is more blurred as compared to corresponding map in Fig. 5. Again, the joint inversion produces the most detailed *MWF* map. However, large *MWF* values potentially arising from frequency-shift induced signal changes in WM are present in both maps. Finally, the effect of regularization is shown in Fig. 7. Here, the results were obtained with low regularization for all model parameters (λ=0.005), leading to very low-quality *MWF*

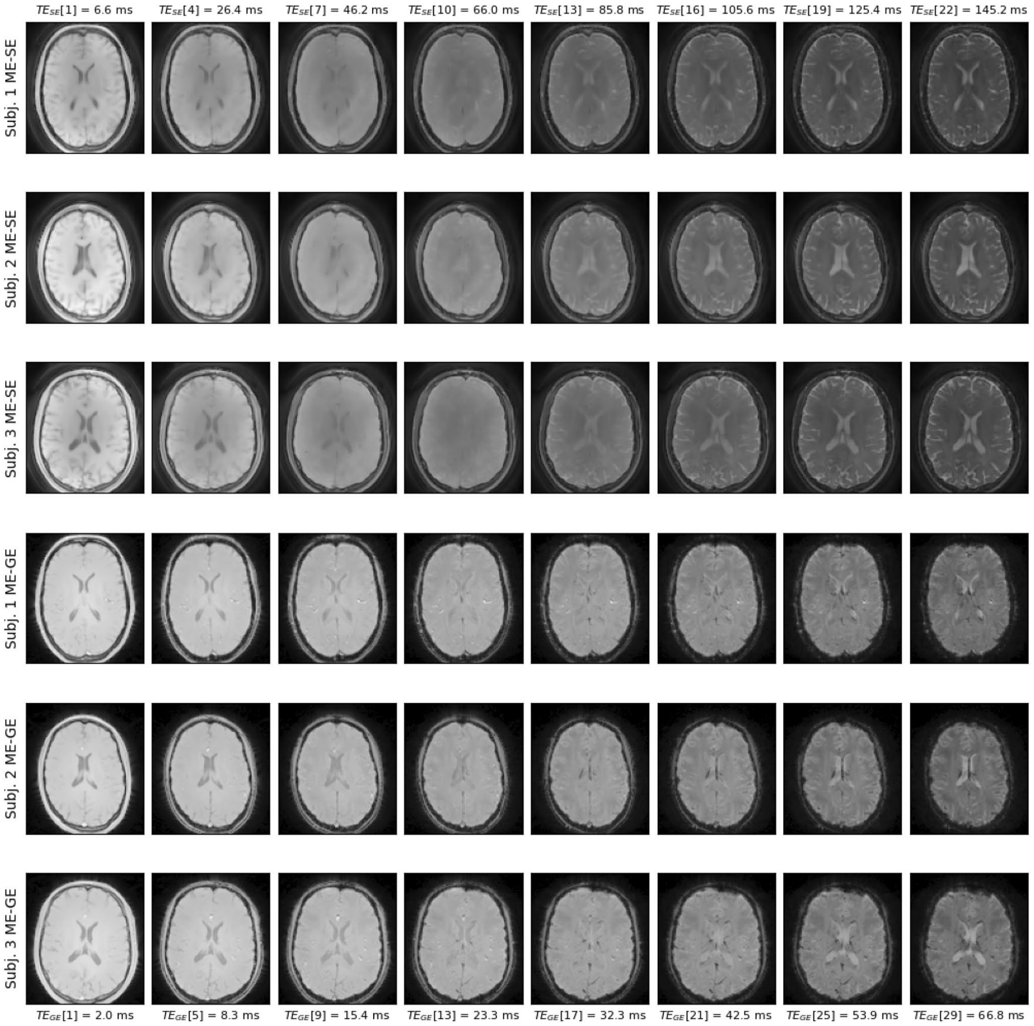

Fig. 4 Single slice imaging data from all three subjects. The first three rows show ME-SE images and the last three rows show ME-GE images. The columns show the signal decay at eight echo times (TEs) over the entire range of the echo train. The TEs of ME-SE and ME-GE are given in the labels at the top and at the bottom, respectively. Note that $\mathrm{TE}_{\mathrm{GE}}^{\max} \ll \mathrm{TE}_{\mathrm{SE}}^{\max}$

maps for the single T_2^* inversion. This underlines the need for regularization, also in the case of joint inversion.

A quantitative evaluation of all estimated parameters is presented in Table 2, showing group averaged fit results in several WM ROIs, which are present in the acquired 3D slab. Interestingly, the joint inversion method often produces *MWF* mean values that are higher than those observed from inverting the ME-SE and ME-GE datasets separately. The group standard deviations, given in brackets in Table 2, indicate that there are only small differences

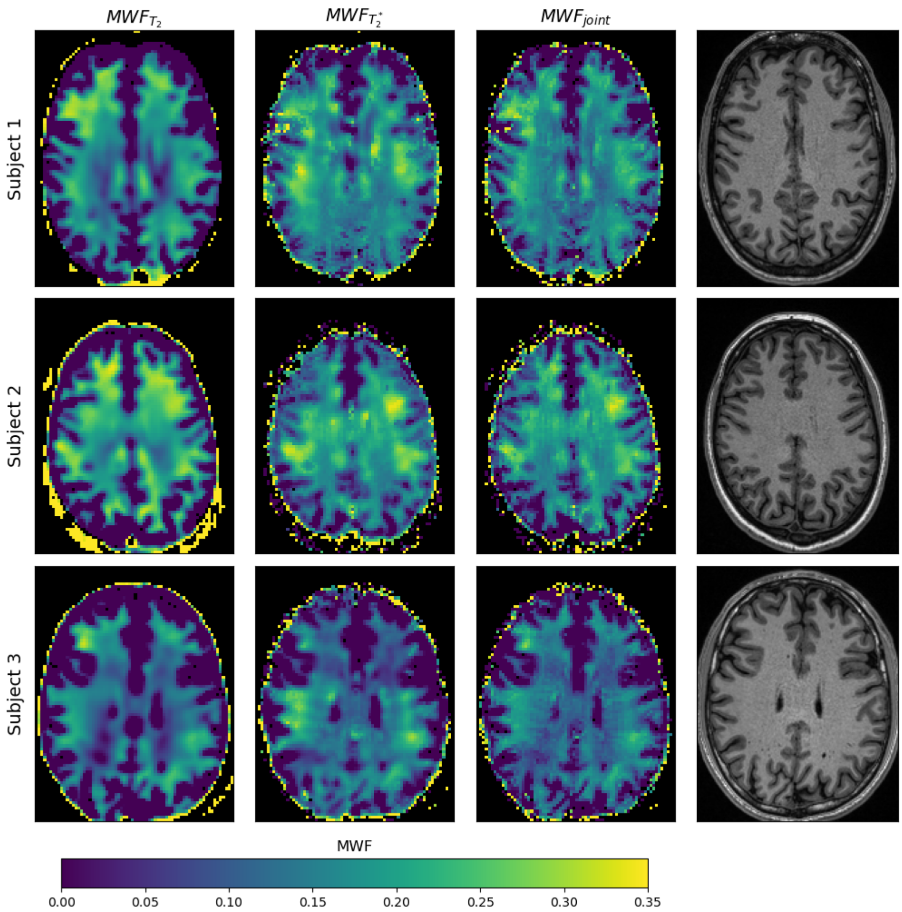

Fig. 5 MWF results for all subjects for single inversions (first and second column) and for the joint inversion (third column). The last column shows the respective slice of the T_1-weighted scan for anatomical reference. For all three inversion methods the estimated MWF values are consistently higher in WM than in GM and CSF and lie in the expected range known from the literature. The joint inversion maps appear less blurred and show less variation within in WM as compared to the maps from the single inversions

between subjects for all estimated parameters, especially for the MWF. This quantitative observation, which holds for single and joint inversions, may not be visually supported when inspecting Fig. 5. Here, the colorbar scaling was chosen to enhance regional differences in MWF, which also visually enhances variation between subjects. Finally, the correlations between the estimated parameters are provided as supporting information S3 for single and joint inversions, showing that parameter estimates are mostly independent of each other (Fig. 7).

Discussion

MWI is a practical approach for indirect in vivo quantitative mapping of brain myelin content, an important marker for understanding brain development, aging, plasticity, and degeneration. However, due to technical limitations MWI may report biased values of the true myelin concentration. In order to improve the accuracy of MWF estimates, we acquired and jointly analyzed ME-GE and ME-SE imaging data. MWI requires the estimation of the respective relaxation spectra, which is a highly ill-posed inverse problem. Strong regularization is typically required to enforce a stable

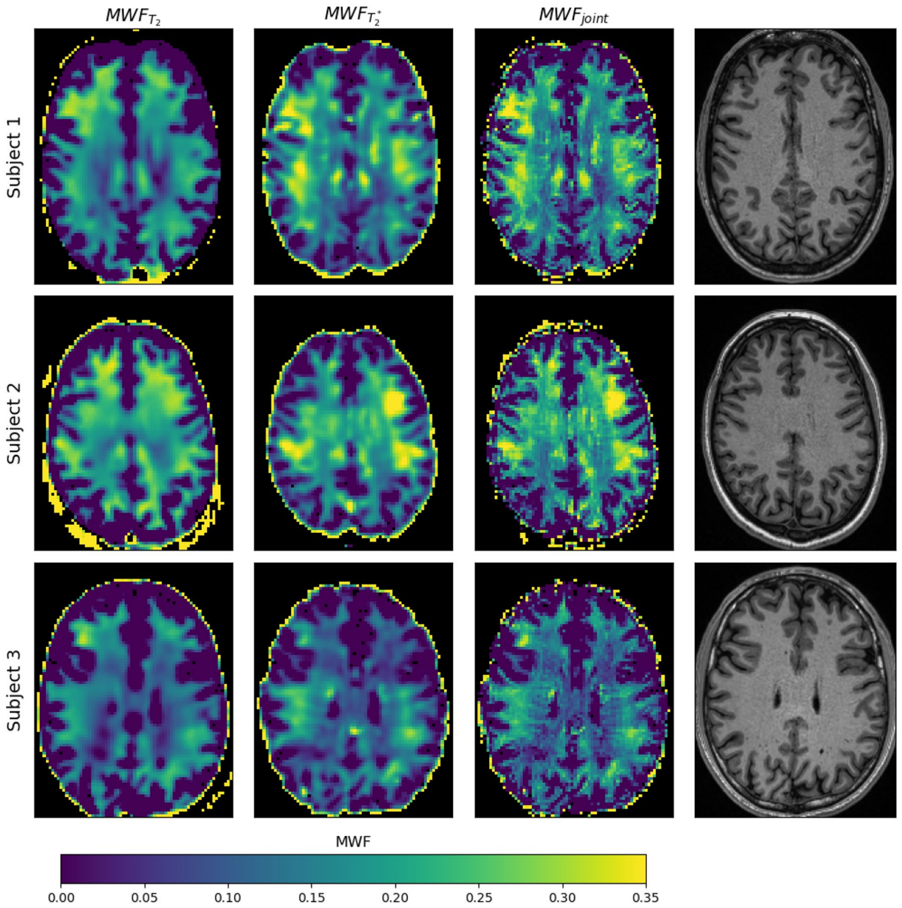

Fig. 6 Same display of MWF results as in Fig. 5 but without taking compartmental frequency shifts into account for the MWF$_{T_2^*}$ and the MWF$_{\mathrm{joint}}$ fit. (The MWF$_{T_2}$ fit is exactly the same as in Fig. 5 and again displayed for comparison.) Regionally high MWF values can be observed in the MWF$_{T_2^*}$-map, which also transfers to the MWF$_{\mathrm{joint}}$ map. This is especially pronounced for subjects 1 and 2 and might be attributed to frequency shifts in white matter fiber bundles

solution, which usually results in biased *MWF* estimates. We hypothesized that jointly inverting both datasets reduces the ill-posedness of the inverse problem, potentially relaxing the need for strong regularization. For this, it was implicitly assumed that ME-GE and ME-SE provide independent measures of *MWF*. Under this assumption, we formulated an objective function with data consistency terms for ME-GE and ME-SE data. The forward operators to compute the respective signals were constructed through parameterized two-pool Gaussian spectra describing the MW and AEW components. For ME-GE and ME-SE signals, they are given by the T_2^* and the T_2 voxel-distribution, respectively. Under the stated assumption, both distributions share the same *MWF* which therefore can be jointly inverted from both datasets.

Our results suggest that the joint inversion approach mitigates the ill-posed nature of the inversion problem inherent in MWI. The underdetermined inverse problem can lead to ambiguity and instability in the reconstruction process when relying on a single dataset. By combining information from both sequences, our method introduces additional constraints that inherently help to regularize the inversion process, thereby improving the stability and accuracy of the estimated *MWF*.

Table 2 Group statistics of the quantitative fit results (rows) for several ROIs (columns): *WM* (white matter), *ALR* (anterior limb of the internal capsule—right), *ALL* (anterior limb of the internal capsule—feft), *PLR* (posterior limb of the internal capsule—right), *PLL* (posterior limb of the internal capsule—left), *GCC* (genu of the corpus callosum), *BCC* (body of the corpus callosum), *SCC* (splenium of the corpus callosum), *AF* (anterior forcepts), *PF* (posterior forcepts)

	WM	ALR	ALL	PLR	PLL	GCC	BCC	SCC	AF	PF
MWF ME-SE	0.12 (0.01)	0.22 (0.02)	0.09 (0.05)	0.2 (0.01)	0.19 (0.02)	0.11 (0.02)	0.05 (0.02)	0.05 (0.01)	0.13 (0.02)	0.07 (0.02)
MWF ME-GE	0.13 (0.01)	0.22 (0.02)	0.11 (0.04)	0.19 (0.01)	0.18 (0.02)	0.12 (0.03)	0.08 (0.01)	0.12 (0.02)	0.1 (0.02)	0.14 (0.01)
MWF joint	0.17 (0.01)	0.2 (0.01)	0.22 (0.03)	0.22 (0.01)	0.23 (0.01)	0.09 (0.01)	0.13 (0.01)	0.18 (0.01)	0.12 (0.01)	0.18 (0.01)
MW T_2 ME-SE	18.21 (0.05)	18.75 (0.15)	18.72 (0.12)	18.17 (0.03)	18.2 (0.05)	18.19 (0.1)	18.01 (0.08)	18.07 (0.03)	18.31 (0.07)	18.06 (0.01)
MW T_2 joint	18.86 (0.2)	22.27 (0.38)	21.27 (0.63)	18.67 (0.06)	18.77 (0.33)	21.87 (0.7)	17.75 (0.31)	17.75 (0.34)	21.96 (0.17)	17.82 (0.16)
AEW T_2 ME-SE	80.67 (0.58)	80.22 (0.63)	79.36 (0.07)	79.73 (0.06)	79.42 (0.24)	79.71 (0.24)	91.18 (8.38)	82.97 (1.28)	78.81 (0.59)	81.6 (0.96)
AEW T_2 joint	83.13 (1.64)	78.32 (0.13)	88.52 (6.51)	79.33 (0.12)	80.03 (0.73)	83.05 (2.22)	100.78 (12.01)	96.82 (3.55)	81.4 (1.54)	86.7 (4.33)
MW T_2^* ME-GE	12.23 (0.02)	12.74 (0.29)	13.21 (0.67)	12.52 (0.16)	12.7 (0.41)	15.43 (0.56)	11.56 (0.51)	13.33 (0.25)	13.21 (0.11)	13.67 (0.11)
MW T_2^* joint	10.64 (0.02)	13.21 (0.65)	11.37 (0.52)	11.57 (0.3)	10.93 (0.11)	10.61 (0.22)	10.43 (0.28)	11.94 (0.59)	10.39 (0.2)	11.45 (0.15)
AEW T_2^* ME-GE	59.87 (0.58)	58.09 (0.21)	62.62 (2.82)	58.64 (0.36)	58.14 (0.7)	60.27 (0.79)	64.42 (3.49)	63.33 (1.24)	59.47 (0.65)	60.59 (0.95)
AEW T_2^* joint	58.56 (0.44)	58.72 (1.32)	58.32 (0.64)	58.66 (0.63)	57.44 (1.56)	61.3 (1.13)	66.7 (6.76)	60.98 (0.98)	56.19 (1.85)	59.59 (0.87)

Each row shows the group mean value in the ROI and below the standard deviation in brackets. The first three rows compare the MWF estimates for single and joint inversions. The next eight rows show T_2 and T_2^* estimates of the MW and the AEW component for the respective inversion approaches

The simulation results presented in this study demonstrate the superiority of the proposed joint inversion approach over conventional methods that rely on a single dataset for MWI. The main advantage of the simulation is the knowledge of the ground truth (completely defined by the known T_2 and T_2^* model), which enables to determine and compare the accuracy of the different inversion methods. For the single T_2 and T_2^* inversions, we observed under- and overestimation for a wide range of the true *MWF* values. Instead, the *MWF* joint inversion estimates were closer to the ground truth in almost all cases. These results were obtained for SNR = 150 of the respective first echo of the synthetic data. In simulations with much lower SNR, all three estimates, also the join inversion, significantly deviate from the true *MWF* values. If the SNR is increased beyond 150, the advantage of the joint inversion remains but gets smaller, since also the bias of the individual inversions decreases. Thus, the improvement in accuracy seems to be particularly noteworthy when considering the challenges posed by realistic SNR.

The superiority of the joint inversion approach is further corroborated by the results obtained from in vivo data. Here, the ground truth is not known and biases due to incorrect model assumptions may enter as well (cf. subsection Limitations below). In contrast, the joint inversion produces sharper MW fraction maps which highlight its ability to provide enhanced spatial resolution and tissue contrast compared to the conventional approaches. The improved level of detail is a result of leveraging additional information from a second dataset during the joint inversion process. The two datasets have different sensitivities and resolution characteristics. This complementary information reduces the influence of regularization although the same regularization method and strength were applied to single and joint inversions. The joint inversion problem is less ill-posed and less impacted by regularization, which lead to more detailed images. The improved results of the joint inversion are not related to enhanced SNR from the bigger dataset, as it was compared to the single inversions of two repeated scans, which resulted in approximately the same amount of data and scan time. Indeed, the results from single inversions on

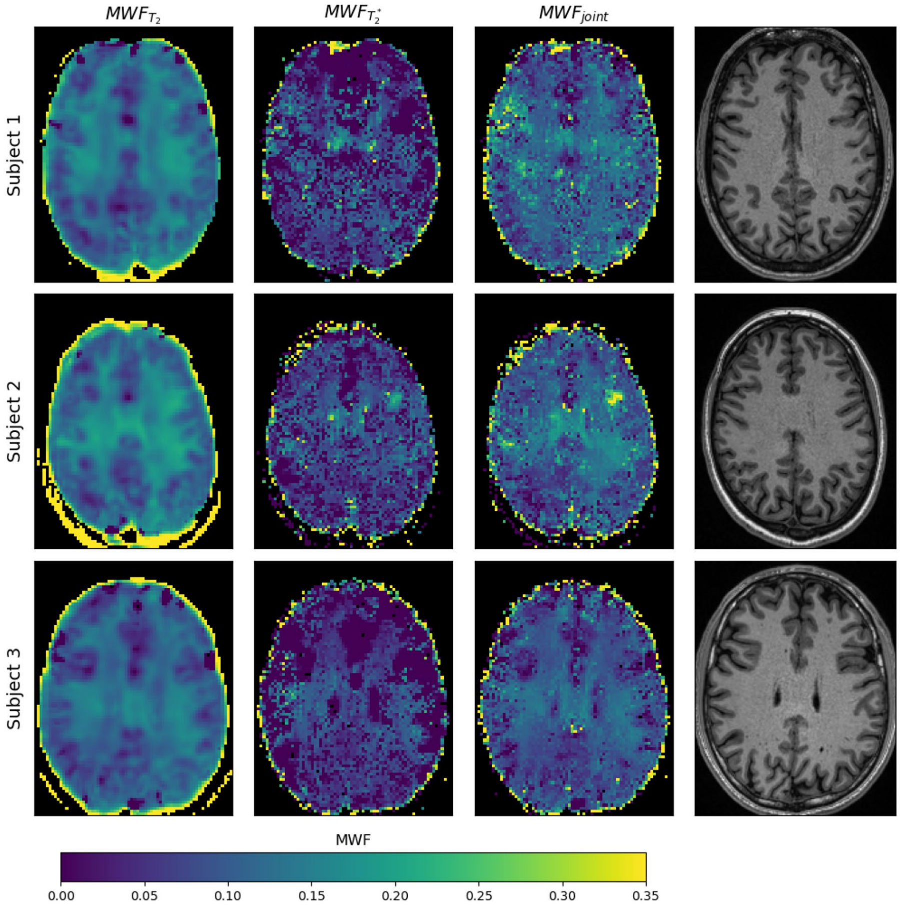

Fig. 7 Same display of MWF results as in Fig. 5 but using low regularization in the inversion ($\lambda = 0.005$ for all model parameters). While T_2 inversion is less affected, the T_2^* result is dominated by noise, which also takes over to the joint inversion results

single datasets (not shown), are very similar to those from the averaged scans. This might be attributed to the high SNR already present in the single acquisitions. The joint inversion is better constrained since it inverts simultaneously multiple types of data, which help to reduce the solution space in comparison with the single inversions. The joint inversion can also average out the noise from the single datasets, leading to more reliable results. Moreover, T_2 and T_2^* inversions seem to solve the minimization problems differently: the MWF_{T_2} maps are less noisy while the $MWF_{T_2^*}$ maps are less blurred (in case of a complex signal model, cf. Figure 5). Joint inversion leverages the strengths of both data types, leading to higher resolution models. Noteworthy, the group statistics in WM ROIs (cf. Table 2) show that the joint inversion MWF is mostly larger than the estimates of the single inversions. However, due to the lack of a ground-truth, it remains to be shown if the in vivo MWF estimates are more accurate than those obtained from the single inversions. Although this observation is supported by the simulation results, it cannot be generalized to the case of in vivo data (cf. limitations below). Nevertheless, the main advantage of the joint inversion approach is the obvious improvement in resolution as compared to the results based on a single dataset. Table 2 also shows that the different fits of the MW and AEW relaxation times are in good agreement in most ROIs. This indicates that the joint inversion consistently found the same local optima for the respective distributions (T_2 and T_2^*) as the single inversions. Noteworthy are also the small group standard deviations of all estimates and ROIs, indicating that all inversion approaches provide stable cross-subject results in healthy volunteers. However, this observation needs to be confirmed using a larger sample, as only three subjects were included in this proof-of-concept study.

Several limitations warrant consideration. First, the simulation results have to be interpreted with care since the data are modeled with the same algorithm as used for inversion. This scenario is called *inverse crime* in geophysics: during the iterative fitting process, the data consistency terms will produce perfect gradient estimation and therefore facilitating convergence during the inversion. In real data, the residuals in addition contain deficiencies in the modeling algorithm that leads to gradient errors too. Thus, for instance, it would be not useful to compare the performance of conventional NNLS inversion with parameterized inversion while using the same parametric model for generating synthetic data. In that case the data would perfectly fit to one approach but not to the other, and the results would be misleading. Therefore, NNLS was not considered in the simulations. For the in vivo data we also performed conventional NNLS inversion individually on ME-GE and ME-SE data. The results (not shown) were similar but slightly worse as compared to the parameterized single inversions, as expected [6]. Another limitation of the current approach is that B_0 field inhomogeneities were not taken into account. Due to the high readout bandwidth of the ME-GE sequence image distortions are minimal, yet the multi-exponential T_2^* decay model might be invalid in regions with large ΔB_0 [34]. Furthermore, phase images contain multiple phase wraps in these regions, which results in unstable *MWF* fits for both, single inversion ME-GE and joint inversion (cf. *MWF* maps in the supplementary material). Improved phase preprocessing may help to overcome these problems. However, since we mainly focused on *MWF* estimates in WM, we assume that susceptibility-induced field inhomogeneities have minor influence on the presented results. The proposed inversion method, especially the proposed initial model and regularization parameters, may be sensitive to variations in acquisition parameters and pathology-dependent tissue properties, necessitating further validation across different imaging protocols and patient populations. Finally, the results were obtained on high SNR data resulting from rather lengthy acquisitions (20 min), as good data quality was seen as a requirement for this proof-of-concept study. The impact of reduced SNR in accelerated acquisitions needs to be investigated in future, aiming at faster protocols suitable for patient studies.

In conclusion, this study demonstrates the effectiveness of a novel joint inversion approach for MWI, which integrates information from multi-echo spin-echo and gradient-echo imaging sequences to improve the accuracy and reliability of MW quantification. The observed improvements in accuracy and spatial resolution, coupled with the potential clinical implications, underscore the significance of our proposed method in advancing neuroimaging research and clinical practice. Future work will focus on further refining the proposed approach and validating its utility in clinical studies, e.g., multiple sclerosis (MS) patients.

Supplementary Information The online version contains supplementary material available at https://doi.org/10.1007/s10334-025-01235-5.

Acknowledgements This work received financial support from the Helmholtz Association, Initiative and Networking Fund, funding code ZT-I-PF-4-006 (Helmholtz Imaging Project “JIMM”). SD received a HIDA Trainee Network Grant, also from the Helmholtz Association. MF and TS received funding from German Federal Ministry of Education and Research (BMBF; funding code 01ED2109A) as part of the SCAIFIELD project under the aegis of the EU Joint Programme—Neurodegenerative Disease Research (JPND).

Funding Open Access funding enabled and organized by Projekt DEAL.

Declarations

Conflict of interest All authors declare that they have no conflict of interest.

Ethical approval All procedures performed in studies involving human participants were in accordance with the ethical standards of the institutional committee. Informed consent was obtained from all individual participants included in the study.

References

1. Laule C, Vavasour IM, Kolind SH, Li DKB, Traboulsee TL, Moore GRW, MacKay AL (2007) Magnetic resonance imaging of myelin. Neurotherapeutics 4:460–484
2. Alonso-Ortiz E, Levesque IR, Pike GB (2014) MRI-based myelin water imaging: a technical review. Magn Reson Med 81:70–81
3. Lee J, Hyun JW, Lee J, Choi EJ, Shin H G, Min K, Nam Y, Kim HJ Oh S H (2021) So you want to image myelin using mri: an overview and practical guide for myelin water imaging. J Magn Reson Imaging 53:60–373
4. MacKay A, Laule C, Vavasour I, Bjarnason T, Kolind S, Mädler B (2006) Insights into brain microstructure from the T2 distribution. Magn Reson Imaging 24:515–25

5. Du YP, Chu R, Hwang D, Brown MS, Kleinschmidt-DeMasters BK, Singel D, Simon JH (2007) Fast multislice mapping of the myelin water fraction using multicompartment analysis ofT2* decay at 3T: a preliminary postmortem study. Magn Reson Med 58:865–870
6. Raj A, Pandya S, Shen X, LoCastro E, Nguyen TD, Gauthier SA (2014) Multi-compartment T2 relaxometry using a spatially constrained multi-Gaussian model. PLoS ONE 9:e98391
7. Nam Y, Lee J, Hwang D, Kim D-H (2015) Improved estimation of myelin water fraction using complex model fitting. Neuroimage 116:214–221
8. Wharton S, Bowtell R (2012) Fiber orientation-dependent white matter contrast in gradient echo MRI. Proc Natl Acad Sci USA 109:18559–18564
9. Vozoff K, Jupp DLB (1974) Joint inversion of geophysical data. Geophys J Roy Astron Soc 42:977–991
10. Linde N, Doetsch J (2016) Joint Inversion in Hydrogeophysics and Near-Surface Geophysics. In: Moorkamp M, Lelièvre PG, Linde N, Khan A (eds) Geophysical Monograph Series. Wiley, pp 117–35
11. Paasche H, Tronicke J (2007) Cooperative inversion of 2D geophysical data sets: A zonal approach based on fuzzy $\boldsymbol{c}$ -means cluster analysis. GEOPHYSICS 72:A35-9
12. Lebel RM, Wilman AH (2010) Transverse relaxometry with stimulated echo compensation. Magn Reson Med 64:1005–1014
13. Hennig J (1991) Echoes-how to generate, recognize, use, or avoid them in mr-imaging sequences. part ii: echoes in imaging sequences. Concepts Magn Reson 3:179–192
14. Scheffler K (1999) A pictorial description of steady-states in rapid magnetic resonance imaging. Concepts Magn Reson 11:291–304
15. Prasloski T, Mädler B, Xiang Q-S, Mackay A, Jones C (2011) Applications of stimulated echo correction to multicomponent T(2) analysis. Magn Reson Med : Off J Soc Magn Reson Med/Soc Magn Reson Med 67:1803–1814
16. Van Gelderen P, De Zwart JA, Lee J, Sati P, Reich DS, Duyn JH (2012) Nonexponential T_2 * decay in white matter. Magn Reson Med 67:110–7
17. Song JE, Kim D-H (2022) Improved multi-echo gradient-echo-based myelin water fraction mapping using dimensionality reduction. IEEE Trans Med Imaging 41:27–38
18. Gavin HP 2024 The Levenberg-Marquardt algorithm for nonlinear least squares curve-fitting problems *Duke University*
19. Liu H, Rubino C, Dvorak AV, Jarrett M, Ljungberg E, Vavasour IM, Lee LE, Kolind SH, MacMillan EL, Traboulsee A, Lang DJ, Rauscher A, Li DKB, MacKay AL, Boyd LA, Kramer JLK, Laule C (2019) Myelin water atlas: a template for myelin distribution in the brain. J Neuroimaging 29:699–706
20. Stirnberg R, Stöcker T (2021) Segmented K-space blipped-controlled aliasing in parallel imaging for high spatiotemporal resolution EPI. Magn Reson Med 85:1540–1551
21. Prasloski T, Rauscher A, Mackay AL, Hodgson M, Vavasour IM, Laule C, Mädler B (2012) Rapid whole cerebrum myelin water imaging using a 3D GRASE sequence. Neuroimage 63:533–539
22. Layton KJ, Kroboth S, Jia F, Littin S, Yu H, Leupold J, Nielsen JF, Stocker T, Zaitsev M (2017) Pulseq: a rapid and hardware-independent pulse sequence prototyping framework. Magn Reson Med 77:1544–52
23. Uecker M, Tamir JI, Ong F, Lustig M 2016 The BART toolbox for computational magnetic resonance imaging. 24th Annual Meeting of ISMRM (Singapore)
24. Veldmann M, Ehses P, Chow K, Nielsen J, Zaitsev M, Stöcker T (2022) Open-source MR imaging and reconstruction workflow. Magn Reson Med 88:2395–2407
25. Vannesjo SJ, Graedel NN, Kasper L, Gross S, Busch J, Haeberlin M, Barmet C, Pruessmann KP (2016) Image reconstruction using a gradient impulse response model for trajectory prediction. Magn Reson Med 76:45–58
26. Oh SH, Bilello M, Schindler M, Markowitz CE, Detre JA, Lee J (2013) Direct visualization of short transverse relaxation time component (ViSTa). NeuroImage 83:485–92
27. Labadie C, Lee JH, Rooney WD, Jarchow S, Aubert-Frécon M, Springer CS, Möller HE (2014) Myelin water mapping by spatially regularized longitudinal relaxographic imaging at high magnetic fields. Magn Reson Med 71:375–387
28. Ehses P, Brenner D, Stirnberg R, Pracht ED, Stöcker T (2019) Whole-brain B1-mapping using three-dimensional DREAM. Magn Reson Med 82:924–34
29. Mugler JP III, Brookeman JR (1990) Three-dimensional magnetization-prepared rapid gradient-echo imaging (3D MP RAGE). Magn Reson Med 15:152–7
30. Brenner D, Stirnberg R, Pracht ED, Stöcker T (2014) Two-dimensional accelerated MP-RAGE imaging with flexible linear reordering. Magma (New York, N.Y) 27:455–62
31. Friston KJ, Ashburner JT, Kiebel S, Nichols TE and Penny WD (2007) Statistical Parametric Mapping: The Analysis of Functional Brain Images. London: Elsevier/Academic Press
32. Avants B, Epstein C, Grossman M, Gee J (2008) Symmetric diffeomorphic image registration with cross-correlation: evaluating automated labeling of elderly and neurodegenerative brain. Med Image Anal 12:26–41
33. Mori S, Waskana S, Nagae-Poetscher LM, Van Zijl PCM (2005) MRI Atlas of Human White Matter von Susumu Mori, S. Wakana, Peter C M van Zijl, L.M. Elsevier, Amsterdam
34. Yablonskiy DA, Sukstanskii AL, Luo J, Wang X (2013) Voxel spread function method for correction of magnetic field inhomogeneity effects in quantitative gradient-echo-based MRI. Magn Reson Med 70:1283–1292

4. Discussion with references

This thesis provides a comprehensive, cross-sectional and longitudinal assessment of neurodegeneration in the rare movement disorder spinocerebellar ataxia type 3 (SCA3). Across two disease-focused studies, structural and microstructural MRI markers were evaluated in more than 150 mutation carriers. These data with a clinical focus are complemented by a third study, which presents methodological improvements in myelin water estimation, offering a foundation for future development of sensitive imaging biomarkers in SCA3.

4.1 Regional and Temporal Characteristics of Volume Atrophy in SCA3

Volumetric analyses showed early and consistent involvement of infratentorial brain structures. Particularly, the conducted cross-sectional studies revealed a prominent loss of cerebellar white matter in SCA3. Longitudinally, volume loss was first detectable in the medulla oblongata, followed by the pons. Among all regions assessed, pons volume emerged as the most responsive marker across disease stages, including the pre-symptomatic phase before clinical onset of symptoms. Trajectory modelling revealed that regional decline follows distinct temporal patterns, with the pons and cerebellar white matter showing the steepest volume loss over time.

4.2 Diffusion and Myelin Imaging

Diffusion MRI identified cross-sectional abnormalities in the cerebellar peduncles in pre-symptomatic individuals, especially reduced fractional anisotropy (FA) in the inferior and superior peduncles. However, these metrics showed poor longitudinal sensitivity and high intra-subject variability. These findings likely reflect both the limitations of tensor-derived metrics in regions of complex fibre architecture (Jeurissen et al., 2014) and the technical constraints of the acquisition protocol.

While not yet applied to the SCA3 cohort, the myelin water imaging method developed within this thesis addresses key limitations of conventional T_2-based approaches. By jointly inverting multi-echo spin-echo and gradient-echo data, the method improves anatomical fidelity and estimation stability, particularly in regions affected by partial volume effects and B_1 inhomogeneity. These improvements are relevant for future studies in SCA3, as the findings of this thesis provide evidence for early myelin alterations.

4.3 Implications for the Imaging of SCA3 Pathophysiology

The predominance of white matter degeneration in infratentorial structures suggests that SCA3 pathophysiology involves mechanisms beyond neuronal loss alone. Early and progressive atrophy of cerebellar white matter, as seen in both cross-sectional and longitudinal analyses, raises the possibility of glial dysfunction contributing to the development of the disease. This interpretation is consistent with preclinical findings showing impaired oligodendrocyte maturation and early myelin disruption in SCA3 models (Haas et al., 2022; Schuster et al., 2022). While direct imaging of myelin was not possible, the anatomical pattern and timing of volume loss alongside diffusion alterations are compatible with an early vulnerability of white matter tracts, particularly those in brainstem–cerebellar circuits.

4.4 Multimodal Comparison of Imaging, Clinical, and Fluid Markers

The comparative analysis of imaging, fluid, and clinical measures underscored the limitations of currently used markers. The Scale for the Assessment and Rating of Ataxia, while established as a clinical endpoint, showed delayed and less pronounced change relative to volumetric imaging markers. Moreover, mutant ataxin-3 protein concentrations remained stable across disease stages and were not associated with progression. Neurofilament light chain levels deviated from normative ranges decades before symptom onset, but plateaued thereafter and did not show sensitivity to intra-individual change. Across the full disease course, volumetric MRI—particularly pons volume—demonstrated the highest sensitivity to change, supporting the utility of infratentorial volumetric measures as progression as well as stratification biomarkers, particularly for early-phase trials.

4.5 Pipeline Development

A key contribution of this work is the development of an automated multimodal imaging pipeline designed for longitudinal and multisite applications. This included subsegmentation of infratentorial and spinal structures (De Leener et al., 2017; Faber et al., n.d.; Henschel et al., 2020; Iglesias et al., 2015), harmonization of diffusion metrics across scanners using ComBat (Fortin et al., 2017), and integration of tractography using multi-shell multi-tissue spherical deconvolution (Jeurissen et al., 2014). For quantitative susceptibility mapping (QSM), a two-pass reconstruction approach, as proposed in QSMxT (Stewart et al., 2021), was implemented to enhance anatomical specificity and mitigate artefacts. Additionally, to enable large-scale analysis of subcortical nuclei, a deep learning model was trained on manually segmented data which will be used for future studies with higher cohort sizes.

4.6 Limitations and Future Directions

Despite the use of advanced tractography methods, diffusion quantification relied on tensor-based scalar metrics, which remain limited in regions with crossing or bending fibres. The low sensitivity of FA and radial diffusivity to longitudinal change in the cerebellar peduncles and brainstem was consistent across studies and reinforces the need for alternative models such as neurite orientation dispersion and density imaging or diffusion kurtosis imaging (Jensen et al., 2005; Zhang et al., 2012). While pons volume showed strong performance, it is unlikely that a single measure will capture the full spectrum of disease progression. Integration of structural, microstructural, and biochemical markers into composite indices may improve staging and stratification. Most data in this thesis were derived from European participants. Broader inclusion of diverse populations will be necessary to ensure generalizability. As antisense oligonucleotide therapies move toward clinical application, identifying sensitive and reliable imaging biomarkers becomes increasingly urgent.

The findings presented here suggest that volumetric imaging of the pons and upper spinal cord may serve as useful candidates for monitoring early neurodegenerative change.

4.7 References

De Leener, B., Lévy, S., Dupont, S.M., Fonov, V.S., Stikov, N., Louis Collins, D., Callot, V., Cohen-Adad, J., 2017. SCT: Spinal Cord Toolbox, an open-source software for processing spinal cord MRI data. NeuroImage 145, 24–43. https://doi.org/10.1016/j.neuroimage.2016.10.009

Faber, J., Kügler, D., Bahrami, E., Heinz, L.-S., Timmann, D., Ernst, T.M., Deike-Hofmann, K., Klockgether, T., n.d. CerebNet: A fast and reliable deep-learning pipeline for detailed cerebellum sub-segmentation 16.

Fortin, J.-P., Parker, D., Tunç, B., Watanabe, T., Elliott, M.A., Ruparel, K., Roalf, D.R., Satterthwaite, T.D., Gur, R.C., Gur, R.E., Schultz, R.T., Verma, R., Shinohara, R.T., 2017. Harmonization of multi-site diffusion tensor imaging data. NeuroImage 161, 149–170. https://doi.org/10.1016/j.neuroimage.2017.08.047

Haas, E., Incebacak, R.D., Hentrich, T., Huridou, C., Schmidt, T., Casadei, N., Maringer, Y., Bahl, C., Zimmermann, F., Mills, J.D., Aronica, E., Riess, O., Schulze-Hentrich, J.M., Hübener-Schmid, J., 2022. A Novel SCA3 Knock-in Mouse Model Mimics the Human SCA3 Disease Phenotype Including Neuropathological, Behavioral, and Transcriptional Abnormalities Especially in Oligodendrocytes. Mol. Neurobiol. 59, 495–522. https://doi.org/10.1007/s12035-021-02610-8

Henschel, L., Conjeti, S., Estrada, S., Diers, K., Fischl, B., Reuter, M., 2020. FastSurfer - A fast and accurate deep learning based neuroimaging pipeline. NeuroImage 219, 117012. https://doi.org/10.1016/j.neuroimage.2020.117012

Iglesias, J.E., Van Leemput, K., Bhatt, P., Casillas, C., Dutt, S., Schuff, N., Truran-Sacrey, D., Boxer, A., Fischl, B., Alzheimer's Disease Neuroimaging Initiative, 2015. Bayesian segmentation of brainstem structures in MRI. NeuroImage 113, 184–195. https://doi.org/10.1016/j.neuroimage.2015.02.065

Jensen, J.H., Helpern, J.A., Ramani, A., Lu, H., Kaczynski, K., 2005. Diffusional kurtosis imaging: the quantification of non-gaussian water diffusion by means of magnetic resonance imaging. Magn. Reson. Med. 53, 1432–1440. https://doi.org/10.1002/mrm.20508

Jeurissen, B., Tournier, J.-D., Dhollander, T., Connelly, A., Sijbers, J., 2014. Multi-tissue constrained spherical deconvolution for improved analysis of multi-shell diffusion MRI data. NeuroImage 103, 411–426. https://doi.org/10.1016/j.neuroimage.2014.07.061

Schuster, K.H., Zalon, A.J., Zhang, H., DiFranco, D.M., Stec, N.R., Haque, Z., Blumenstein, K.G., Pierce, A.M., Guan, Y., Paulson, H.L., McLoughlin, H.S., 2022. Impaired Oligodendrocyte Maturation Is an Early Feature in SCA3 Disease Pathogenesis. J. Neurosci. Off. J. Soc. Neurosci. 42, 1604–1617. https://doi.org/10.1523/JNEUROSCI.1954-20.2021

Stewart, A.W., Robinson, S.D., O'Brien, K., Jin, J., Widhalm, G., Hangel, G., Walls, A., Goodwin, J., Eckstein, K., Tourell, M., Morgan, C., Narayanan, A., Barth, M., Bollmann, S., 2021. QSMxT: Robust Masking and Artefact Reduction for Quantitative Susceptibility Mapping (preprint). Neuroscience. https://doi.org/10.1101/2021.05.05.442850

Zhang, H., Schneider, T., Wheeler-Kingshott, C.A., Alexander, D.C., 2012. NODDI: practical in vivo neurite orientation dispersion and density imaging of the human brain. NeuroImage 61, 1000–1016. https://doi.org/10.1016/j.neuroimage.2012.03.072

5. Statement on own contribution

The work was carried out at the German Center for Neurodegenerative Disease (DZNE) under the supervision of PD Dr. Jennifer Faber.

For the publication Cerebellar Volumetry in Ataxias: Relation to Ataxia Severity and Duration, the work was designed by me, PD Dr. Jennifer Faber and Prof. Dr. Thomas Klockgether. All analyses were carried out by me, after training and with the support of PD Dr. Jennifer Faber and Dr. Tamara Schaprian. The data were acquired by the multicenter collaborators listed in the publication. The statistical evaluation was carried out by me.

For the publication Progression of biological markers in spinocerebellar ataxia type 3: longitudinal analysis of prospective data from the ESMI cohort, the work was designed by me, PD Dr. Jennifer Faber, Prof. Thomas Klockgether (clinical neurology) and Dr. Moritz Berger (biostatistics), and Dr. Hector Garcia-moreno and Dr. Jeannette Hübener-Schmid. The magnetic resonance and demoghraphic data used for the anaylsis was compiled by me. The pre and post processing of the magnetic resonance data was carried out by me. The data were collected within the ESMI cohort by the multicenter collaborators listed in the publication.

For the publication Myelin water fraction mapping with joint inversion of gradient-echo and spin-echo data, the work was designed by me, Ségolène Dega, Prof. Dr. Hendrik Paasche, and Prof. Dr. Tony Stöcker. The analyses were carried out by me in collaboration with Ségolène Dega, Marten Veldmann, and Ruediger Stirnberg. The data were collected by the Bonn MRI core facility. The statistical evaluation was carried out by me, after consultation with Prof. Dr. Tony Stöcker.

I hereby confirm that my thesis complies with the Statement by the Executive Committee of the Deutsche Forschungsgemeinschaft (DFG, German Research Foundation) on the Influence of Generative Models of Text and Image Creation on Science and the Humanities and on the DFG’s Funding Activities.